PHOTOCHEMICAL METAL ORGANIC DEPOSITION OF METAL OXIDES

by

Wai Lung (Simon) Law

B. Sc. Simon Fraser University, 1995

THESIS SUBMITTED IN PARTIAL FULFILLMENT OF THE
REQUIREMENTS FOR THE DEGREE OF

DOCTOR OF PHILOSOPHY

in the Department
of
CHEMISTRY

SIMON FRASER UNIVERSITY

April, 2004

APPROVAL

Name: Wai Lung (Simon) Law

Degree: Doctor of Philosophy

Title of Thesis: Photochemical Metal Organic Deposition of Metal Oxides

Examining Committee:

Chair: Dr. V. Williams (Assistant Professor)

Dr. R.H.Hill (Professor) Senior Supervisor

Dr. G.W. Leach (Associate Professor) Committee Member

Dr. Z-G. Ye (Professor) Committee Member

Dr. D.B. Leznoff (Assistant Professor) Internal Examiner

Dr. F.C.J.M. van Veggel (Professor) External Examiner
Department of Chemistry, University of Victoria

Date Approved: april 2, 2004

SIMON FRASER UNIVERSITY

Partial Copyright Licence

Abstract

This thesis pertains to the study of the deposition of metal oxide thin films via the process of Photochemical Metal Organic Deposition (PMOD). In this process, an amorphous metal organic precursor thin film is subjected to irradiation under ambient conditions. Fragmentation of the metal precursor results from the photoreaction, leading to the formation of metal oxide thin films in the presence of oxygen. The advantage of PMOD lies in its ability to perform lithography of metal oxide thin film without the application of photoresist. The metal organic precursor can be imaged directly by photolysis through a lithography mask under ambient conditions. Thus the PMOD process provides an attractive alternative to the conventional VLSI fabrication process.

Metal carboxylates and metal acetylacetonates complexes were used as the precursors for PMOD process in this thesis. Transition metal carboxylate and metal acetylacetonate complexes have shown previously that when deposited as amorphous thin films, they will undergo fragmentation upon photolysis, leading to the formation of metal oxide thin films under ambient conditions. In this thesis, the formation of main group metal oxides of aluminum, indium and tin, as well as the formation of rare-earth metal oxides of cerium and europium by PMOD from its corresponding metal organic precursor will be presented. The nature of the photoreactions as well as the properties of the thin films deposited by PMOD will be investigated.

Doped metal oxide thin films can also be prepared using the PMOD process. By mixing the metal precursors prior to deposition in the desired ratio, precursor films containing more than one metal precursor can be obtained. Mixed metal oxide thin films corresponding to the original metal ratio, in the precursor mixture, can be obtained upon photolysis under ambient conditions. In this thesis, the properties of doped metal oxide thin films of europium doped aluminum oxide as well as tin doped indium oxide thin films will also be presented.

Dedication

To my family that makes my dreams possible

Acknowledgements

I would like to express my sincere appreciation for the support and guidance of my senior supervisor, Professor Ross H. Hill. I will always remember the help and advices from Professor Hill throughout my graduate school career.

I would also like to thank my examining committee, Professor Frank van Veggel, Professor Gary Leach, Professor Zuo-Guang Ye, Professor Daniel Leznoff for their time and input to my thesis.

My special thanks go to Dr. Sharon Blair of Tekion Solutions Inc. for her understanding and tremendous support.

Also I would like to thank all the past and present members of Professor Ross H. Hill's research group for their help and friendship. Special thanks are given to Dr. Juan Pablo Bravo Vasquez and Mr. Xin Zhang for their help with the Auger Analysis, Mr. Simon Trudel for his help with numerical analysis for experimental data.

I would also like to thank Mr. Greg Owen for performing mass spectrometry, Professor Brent Heinrich from Department of Physics at SFU for permission to perform Auger Electron Spectroscopy. Also a thank you to Mr. Bill Wood from the School of Engineering Science at SFU for access of clean room facilities, Dr. Ming Dong for performing dielectric constant measurement and Dr. Sean Barstow from School of Chemical Engineering at GIT for performing refractive index measurements.

Last but certainly not least, I sincerely thank Miss Helen Yeung for her encouragement and being my best companion.

Table of Contents

List of Figures

List of Tables

List of Abbreviations and Symbols

A	absorbance
AES	Auger electron spectroscopy
AFM	atomic force microscopy
AIBN	2, 2'-Azobisisobutyronitrile
ALE	atomic layer epitaxy
C	capacitance
CF	correction factor
CVD	chemical vapor deposition
d	distance
E	Einstein
F	faraday
FTIR	Fourier transformed infrared
hν	energy of a photon
I	current
I_o	light intensity
IC	integrated circuit
J	joule
L	ligand
LMCT	ligand-to-metal charge transfer
M	metal
MBE	molecular beam epitaxy

MIM	metal-insulator-metal
MS	mass spectroscopy
n	integer or refractive index
PMOD	Photochemical Metal Organic Deposition
R	resistance
R_s	sheet resistance
RF	radio frequency
s	second
t	time
UV	ultraviolet
V	voltage
vis	visible
VLSI	very large scale integrated
X	mole fraction
XRD	X-ray diffraction
YBCO	Yttrium barium copper oxide
ε	extinction coefficient
ε_o	permittivity of free space
θ	angle
λ	wavelength
ν	frequency
Φ	quantum yield of the photoreaction
Ω	ohm

Chapter 1

Introduction

1.1. Introduction

This chapter begins with an introduction to Photochemical Metal Organic Deposition (PMOD), a novel deposition technique for metal or metal oxide thin films using amorphous metal-organic precursor films under ambient conditions. The characteristics of the PMOD process, including its advantage over current deposition techniques in depositing patterned metal oxide thin films will be discussed. This is followed by an explanation of the various analytical tools that are used to characterize the thin films throughout the thesis. Then a discussion of the physical properties of the thin films of interest to this thesis will be presented. Finally, an overview of the organization of the thesis will be provided.

1.2. Photochemical Metal Organic Deposition (PMOD)

Metal oxide thin films have a wide range of applications in the electronics industry and a variety of methods have been developed to deposit thin films of metal oxides.[1-6] In this thesis, Photochemical Metal Organic Deposition (PMOD), a photochemical process to deposit metal oxide and mixed metal oxide films under ambient conditions will be introduced. A variety of transparent metal oxides films ranging from aluminum oxide, an insulator, to tin-doped indium oxide, a semiconductor, will be deposited using this photochemical process.

1.2.1 The PMOD process

The PMOD process is outlined in Figure 1.1. It begins by the preparation of metal organic precursor (ML_n in which M stands for the metal center while L represents the coordinated ligands) solution in a volatile solvent. By spin casting the solution onto a desired substrate, a thin amorphous precursor film is formed. The film is then subjected to irradiation in which photolysis of the precursor results in the fragmentation of the precursor as illustrated in equation (1.1), and in Figure 1.1a).

$$ML_n \xrightarrow{h\nu} M + n\,L \qquad 1.1$$

During this process, the ligands escape from the film, leaving the metal on the substrate as shown in Figure 1.1b). When the photoreaction is carried out in vacuum or in a reducing environment, a metal film can be produced.[7] When the photoreaction is carried out under ambient conditions, the metal formed during the fragmentation is oxidized by oxygen, forming a metal oxide as illustrated in Figure 1.1c).[8]

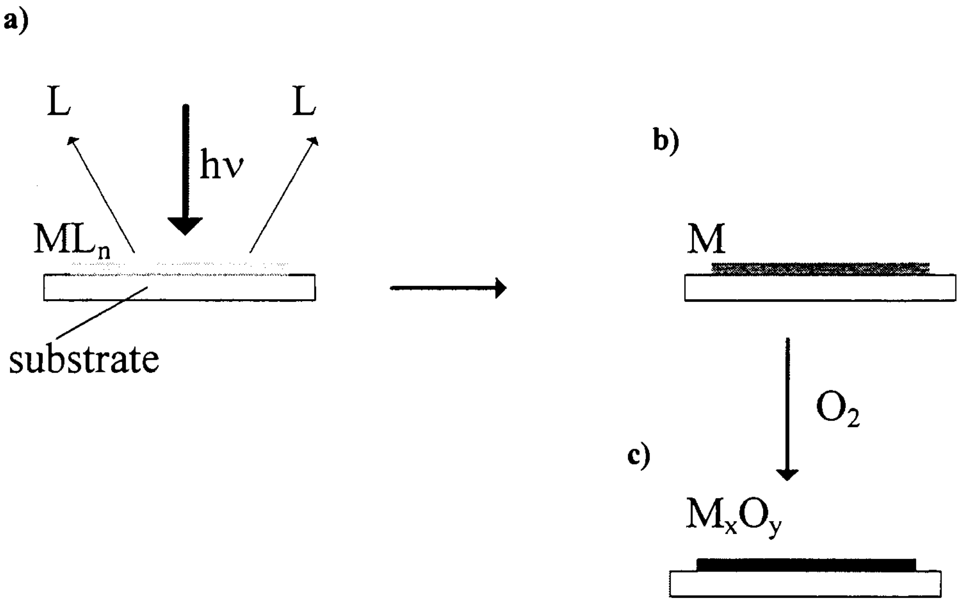

Figure 1.1 Schematic representation of PMOD. a) Irradiation to the precursor film results in the decomposition of the precursor, with ligand fragments leaving the film surface. b) The decomposition leads to the formation of metal film. c) Metal oxide forms upon reaction with oxygen when reaction is carried out under ambient conditions.

The advantages of PMOD over common thin film deposition techniques such as chemical vapor deposition (CVD), sputtering, sol-gel and molecular beam epitaxy (MBE) are that the PMOD process is a low energy process which can be conducted under ambient conditions. Equipment requirements for PMOD are low because the metal oxide films can be prepared without the use of expensive vacuum chambers and/or high-energy ion beam. The PMOD process also enables photoresist-free lithographic processing, and the existing photolithography equipment in the electronic industry can be used in the PMOD process.

The PMOD process is also a lot simpler to most other thin film deposition processes in preparing mixed metal oxide thin films. In order to prepare a mixed metal oxide thin film by PMOD, the two metal precursors are dissolved in a solvent in a stoichiometric ratio. A precursor film of the mixed metal precursors is obtained by spin coating and upon photolysis, a mixed metal oxide thin film with a ratio between the two metals corresponding to the original precursor ratio can be obtained.

This process is summarized in Figure 1.2 in which M^1 and M^2 denote the two different metals. Upon photolysis, the precursor film of the mixed metal precursor decomposes and ligand fragments escape from the precursor film as in Figure 1.2a). This results in the formation of a mixed metal film as in Figure 1.2b). When the reaction is carried out under ambient conditions, the mixed metals will be oxidized, resulting in the formation of the mixed metal oxide thin film as in Figure 1.2c). The metal ratio M^1:M^2 in the photolyzed film remains the same as in the original precursor mixture.

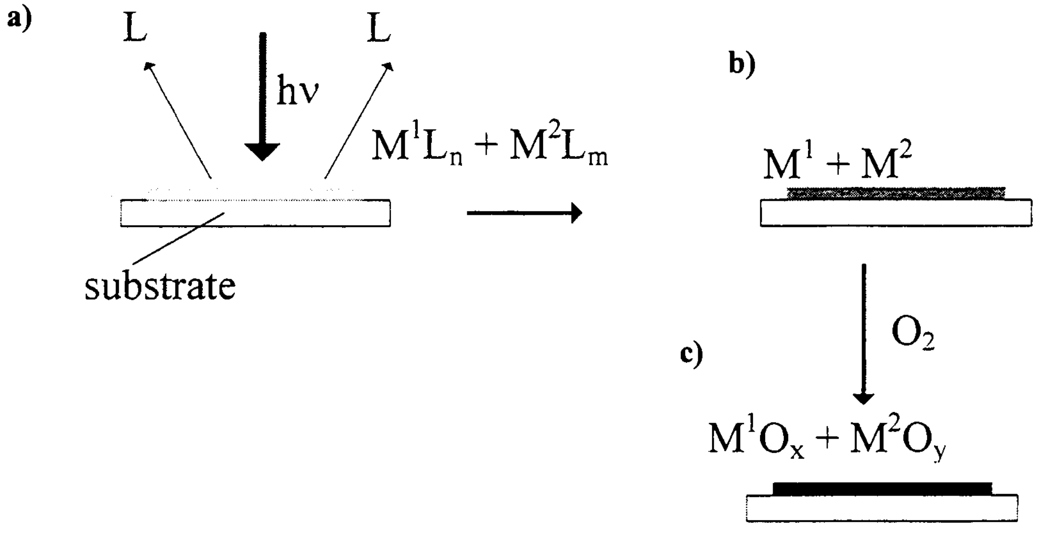

Figure 1.2 Schematic representation of PMOD to prepare mixed metal oxides thin film. a) Irradiation of the precursor film of mixed metal precursors results in the decomposition of the precursors, with ligand fragments leaving the film surface. b) The decomposition leads to the formation of a mixed metal film. c) Mixed metal oxide, with a ratio between the two metals equal to that of the original mixture, forms upon reaction with oxygen when reaction is carried out under ambient conditions.

The PMOD process requires precursors with specific qualities. The first requirement for a successful precursor for the PMOD process is that it be photosensitive since the driving force of the process is via irradiation. The precursor also has to be able to form amorphous films on the substrate. This is because during the photolysis, the precursor decomposes and the ligand or its fragments diffuse out of the film. However, diffusion is restricted in a crystal. This in turn will make recombination more probable, leading to a lower quantum efficiency. The precursor also has to be thermally stable in order to be able to perform photolithography with the PMOD process.

A wide range of metal organic complexes have been studied, including metal carboxylates, metal acetylacetonates, metal carbonyls as well as metal complexes with amines and phosphines.[7-11] Among the classes of complexes being studied, metal carboxylates and metal acetylacetonates have provided useful precursors.

Metal carboxylates are able to undergo charge transfer in the UV-vis region upon irradiation.[12] Transitions such as ligand-to-metal charge transfer (LMCT) upon irradiation are able to trigger the photolysis of metal carboxylates, leading to the fragmentation of the precursor molecule. The general structure of a metal carboxylate is illustrated in Figure 1.3. It shows a bidentate coordination with the metal center. However, other modes of coordination such as monodentate as well as bridging are also common in metal carboxylates.

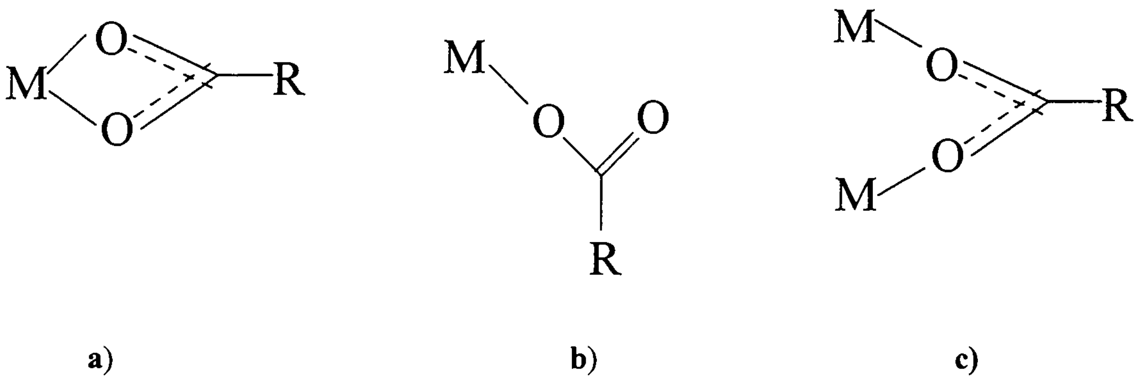

Figure 1.3 Structures of metal carboxylate illustrating a) bidentate b) monodentate and c) bridging coordinations (M denotes the metal centre while R represents an organic group.)

Metal acetylacetonates have intense charge transfer bands in the UV-vis region.[13] These bands make this type of precursor capable to undergo photolysis upon irradiation in the UV-vis region. These absorptions generally have higher extinction coefficients when compared to metal carboxylate complexes, thus leading to a more efficient photoreaction. The general structure of a metal acetylacetonate is illustrated in Figure 1.4.

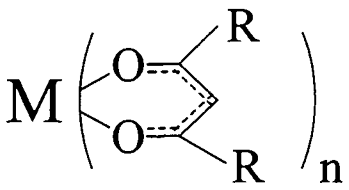

Figure 1.4 General structure of a metal acetylacetonate where M denotes the metal center and R represents an organic group.

1.2.2 Photoresist-free lithography by PMOD

The advantage of the PMOD process lies in its ability to deposit metal or metal oxide patterns onto the desired substrate in the absence of photoresist. In the electronic fabrication of very large scale integrated (VLSI) devices, integrated circuits (IC) are printed onto silicon substrate by photolithography through the use of photoresist. A comparison between a photoresist and a photoresist-free printing process is illustrated in Figure 1.5. In photolithography with photoresist, a layer of photoresist is first deposited on the surface of the substrate as in Figure 1.5 a) 1. In Figure 1.5 a) 2, the substrate is then irradiated through a mask with the desired pattern. Irradiation changes the solubility of the exposed photoresist. In the case shown in the diagram, irradiation renders the photoresist more soluble (negative resist). The pattern is revealed upon rinsing of the substrate, as in Figure 1.5 a) 3. Metal or metal oxide is deposited onto the substrate via one of a variety of thin film deposition methods such as chemical vapor deposition, sputtering and molecular beam epitaxy (MBE) and is shown in Figure 1.5 a) 4.[14-16] The surface of the coated substrate is then developed, either by wet etching in chemical solutions or by dry etching with plasma etching before the final pattern is revealed as in Figure 1.5 a) 5.

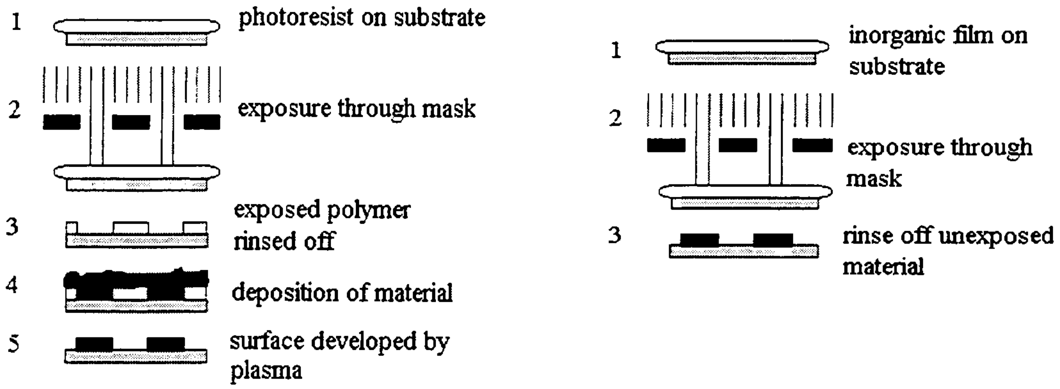

a) Lithography with photoresist **b) Phororesist-free lithography**

Figure 1.5 Comparison between lithography with a) a photoresist and b) a photoresist-free process.

In photoresist-free deposition techniques such as PMOD, a metal-organic film is deposited onto the substrate as in Figure 1.5 b) 1. The coated substrate is then irradiated through a mask with the desired pattern as shown in Figure 1.5 b) 2. The exposed material undergoes photolysis, forming metal or metal oxide depending on the reaction environment while the organic products outgas. The unexposed material is rinsed off with an appropriate solvent and the pattern is revealed as in Figure 1.5 b) 3. No etching step is required during the PMOD process. Fewer steps are required to deposit metal or metal oxide pattern with photoresist-free deposition, leading to a potential reduction of production cost. The PMOD process will also require one less image transfer step when compared to the conventional method. Thus a photoresist-free deposition technique such as PMOD is an attractive alternative to the conventional VLSI fabrication process.

1.3. Thin film characterization methods

Thin films used in this thesis are characterized with a variety of analytical tools and these methods will be highlighted in the following sections.

1.3.1 Powder x-ray diffraction (XRD)

The crystal structures of the films will be determined by the use of powder x-ray diffraction. X-ray diffraction is a non-destructive analytical technique that provides information on the periodicity of the atomic arrangement of the test sample. For a crystalline material, Bragg's equation can be used to describe the x-ray diffraction phenomenon and is represented in equation 1.2.

$$n\lambda = 2d\,sin\theta \qquad 1.2$$

In the equation n is an integer, λ refers to the wavelength of the x-ray, d is the perpendicular distance between adjacent crystalline planes and θ represents the angle between the incident x-ray beam and the crystalline plane. For a crystalline material, $2d\sin\theta$ represents the difference in the path length traveled by 2 paths of an x-ray beam. When it is equal to an integral number of the wavelength of the x-ray (in phase), the Bragg condition is satisfied. This results in a strong signal in the x-ray spectrum due to the constructive interference of the x-ray reflection. The position and intensity of reflections from a crystal are indicative of the underlying atomic structure. However in the thesis, the crystal structure of the analyzed materials will be determined by comparison with previously known structures. The x-ray spectrum will be compared to a database of standards to identify its crystal structure.

1.3.2 Auger Electron Spectroscopy (AES)

Auger electron spectroscopy will be used to determine the elemental composition of the thin films in this thesis. The basis of Auger electron spectroscopy can be best described by considering the following figures. When an atom is exposed to a beam of high energy electrons as in Figure 1.6 a), the atom is ionized by the loss of a core level electron as in Figure 1.6 b). At this point a transition in the atom can occur by an electron from a higher energy level filling the vacancy at the core level. The energy generated can in turn release a second electron, the Auger electron, as illustrated in Figure 1.7.[17] The energy of the Auger electron is specific to the atom from which it originated and proportional to the concentration of the atoms on the surface. Therefore, Auger electron spectroscopy will be able to determine the two-dimensional elemental composition of the surface of the sample.

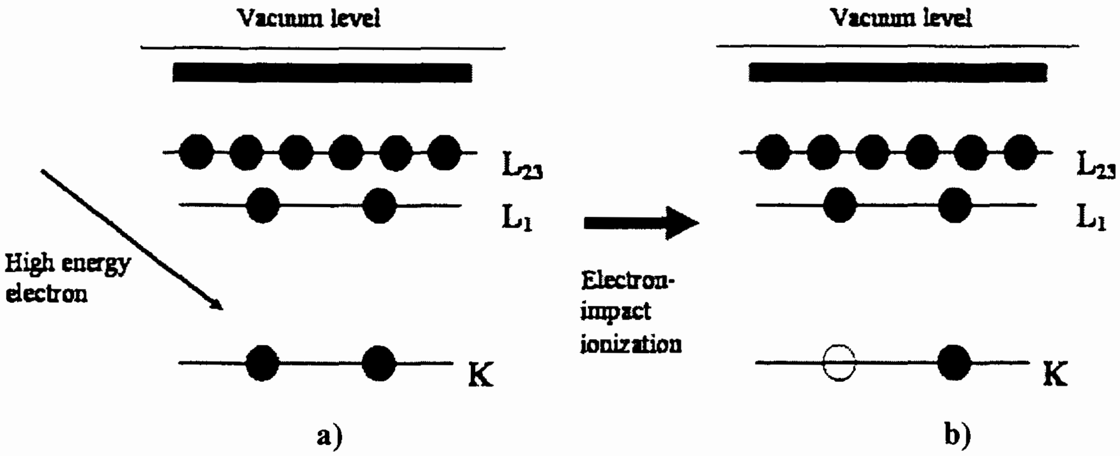

Figure 1.6 Ionization of an atom at core level. a) A high energy electron interacts with a ground state atom resulting in the loss of an electron from a core level (K) to yield, b) an excited ion.

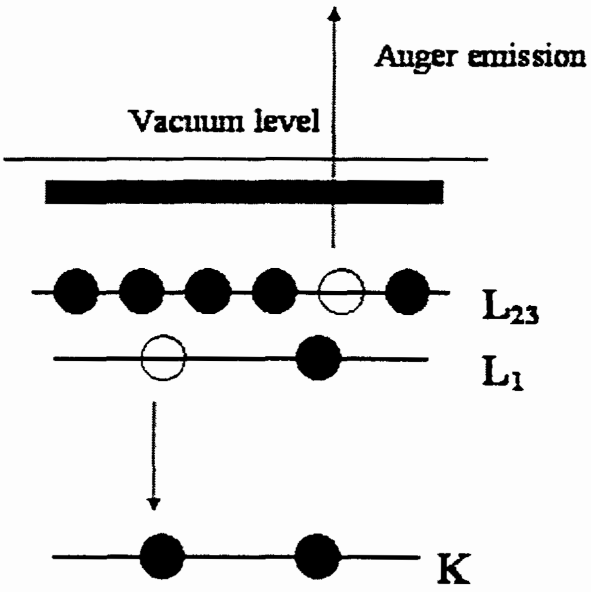

Figure 1.7 Emission of Auger electron. The relaxation of a electron from one level (L_1) to fill a core energy (K) produces sufficient energy to ionize an Auger electron (L_{23}).

In order to evaluate the composition of the material beneath the surface, material from the surface of the sample will have to be removed. This is achieved with the use of an argon ion sputtering gun. The ion beam etches the surface of the sample, revealing the material beneath the surface of the sample for analysis. Thus the depth profile of a particular sample can be obtained.

1.3.3 Profilometry

The thickness of samples can be measured by a profilometer. Surface profilometry requires the use of a submicron stylus. During measurement, the stylus is brought to contact to the surface of the sample. When the stage supporting the specimen moves in a horizontal direction, the vertical displacement from the stylus is recorded and the measurement of the movement of the stylus in relation to the horizontal displacement gives the measurement of the topography of the sample.

1.3.4 Atomic force microscopy (AFM)

The surface morphology of the samples can also be evaluated by atomic force microscopy. Atomic force microscopy operates on the same principle as profilometry. A sharp tip (apex radius ~20 nm) formed on a soft cantilever is used to probe the interaction (force) between the tip and sample surface. The interaction between the tip and sample surface is measured through the deflection of a cantilever using a laser beam and photodetector. The more common modes of AFM are the contact mode and the dynamic mode. In the contact mode AFM the tip is mechanically contacted with sample surface at an applied force. Dynamic force mode AFM was developed to measure soft surfaces where the contact mode AFM could result in a degradation on the surface due to a large applied force. This mode is operated with a stiff cantilever with a typical spring constant of ~ 40 N/m, which is oscillated at around its resonant frequency. The amplitude decreases when the tip "feels" attractive and/or repulsive forces as the tip is brought closer to the sample surface. The decrease of the oscillation frequency when the tip is close to the sample surface is used as the feedback parameter to obtain surface morphology.

1.4. Quantitative analysis for the photoreactions from PMOD

The efficiency of the photoreactions occurring during the PMOD deposition are evaluated through the study of the quantum yield of the photoreaction.[18] The quantum yield (Φ) for a photoreaction can be expressed as in equation 1.3.

$$\Phi = \frac{\text{Number of molecules undergoing a reaction}}{\text{Number of quanta of light absorbed by the molecules}} \qquad 1.3$$

The value obtained from the quantum yield calculation provides evidence about the nature of a photoreaction. In general the quantum yield of a photoreaction will be less than one since not every photon will result in a reaction in a molecule. A quantum yield of more than one is an indication of secondary reactions which take place as a result of the primary photoreaction. A quantum yield value higher than two is likely the result of a photoreaction which initiates a chain reaction. When the quantum yield is much less than one, it is likely that the energy of the photon is mostly being consumed in physical processes (i.e. non-radiative decay, emission etc).[19]

1.5. Properties of thin films

In this thesis, the physical properties of the thin films deposited by PMOD will be determined. This section provides an introduction to some of these physical properties and methods for determining these properties.

1.5.1 Dielectric constant

Dielectric constant is a measure of polarizability of the material in an electric field, which is a measure of response to an applied electric field. Dielectric constant is an important material property in many applications. To understand this important property, we will consider dielectric constant in terms of a capacitor. The dielectric constant of the material can be determined by measuring the capacitance of the material in a metal-insulator-metal (MIM) structure. A dielectric material between the plates of a parallel plate capacitor is illustrated in Figure 1.8.[20] The dielectric constant for a material in this structure is given by equation 1.4.

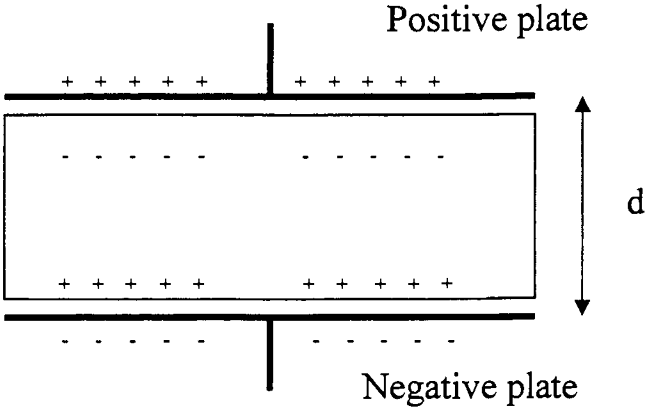

Figure 1.8 Dielectric material between the plates of a parallel plate capacitor.

$$\varepsilon_r = C\,d\,/\,A\,\varepsilon_0 \qquad 1.4$$

In equation 1.4, ε_r is the dielectric constant of a particular material. C is the capacitance of the device, A is the area of the parallel plates, d is the thickness of the material and ε_0 is the dielectric constant of free space (8.854×10^{-12} F/m).

1.5.2 Refractive index

The refractive index of a medium is the ratio of the velocity of propagation of an electromagnetic wave in vacuum to its velocity in the medium. The refractive index of a material can be measured using an ellipsometer. Ellipsometry evaluates both the refractive index and the thickness of a semi-transparent thin film. In this technique, plane polarized light (usually in the form of He-Ne laser) is incident onto the film surface. The reflected light will be elliptically polarized. The ellipsometric parameters Ψ (amplitude ratio) and Δ (phase change) are measured from the process, which are related to the polarization change of the light caused by its interaction with a sample. The refractive index and the thickness of the test sample can then be calculated from the measured Ψ and Δ value through a regression process. The regression compares the measured spectra with values calculated from initial estimates of the film parameters. The ellipsometry experiment for the refractive index of the aluminum oxide thin films reported in this thesis was performed at the laboratory of Professor Cliff Henderson at the School of Chemical Engineering, Georgia Institute of Technology by Dr. Sean Barstow.

1.5.3 Sheet resistance

The electrical conductivity of a thin film is often expressed in terms of sheet resistance. It has the units of Ω/square. Sheet resistance is measured with a 4-point probe as illustrated in Figure 1.9. The four point probe consists of four probes which are brought in contact with the sample. Current (I) is made to flow between the outer probes while the voltage (V) is measured between the two inner probes. For a material in the form of an infinitely thin film resting on an insulating support, the sheet resistance R_s is given by equation 1.5.

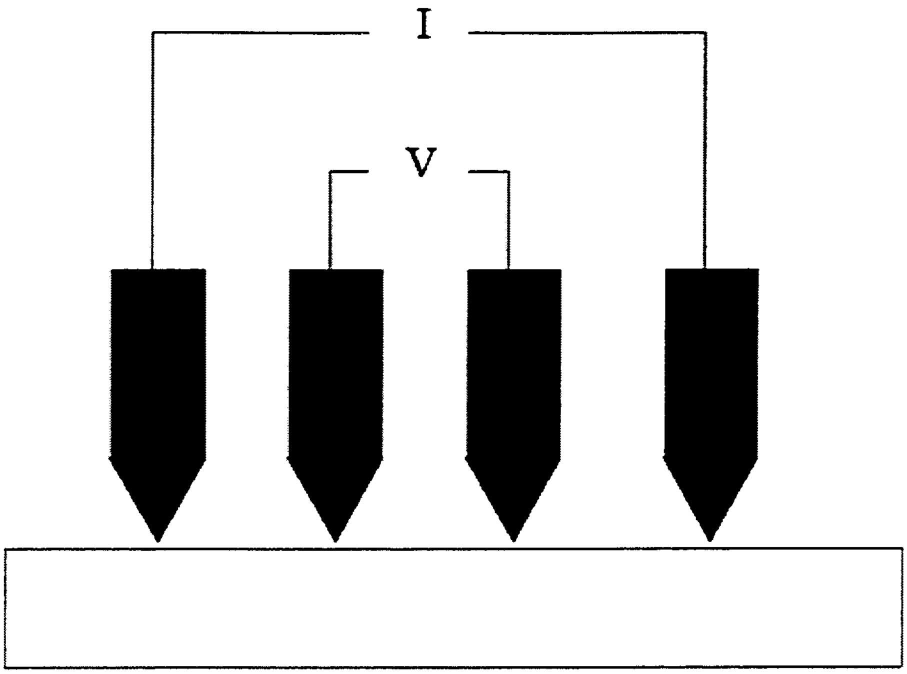

Figure 1.9 Four point probe measurement.

$$\mathbf{Rs = (V / I) \times 4.53} \qquad 1.5$$

In the equation, V is the measured DC voltage across the two voltage probes and I is the DC current passing through the two current probes and 4.53 is the correction factor (CF) for the equation.[21]

1.6. Organization of the thesis

The goal of this research is to demonstrate the versatility of the PMOD. In this thesis we show that a wide range of metal oxides can be deposited using the PMOD method. The range is shown to be broad by including main group, transition metal and rare earth oxides. Unlike some other thin film deposition techniques, mixed oxide systems can be produced easily by using a stoichiometric mixture of the desired ratio of the precursors. Furthermore the photoluminescence and electrical conductivity of two doped-metal oxides deposited by PMOD will be presented.

Chapter 2 describes the photochemistry of the 2-ethylhexanoate complexes of cerium and europium. These are the first example of the PMOD process applied to rare-earth metal organic complexes. When these compounds are irradiated, photolysis will occur, leading to the formation of their respective oxides. The photolithography experiments demonstrated the deposition of micron size structures onto silicon substrates.

Chapter 3 describes the deposition of aluminum oxide, the first example of the PMOD process applied to a main group metal oxide. A series of aluminum β-diketonate and mixed β-diketonate alkoxide compounds were used in this study. Carbon free amorphous aluminum oxide was formed by PMOD from these complexes. The introduction of alkoxide ligands to the metal complexes was found to increase the purity of the final product.

Chapter 4 presents the physical properties of the deposited aluminum oxide thin films. The dielectric constant and the refractive index measurement of the as-deposited aluminum oxide films suggested the aluminum oxide deposited by PMOD is of a porous nature. A mixed metal oxide system of europium-doped aluminum oxide was also demonstrated and its photoluminescence presented. This demonstrates the versatility of the PMOD process in the preparation of mixed metal oxides thin films.

Chapter 5 describes the PMOD process for tin (II) oxide, another main group metal oxide. Carbon free amorphous tin (II) oxide thin film is produced by the PMOD from tin (II) 2-ethylhexanoate carboxylate. The proposed mechanism of the photoreaction is also presented.

In chapter 6, the deposition of indium oxide, a transparent oxide, is presented using an indium (III) methyl(trimethyl)acetylacetate precursor. Tin-doped indium oxide thin films were also produced using the PMOD process by starting with mixture of tin and indium metal organic precursors. The conductivity characteristics of the amorphous indium oxide and tin-doped indium oxide as well as their crystalline counterparts are presented in terms of their sheet resistance. It was shown that electrical conductivity in this type of material is closely related to its crystalline structure.

Chapter 2

Photochemical Metal Organic Deposition (PMOD) of Cerium Oxide and Europium Oxide Thin Films

2.1. Introduction

This chapter outlines a method for the deposition of patterned cerium and europium oxide films from the corresponding 2-ethylhexanoate complexes by photochemical metal organic deposition (PMOD). Thin films of rare earth metal oxides are considered as promising coating materials due to their mechanical and chemical stability.[22] Thin films of cerium oxide (CeO_2) have a range of technical applications. Its dielectric constant, 26, makes it useful as a substrate for silicon on insulator structures and also for dielectric spacers in capacitors.[23, 24] Crystalline CeO_2 is of the fluorite structure, and its lattice constant is well matched with silicon.[25] The CeO_2 structure has a good lattice match with YBCO, a superconducting material. This fact and the insulating properties have been used in the construction of some structures with YBCO superconductors.[26-28] The high refractive index of CeO_2 also makes it a useful material for optical coatings.[29, 30] Europium (III) oxide (Eu_2O_3) is widely used as a phosphor activator and in laser technology.[31] Europium (II) oxide (EuO) has a simple NaCl crystal structure and is ferromagnetic below the temperature of 69K.[32]

CeO_2 thin film deposition has been accomplished by E-beam evaporation,[23, 29] laser ablation,[24, 26, 33-35] ion beam deposition,[25, 35] and RF magnetron sputtering.[27,28, 30] Thin films of europium oxide are prepared by vacuum evaporation,[31] pulsed laser deposition,[32] and electrodeposition.[36] With the exception of the electrodeposition technique, these methods are all high-capital, high-energy processes. The other drawback with all these methods is that they do not easily result in patterned surfaces and, therefore require additional lithographic procedures. In this chapter, photochemical metal organic deposition (PMOD) of the rare earth metal oxides of cerium oxide and europium oxide thin films will be introduced.

2.2. Results

2.2.1 Characterization of Cerium (III) and Europium (III) 2-ethylhexanoates

An amorphous film of $Ce(O_2CCH(C_2H_5)C_4H_9)_3$ was cast by spin coating from dichloromethane solution onto a silicon substrate (1 x 1.5 cm^2). The FTIR spectrum of a film of $Ce(O_2CCH(C_2H_5)C_4H_9)_3$ is presented in Figure 2.1 and the assignments of the IR absorptions of the carboxylic region are summarized in Table 2.1.

The FTIR spectrum of $Ce(O_2CCH(C_2H_5)C_4H_9)_3$ is remarkably similar to that of $Ce(O_2CCH_3)_3$ when compared to the literature data for solid $Ce(O_2CCH_3)_3$.[37-38] The absorptions near 3000 cm^{-1} were found to be consistent with C-H vibrations. The feature around 2300 cm^{-1} was attributed to the CO_2 in air during spectrum subtraction. There were also bands corresponding to C-C stretching modes at about 900 cm^{-1}. The series of intense absorptions in the region of 1000 – 2000 cm^{-1} corresponds to the coordinated carboxylate ligands. The intense absorptions in this region are associated with the symmetric and antisymmetric stretching modes of the CO_2 unit of the ligand. By comparing the FTIR spectra of $Ce(O_2CCH(C_2H_5)C_4H_9)_3$ and $Ce(O_2CCH_3)_3$, it was shown that the carboxylate absorbances are relatively insensitive to the nature of the alkyl group on the ligand. The FTIR bands corresponding to the coordinated carboxylate ligands of cerium (III) 2-ethylhexanoate were assigned using the assignment of $Ce(O_2CCH_3)_3$ as reference.

The carboxylate spectrum includes antisymmetric carboxylate stretches at 1588 and 1541 cm^{-1} for cerium (III) 2-ethylhexanoates. The spectrum also exhibits symmetric carboxylate stretches at 1460 and 1423 cm^{-1}. $Ce(O_2CCH_3)_3$ was know to have a polymeric structure in the solid state.[37, 38] With this information we propose that the precursor film consists of chelating carboxylate ligands with some bridging interactions in the films. The structure of the precursors in the films is best thought of as an idealized polymeric structure as illustrated in Figure 2.2.

The FTIR spectrum of $Eu(O_2CCH(C_2H_5)C_4H_9)_3$ has C-H vibration bands near 3000 cm^{-1} as well as a series of absorptions in the region of 1000 – 2000 cm^{-1} corresponding to the coordinated carboxylate ligands. The FTIR spectrum illustrating the carboxyl region for $Eu(O_2CCH(C_2H_5)C_4H_9)_3$ is shown in Figure 2.3. The IR absorptions at 1462 and 1427 cm^{-1} correspond to the symmetric carboxylate stretches. The band at 1531 cm^{-1} corresponds to the antisymmetric carboxylate stretch. The second antisymmetric carboxylate stretch is located at 1550 cm^{-1} as a shoulder of the intense absorption bands at 1531 cm^{-1}. The energy difference between pairs of symmetric and antisymmetric carboxylate stretches yielded values of 123 and 69 cm^{-1} (from the first pair of antisymmetric-symmetric peaks at 1550 and 1427 cm^{-1}, and the second peaks at 1531 and 1462 cm^{-1} respectively). These are the energy differences normally found in species with bridging and chelating carboxylate groups respectively.[39] No IR absorption related to free carboxylic acid was observed from the spectrum. The structure of the precursor film for $Eu(O_2CCH(C_2H_5)C_4H_9)_3$ can also be thought of as the idealized structure shown in Figure 2.2.

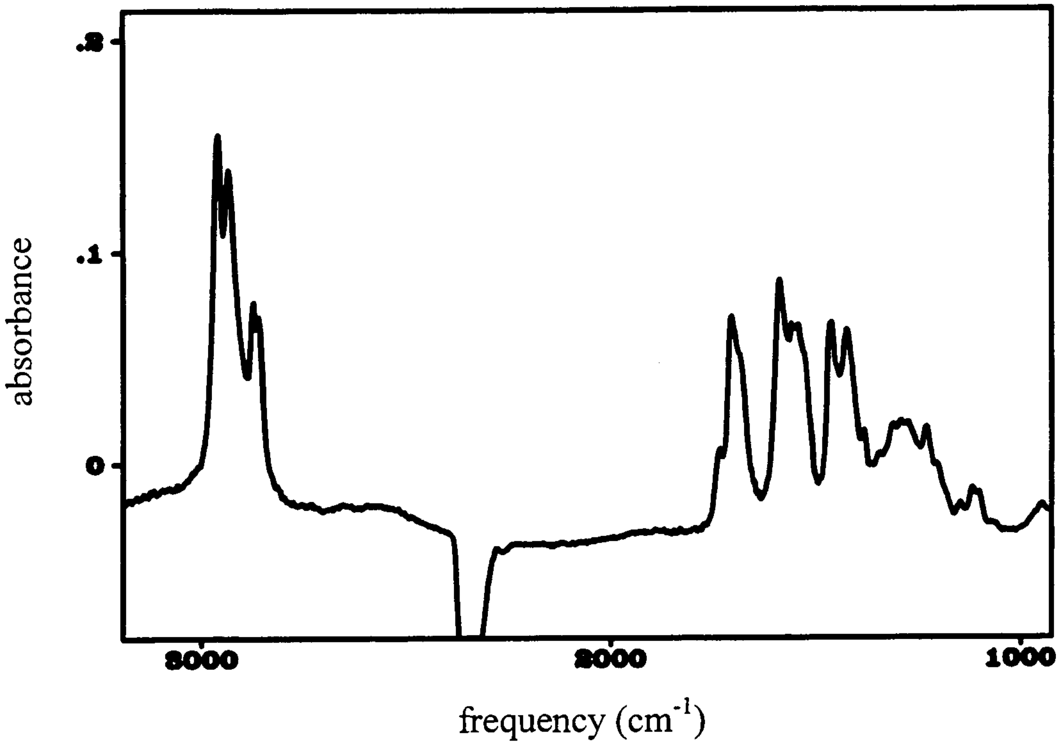

Figure 2.1 FTIR spectrum of $Ce(O_2CCH(C_2H_5)C_4H_9)_3$.

Table 2.1 Table of the Spectroscopic Data for Films of $Ce(O_2CCH(C_2H_5)C_4H_9)_3$, $Eu(O_2CCH(C_2H_5)C_4H_9)_3$ and $Ce(O_2CCH_3)_3$.

Assignment	$Ce(O_2CCH(C_2H_5)C_4H_9)_3$	$Eu(O_2CCH(C_2H_5)C_4H_9)_3$	$Ce(O_2CCH_3)_3$
ν(CO)antisym/ cm^{-1}(lnε)[a]	1588 (13.6)	1550 sh (14.0)	1605
ν(CO)antisym/ cm^{-1}(lnε)[a]	1541 (13.4)	1531 (14.6)	1523
ν(CO)sym/ cm^{-1}(lnε)[a]	1460 (13.4)	1462 (14.0)	1466
ν(CO)sym/ cm^{-1}(lnε)[a]	1423 (13.3)	1427 (14.2)	1449, 1433
LMCT[b]/ nm (lnε)[a]	287 (14.0)	252 sh (13.0)	
	254 (12.3)[c]	254 (12.9)[c]	

[a] Units of ε are cm^2/mol.

[b] The lowest energy absorbance in the electronic spectra of the films.

[c] lnε at irradiation wavelength (254 nm)

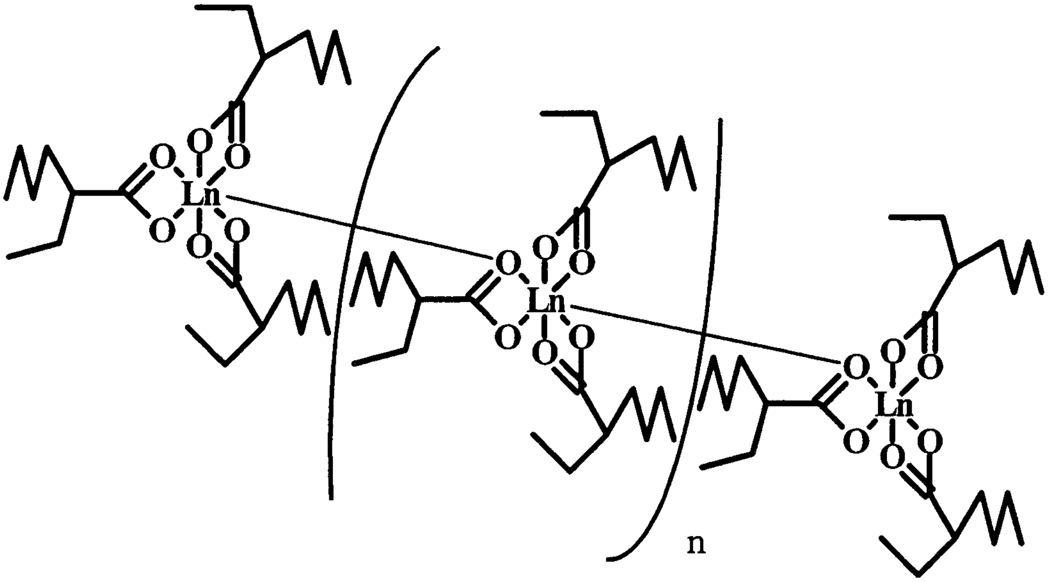

Figure 2.2 Illustration of the association between the complexes in amorphous thin films of cerium (III) and europium (III) 2-ethylhexanoates. (Ln = Ce and Eu).

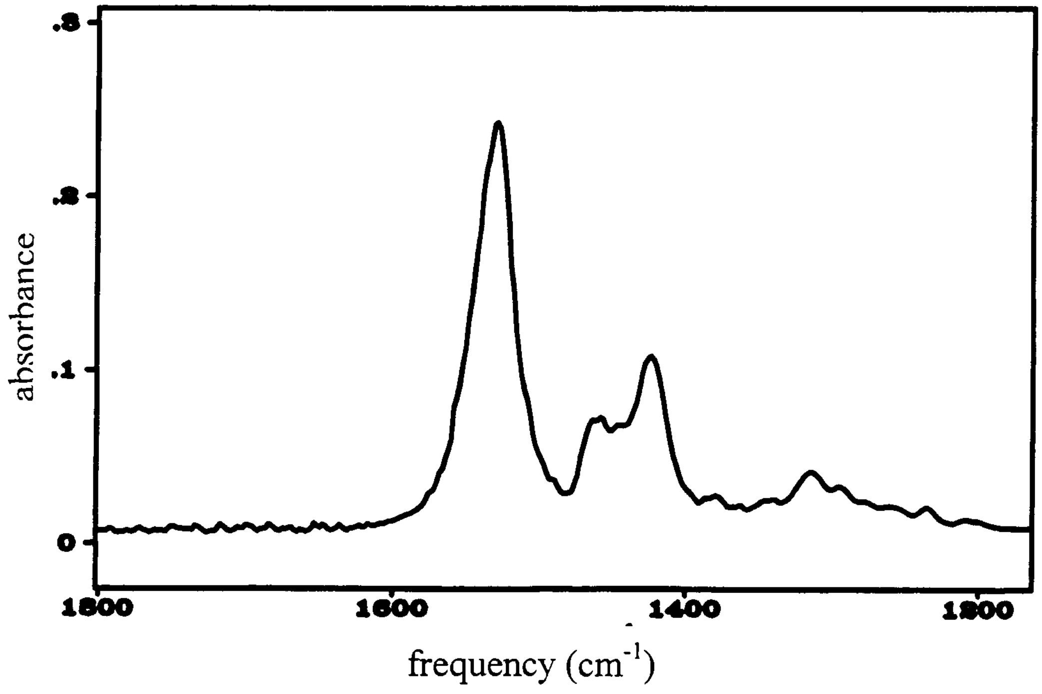

Figure 2.3 FTIR spectrum of $Eu(O_2CCH(C_2H_5)C_4H_9)_3$.

The electronic absorption spectra were also obtained on the thin films and are summarized in Table 2.1. In each case a band is resolved near 300 nm and higher energy bands are also indicated although these appear as shoulders to higher energy absorbances. The lowest energy transition is presumably associated with the charge transfer transition from the carboxylate ligand to the metal (LMCT) which affects the photochemistry corresponding to the PMOD. The extinction coefficients of these transitions are also included in Table 2.1.

2.2.2 Photochemistry of films of cerium (III) 2-ethylhexanoate and europium (III) 2-ethylhexanoate

A thin film of $Ce(O_2CCH(C_2H_5)C_4H_9)_3$ was irradiated at 254 nm. The photolysis of thin films of $Ce(O_2CCH(C_2H_5)C_4H_9)_3$ was monitored by FTIR spectroscopy. In Figure 2.4, the spectral changes associated with the photolysis of a thin film of $Ce(O_2CCH(C_2H_5)C_4H_9)_3$ are shown. The initial stages of the photoreaction are characterized by the loss of intensity of bands at 1588 cm^{-1} and the broad absorbance centered about 1300 cm^{-1} in the first two minutes of the photoreaction. Also decaying upon exposure is the absorbance at 1705 cm^{-1} associated with the uncoordinated acid. Studies of films composed exclusively of the acid confirm this reactivity. The photosensitivity of the 2-ethylhexanoic acid was illustrated by the decrease in FTIR intensities corresponding to the free acid towards baseline during photolysis of a thin film of the free acid .

With regard to the photolysis of $Ce(O_2CCH(C_2H_5)C_4H_9)_3$, at the same time interval during the photolysis, a similar loss of intensity is observed for the bands at higher (2800-3000 cm^{-1}) energy. These bands approach an absorbance of roughly 60% of the original absorbance. The behavior of the other absorbance bands is remarkably different. The absorbance at 1541 cm^{-1} initially decreases then increases drastically to an absorbance near twice its original value. The absorbance bands at 1460 and 1423 cm^{-1}, in contrast, change very little during the initial stages of photolysis.

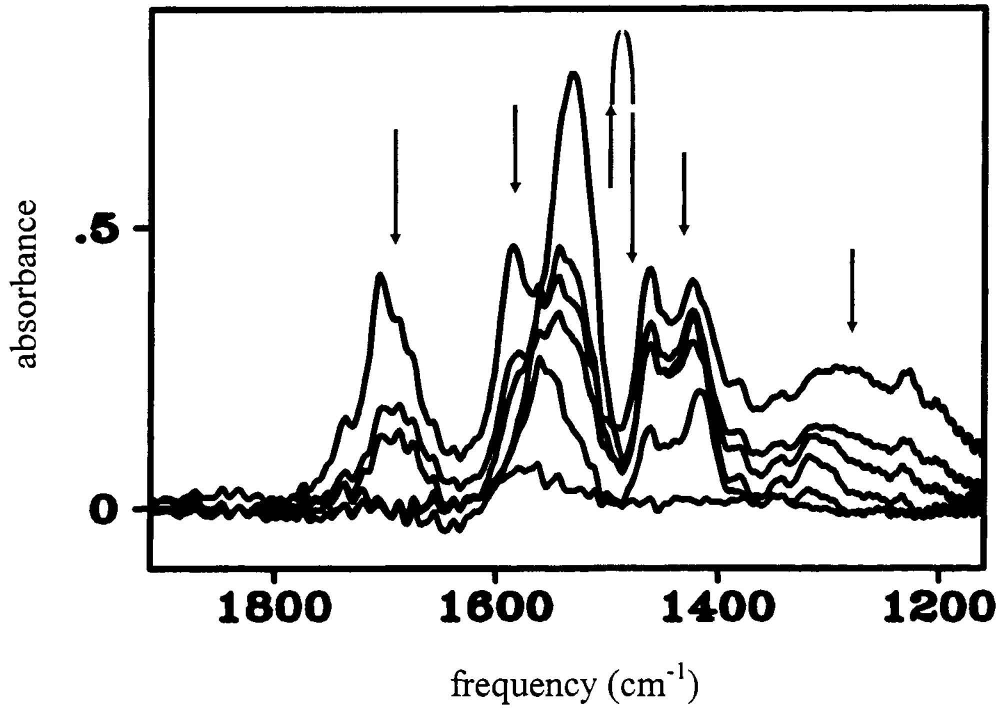

Figure 2.4 Spectral changes upon photolysis of a film of cerium (III) 2-ethylhexanoate for 0, 2, 3, 4, 6, and 14 min. (Note: additional data were collected but were not included for clarity). All FTIR bands decreased in intensities upon photolysis except the band at 1541 cm^{-1} in which the intensity for the band at 1541 during photolysis followed the order of 4, 0, 2, 3, 6 and finally 14 min, with the intensity at 4 min being the strongest.

This initial photoreaction is associated with the conversion of the precursor material from a partially polymeric system containing bidentate carboxylate groups to one in which only monomers with chelating carboxylate group exist. The increase in chelating carboxylate linkage to the central metal led to the increase in intensity of the IR absorbance at 1541 cm^{-1}. The spectral changes upon this reaction are similar to those found upon hydrating the acetate complex, a reaction that also breaks up the polymeric network.[37]

The quantum yield for the initial reaction was determined by monitoring the decay in the absorption band at 1588 cm^{-1}. Plots of absorbance versus photolysis time can be fitted to an exponential decay. The time dependence for the photochemical process is given by Equation 2.1.

$$A_t = A_0 e^{[-(2.303\varepsilon I_0 \Phi)t]} \qquad 2.1$$

In this equation, ε is the extinction coefficient ($mol^{-1}\ cm^2$) at the photolysis wavelength, I_0 is the light intensity (Einstein s), Φ is the quantum yield of the reaction.[40]

A plot of the absorbance versus photolysis time is shown in Figure 2.5. These data fit an exponential decay with an apparent decay constant of $4.1 \times 10^{-3} \pm 1.5 \times 10^{-3}$ s^{-1}. From the measured extinction coefficients, light intensity, and decay constant, the quantum yield for the initial process may be calculated. The quantum yield is calculated to be 1.4 ± 0.5 cerium atom equivalents reacted per photon absorbed.

Following this initial photoreaction a subsequent photoreaction may be monitored. As evident from Figure 2.4, the loss of absorbance associated with bands at 1705 and 1588 cm^{-1} corresponds to a peak in the absorbance of the band centered at 1530 cm^{-1}. Further photoreaction corresponds to the decay of the absorbance at 1530 cm^{-1} along with all other remaining absorbances. This behavior is an indication that all of the carboxylate ligands are lost, leaving cerium as the putative final product of the photochemical reaction. In the presence of air we expect oxidation to yield cerium oxide.

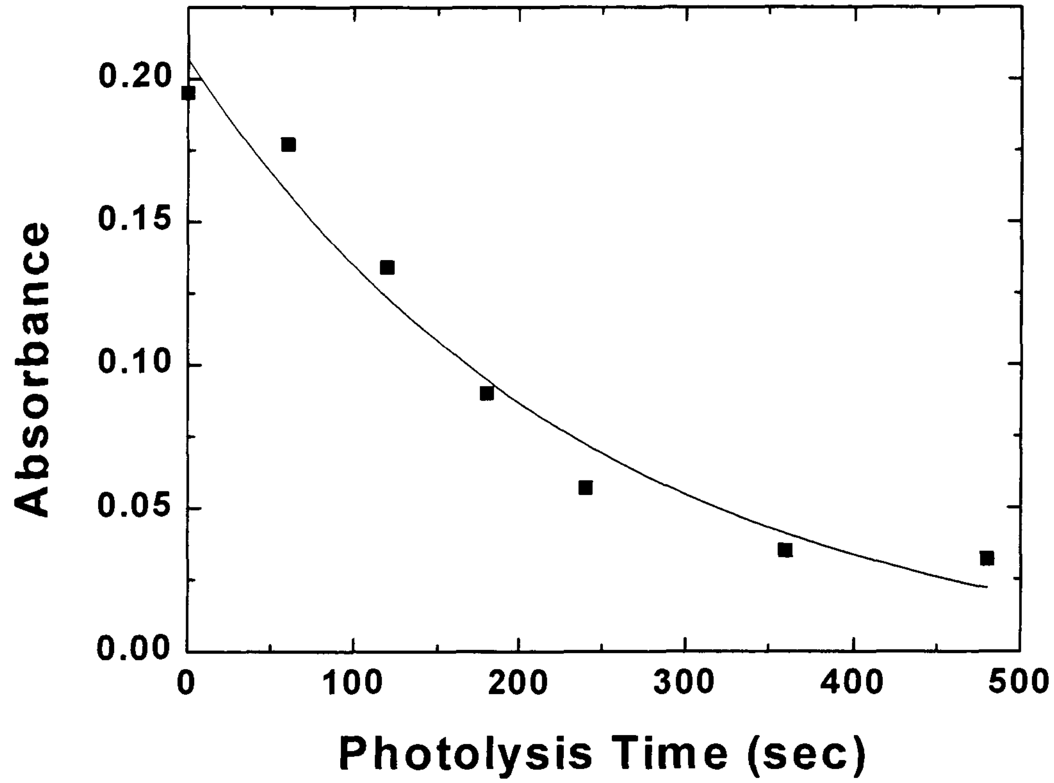

Figure 2.5 Plot showing the changes in absorbance at 1588 cm^{-1} upon photolysis of the spin-cast film of $Ce(O_2CCH(C_2H_5)C_4H_9)_3$. These data are used for the determination of the quantum yield of reaction.

The photolysis of the spin coated sample of $Eu(O_2CCH(C_2H_5)C_4H_9)_3$ results in the spectral changes shown in Figure 2.6. The absorbance bands associated with carboxylate strectches decay in intensity with photolysis time. No apparent intermediate was observed during the photoreaction. The form of the decay is indicative of a single photochemical reaction resulting in the loss of the starting material. No further decay was observed after the sample was photolyzed for more than 360 seconds. In Figure 2.7, a plot of the absorbance at 1531 cm^{-1} versus photolysis time is shown. The line in this plot represents a fit to an exponential decay.

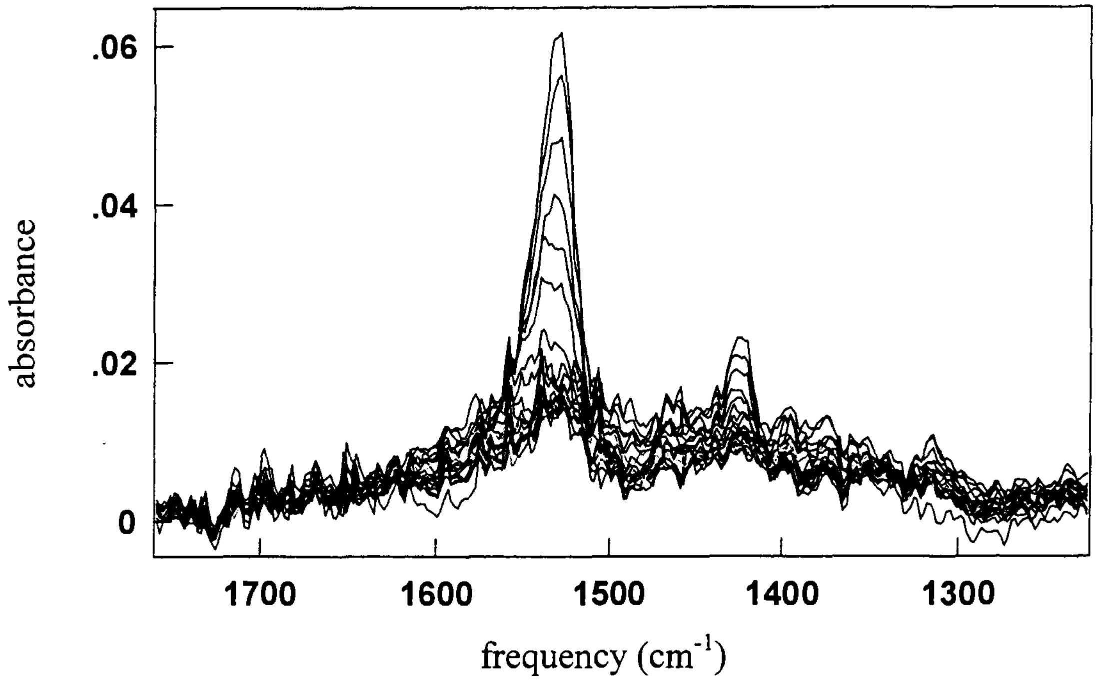

Figure 2.6 The spectra associated with the photolysis of $Eu(O_2CCH(C_2H_5)C_4H_9)_3$ for 0, 10, 30, 60, 90, 120, 180, 240, 300 and 360 seconds. (no further decay was observed after 360 seconds of photolysis). All FTIR bands decreased in intensities upon photolysis

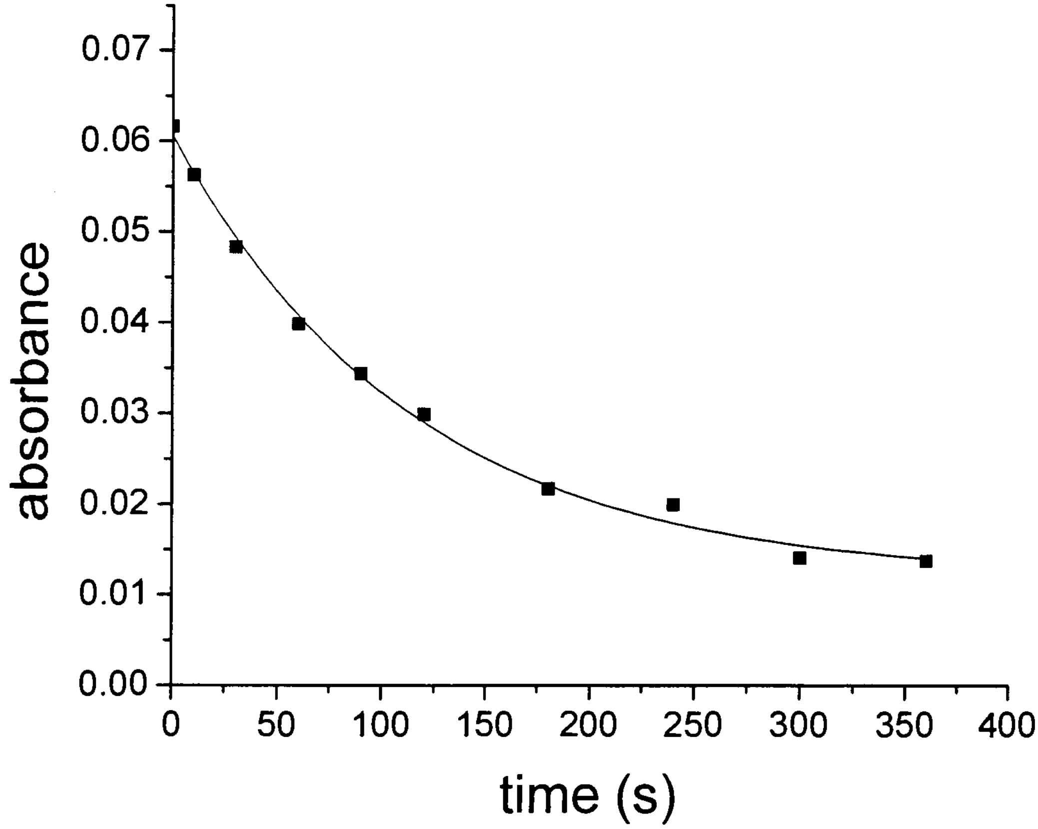

Figure 2.7 The loss of $Eu(O_2CCH(C_2H_5)C_4H_9)_3$ at 1531 cm^{-1} as a function of photolysis time.

The quantum yield for the disappearance of the starting complex was evaluated from the decay rate and the measured light intensity. The quantum yield for the reaction was determined to be 1.8 ± 0.4.

2.2.3 Characterization of the products for the photoreactions of cerium (III) 2-ethylhexanoate and europium (III) 2-ethylhexanoate

2.2.3.1 Elemental compositions of the photolyzed products

The nonvolatile products of the photoreactions were investigated by Auger electron spectroscopy. The Auger electron spectroscopy of the film produced by photolysis of $Ce(O_2CCH(C_2H_5)C_4H_9)_3$ are summarized in Table 2.2. Auger electrons indicative of the presence of cerium, carbon and oxygen were all observed from the surface of the film. The films were also sputtered with argon ions to reveal the interior composition of the films. A decrease in the signal corresponding to carbon was observed during sputtering and in the case of the cerium thin films, sputtering the surface for more than 10 seconds resulted in the loss of signal due to carbon and the observation of peaks only associated with cerium and oxygen. This is consistent with the presence of organic contamination on the sample surface. Continued sputtering results in a near-constant ratio of intensities of Auger peaks associated with the parent metal and oxygen. By comparing with a commercial sample of CeO_2, we find that the prepared amorphous samples have a stoichiometry of Ce_2O_3.

The analysis of the photoproduct of $Eu(O_2CCH(C_2H_5)C_4H_9)_3$ was conducted in a similar manner. The Auger spectra revealed a stoichiometry of Eu_2O_3 with some carbon contamination in the photolyzed film. Sputtering the surface reduced but did not eliminate the carbon. The bulk of the film contained about 10% of carbon.

Table 2.2 The analysis of the surface formed by the reaction of films of $Ce(O_2CCH(C_2H_5)C_4H_9)_3$ and $Eu(O_2CCH(C_2H_5)C_4H_9)_3$ by Auger electron spectroscopy.

Precursor	Sputtering time (seconds)	% Ce	% Eu	% O	% C
$Ce(O_2CCH(C_2H_5)C_4H_9)_3$*	0	8 ± 1		35 ± 3	57 ± 7
	10	39 ± 2		61 ± 3	
	30	40 ± 2		60 ± 3	
$Eu(O_2CCH(C_2H_5)C_4H_9)_3$	0		26 ± 4	50± 3	24 ± 4
	30		32 ± 4	59 ± 2	9 ± 3
Commercial CeO_2	0	29 ± 7		58 ± 7	13 ± 7
	20	37 ± 7		63 ± 7	

* stoichiometry of photolyzed product from $Ce(O_2CCH(C_2H_5)C_4H_9)_3$ determined by comparison with commercial CeO_2 sample

2.2.3.2 Powder X-ray diffraction of the photolyzed films

The cerium oxide film obtained by the photolysis of $Ce(O_2CCH(C_2H_5)C_4H_9)_3$ was analyzed by powder X-ray diffraction. The X-ray spectrum of the cerium oxide film prepared by the PMOD process revealed no diffraction peaks. This indicated the photolyzed film was amorphous in nature.

A europium oxide film was examined in a similar fashion. The X-ray spectrum of the europium oxide film also revealed no diffraction peaks, indicating the amorphous nature of the photolyzed film.

2.2.3.3 Characterization of volatile products from the photoreactions of $Ce(O_2CCH(C_2H_5)C_4H_9)_3$ and $Eu(O_2CCH(C_2H_5)C_4H_9)_3$

Thin films of $Ce(O_2CCH(C_2H_5)C_4H_9)_3$ and $Eu(O_2CCH(C_2H_5)C_4H_9)_3$ were photolyzed under a static vacuum for two hours and their volatile products were analyzed by mass spectrometry.

For $Ce(O_2CCH(C_2H_5)C_4H_9)_3$, mass spectral analysis indicated the presence in the gas phase of species with molecular weights of m/e 44, 98 and 100. The peak at 44 was assigned to CO_2. The peak at 98 and 100 were assigned to heptene and heptane respectively. The release of CO_2 from carboxylate ligands associated with photolysis is the expected reaction with much precedent in both solution and solid state.[7, 41, 42] Support for these assignments come from the observation at of peaks at m/e of 85, 72, 71, 70, 57, 56, 43, 42, 41, 29 and 27, consistent with the fragmentation pattern of heptane as well as at m/e of 83, 70, 69, 67, 57, 56, 55, 54, 53, 51, 42, 41, and 27, consistent with the fragmentation of heptene.

A similar fragmentation pattern was obtained for $Eu(O_2CCH(C_2H_5)C_4H_9)_3$ when the volatile products of the photoreaction were evaluated by mass spectroscopy.

Taking into account both the Auger and mass spectroscopic results, we can write a balanced equation for the photoreaction. The chemistry resulting from the photolysis of

$Ce(O_2CCH(C_2H_5)C_4H_9)_3$ and $Eu(O_2CCH(C_2H_5)C_4H_9)_3$ are described by Equation 2.2 and 2.3 respectively.

$$2\ Ce(O_2CCH(C_2H_5)C_4H_9)_3 + 3/2\ O_2 \xrightarrow{h\nu} Ce_2O_3 + 6CO_2 + 3\ CH_3(CH_2)_5CH_3 + 3\ CH_3CH{=}CH(CH_2)_3CH_3 \qquad 2.2$$

$$2\ Eu(O_2CCH(C_2H_5)C_4H_9)_3 + 3/2O_2 \xrightarrow{h\nu} Eu_2O_3 + 6\ CO_2 + 3\ CH_3(CH_2)_5CH_3 + 3\ CH_3CH{=}CH(CH_2)_3CH_3 \qquad 2.3$$

2.2.3.4 Determination of radical chain reaction

In an attempt to determine the possibility of a free radical chain mechanism, a film of codeposited 2, 2'-Azobisisobutyronitrile (AIBN), a known source of radicals, and $Ce(O_2CCH(C_2H_5)C_4H_9)_3$ was prepared and allowed to react at room temperature in the dark. The FTIR spectral changes are recorded and the overlay spectra of the initial FTIR spectrum and the FTIR spectrum after 48 hours in the dark are shown in Figure 2.8. It was found the intensities of the FTIR absorption peaks decreased. The decrease in the intensity of the FTIR absorption peak indicates that the radicals generated by AIBN were capable of initiating the decomposition of the cerium precursor film.

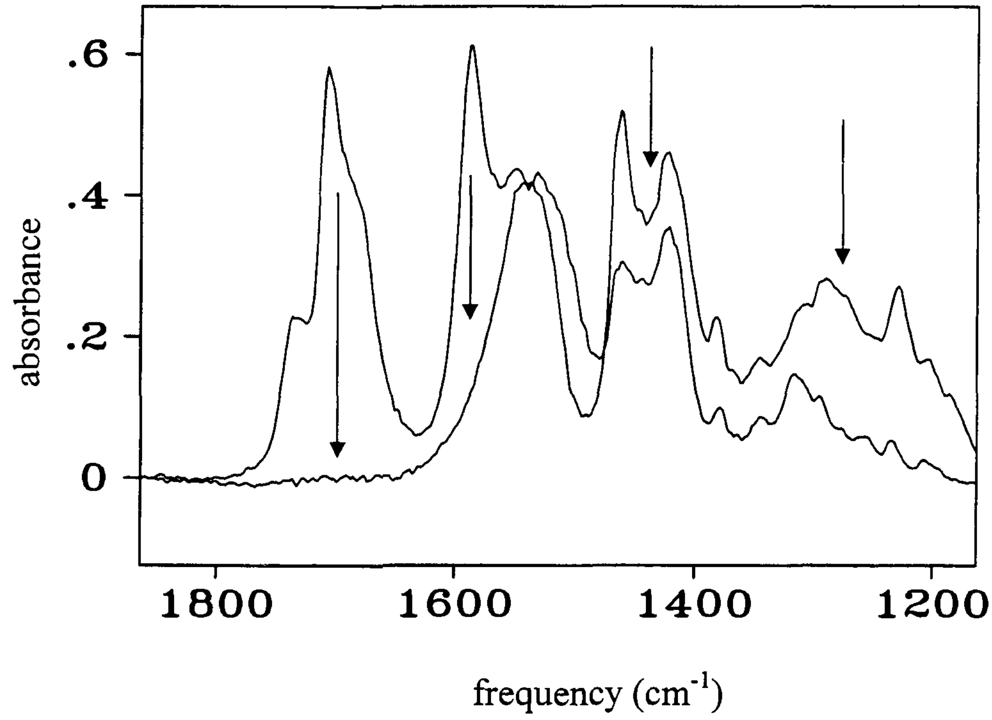

Figure 2.8 Spectral changes showing the thermal reactivity of a film composed of cerium(III) 2-ethylhexanoate and AIBN. The spectra were obtained upon deposition and after 48 hours in the dark. All FTIR bands decreased in intensities after 48 hours.

2.2.3.5 Photolithography of $Ce(O_2CCH(C_2H_5)C_4H_9)_3$ *and* $Eu(O_2CCH(C_2H_5)C_4H_9)_3$

In order to illustrate that PMOD could be used to photopattern materials a contact mask lithography experiment was conducted. A film of $Ce(O_2CCH(C_2H_5)C_4H_9)_3$ was formed by spin coating onto a silicon chip. The film was irradiated through a contact mask for 1 hour. The silicon chip was then rinsed with dichloromethane and the resultant pattern illustrated in Figure 2.10 became apparent. The line width in the figure is ca. 1.5 μm wide. This is not meant to show the limiting line width but rather that this process is capable of reasonable resolution patterning. Films of $Eu(O_2CCH(C_2H_5)C_4H_9)_3$ were also irradiated through a contact mask and comparable patterns were obtained.

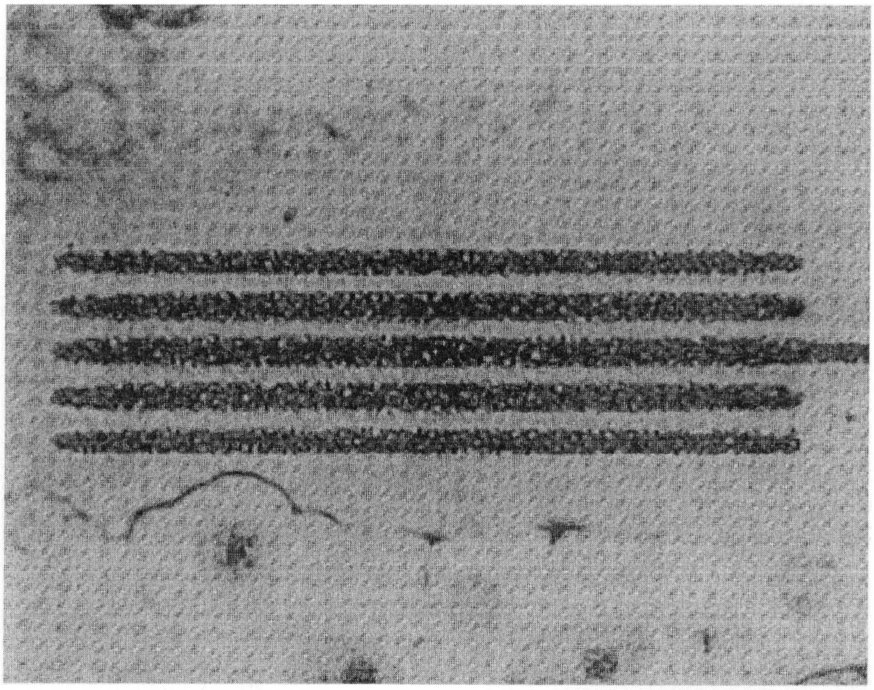

Figure 2.10 Lithographic pattern of Ce_2O_3 produced by the photolysis of a film of cerium (III) 2-ethylhexanoate through a mask. Each of the four complete lines shown is 50 microns long.

2.3. Discussion

The type of molecule used for this series of complexes is illustrated in Figure 2.2. Of importance in the precursor design is the use of the carboxylate ligand. This ligand performs two functions in the molecule. The carboxylate binds the organic portion to the central metal. It also is the group which is photochemically activated. A charge transfer transition excites an electron from the carboxylate ligand to the cerium or europium metal, leaving the CO_2 linkage as formally neutral. This results in a loss of bonding between the ligand and the metal ion and results in the extrusion of CO_2 from the molecule. The loss of CO_2 frees the organic portion from the metal center. The organic group serves to control the intermolecular forces between the molecules. These forces will affect both the tendency for crystallization and the rate of molecular diffusion on the surface. In the present series of molecules we have used the 2-ethylhexanoate ligand which has a chiral center. This was not resolved but rather results in the presence of several isomers in the film. The presence of all these isomers will further inhibit the possibility of crystallization.

The overall reaction is as shown in Equation 2.2 or 2.3. The mechanism of this reaction is best described by considering the reaction of a monomer. The simplest reaction we can consider is the photochemical charge transfer resulting in the loss of bonding character between one CO_2 fragment and the cerium or europium metal and the 3-heptyl fragment. This and the subsequent fragmentation is shown in Figure 2.11. The CO_2 produced in this reaction was one observed product. The resulting 3-heptyl fragment may abstract hydrogen from a second heptyl fragment to yield both the observed heptane and heptene. The disproportionation of the 3-heptyl radicals was evidenced by the presence of peaks of 100 and 98 from the mass spectrometry data during the characterization of volatile products from the photoreactions. The Ce (II) or Eu (II) intermediate formed after the loss of the initial carboxylate ligand is unstable to thermolysis and fragments as shown in Figure 2.11. While Eu (II) complexes are know, all examples in literature are consistent with high coordination geometry.[43] In the case in our experiment, the Eu (II) intermediate formed had a low coordination geometry. This low coordination Eu (II) intermediate is apparently unstable, leading to the formation of europium metal and more ligand fragments.

The net result of the photolysis of cerium (III) or europium (III) 2-ethylhexanoate is the formation of heptyl radicals and CO_2 and the formation of free cerium or europium atoms. The cerium or europium atom is readily oxidized in the presence of air.

It is also important to point out that the proposed mechanism was deduced from volatile fragments detected by mass spectrometry when the precursor film was photolyzed in vacuum. When the precursor film is photolyzed under ambient conditions, alternative mechanism such as oxidation of the unstable Ce (II) or Eu (II) intermediates by oxygen (in stead of thermal decomposition to Ce or Eu metal and ligand fragments) is also a possibility.

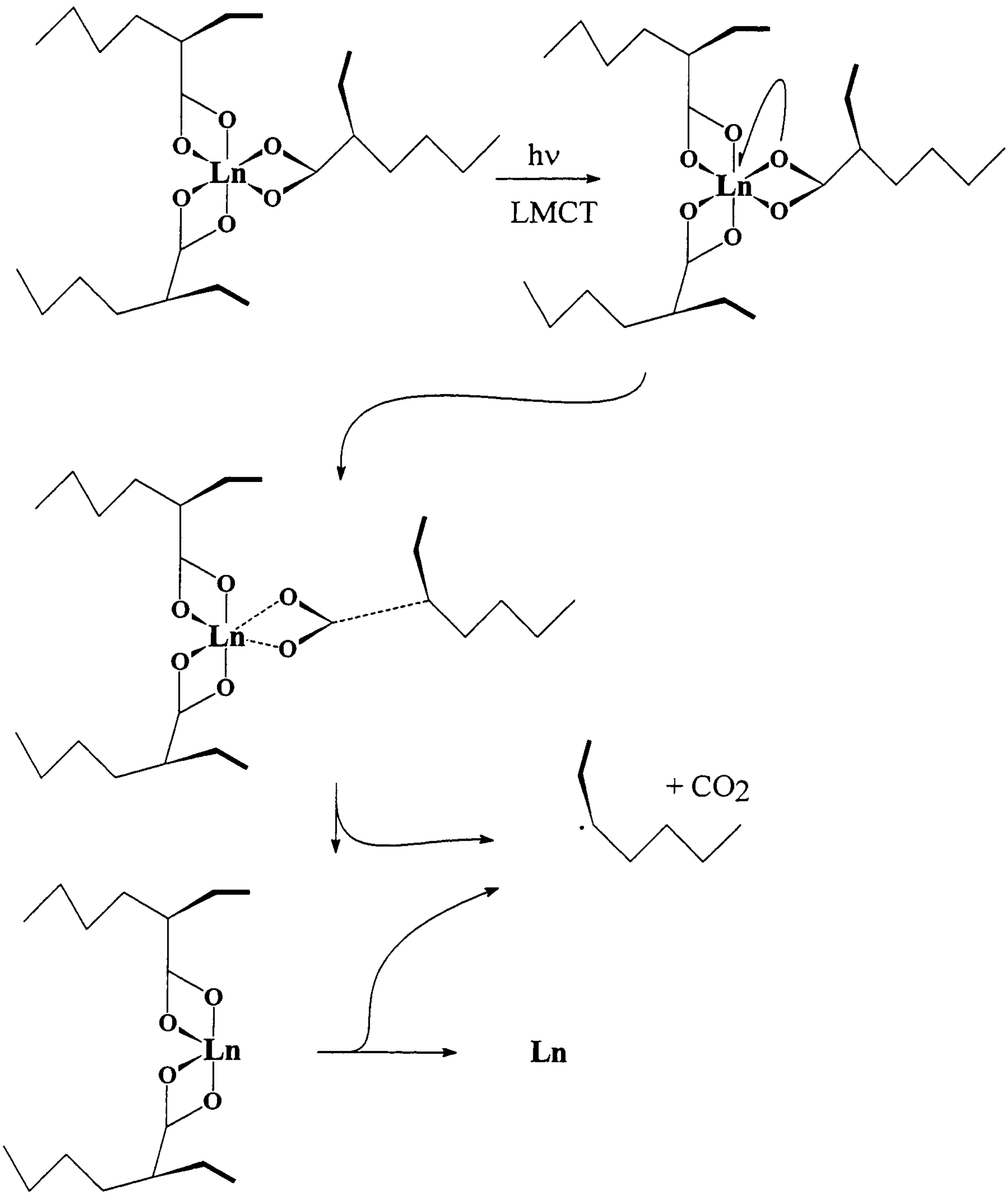

Figure 2.11 Scheme showing the mechanistic details of the photoreaction of the cerium or europium 2-ethylhexanoates (Ln = Ce or Eu).

The above scheme provides a mechanism that explains the formation of the products observed in the reaction. One observation which is not explained by the above is the quantum yield which is in excess of one for the photoreactions. In order to explain this observation one must invoke a mechanism involving either a chain process or at least a subsequent non chain reaction which results in the destruction of a second molecule of the starting material.

In an attempt to determine the possibility of a radical-induced reaction for the precursor, a film of codeposited 2, 2'-Azobisisobutyronitrile (AIBN) and $Ce(O_2CCH(C_2H_5)C_4H_9)_3$ was prepared and allowed to react at room temperature in the dark. AIBN is a known source of radicals and reacts according to Equation 2.4.

$$(CH_3)_2(CN)CNNC(CN)(CH_3)_2 \longrightarrow 2\ {\bullet}C(CN)(CH_3)_2 + N_2 \qquad 2.4$$

It was found that after the film was left in the dark for 48 hours, a decrease in the FTIR intensities of the absorption peaks was observed as indicated in Figure 2.8. This suggests that the radicals formed in this reaction were capable of initiating the decomposition of the precursor molecules.

One proposal for a radical induced reaction is the abstraction of a hydrogen atom from the 2-ethylhexanoate ligand of a complex. This may render the ligand unstable and lead to the fragmentation of the complex thereby regenerating the radical, resulting in chain propagation. In Figure 2.12, this process is outlined for the case of a trimeric unit. The attack on a polymer unit by the 3-heptyl radical is by the abstraction of a hydrogen on the 2-ethylhexanoate ligand. This results in the formation of the two cerium or europium (III) monomers, an unstable cerium or europium (II) complex, CO_2, heptane and 2-heptene. The cerium or europium (II) complex presumably reacts as shown in Figure 2.11.

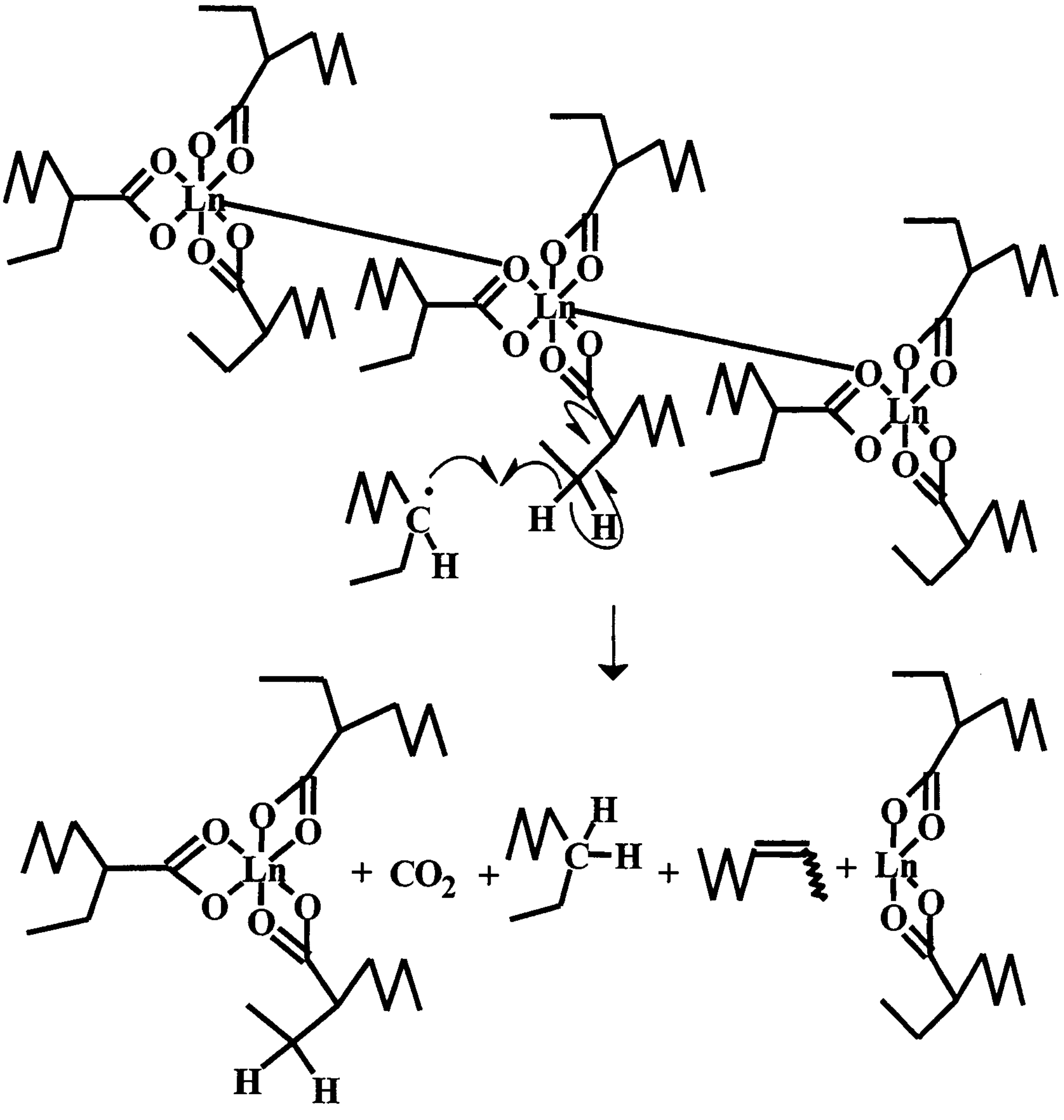

Figure 2.12 Proposed free radical component of the reaction by the abstraction of hydrogen atom (Ln = Ce or Eu).

It is however not clear why the hydrogen abstraction would occur at the position β to the carboxylate leading to the formation of the observed products. The most easily abstracted hydrogen atom is expected to be the one on the most heavily substituted carbon atom. It is not clear if the radical would be able to abstract from this carbon or how this may generate the products. This complication prompts us to suggest an alternative mechanism.

The initial photoproduct formed following the loss of a single carboxylate ligand is the Ce(II) or Eu(II) species. This complex is unstable and is expected to undergo decomposition, however, it may be possible that an electron transfer reaction occurs prior to the decomposition. Such an electron transfer would occur between this species and a Ce(III) or Eu(III) starting complex as shown in Figure 2.13.

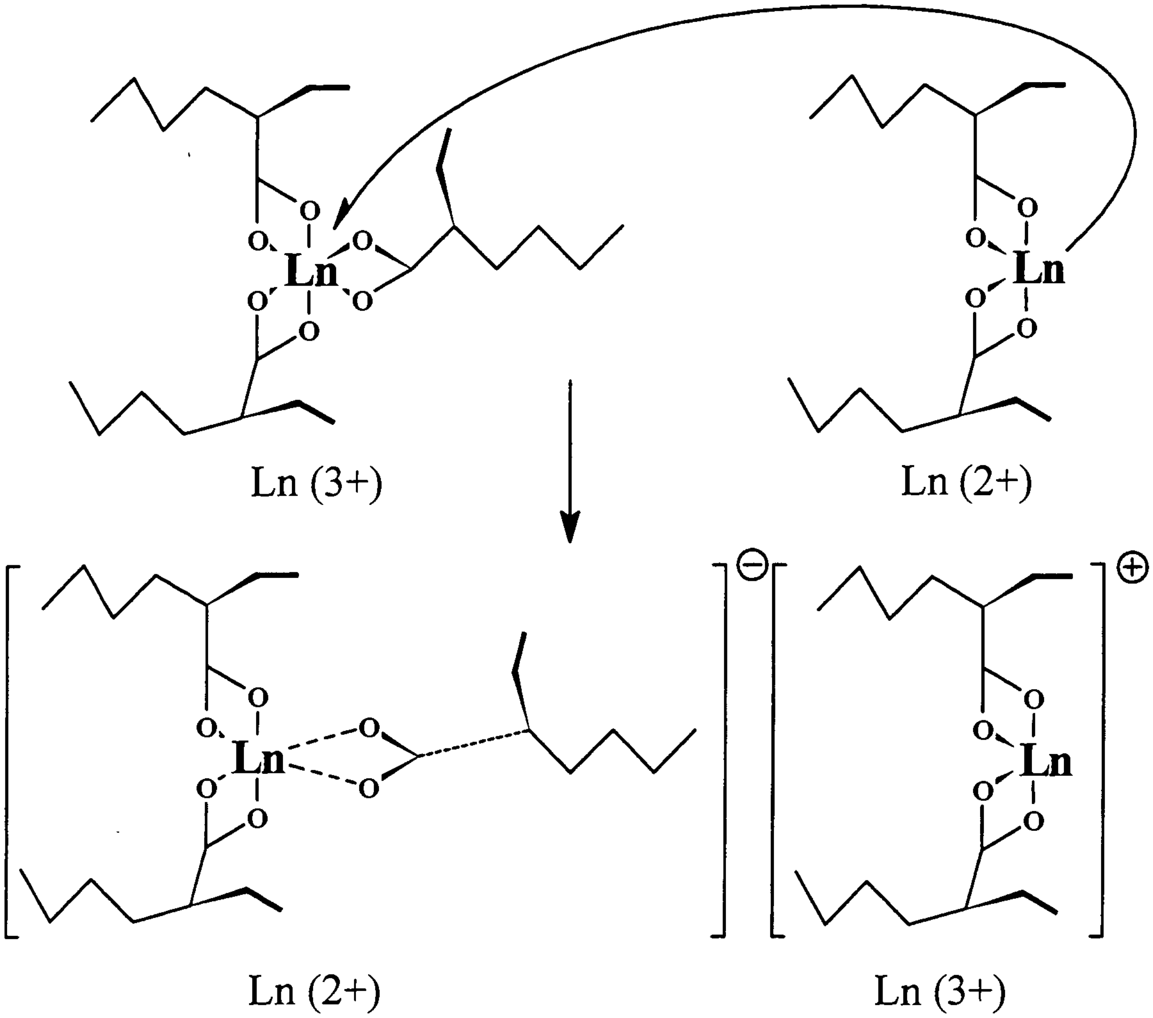

Figure 2.13 Scheme outline the initial electron transfer to form species which could account for the observations of quantum yields in excess of one (Ln = Ce or Eu).

The six coordinate Ce(II) or Eu(II) is not expected to be stable and the ejection of one carboxylate ligand would result in the generation of the four coordinate Ce(I) or Eu(I) species. One possibility at this point is the reverse electron transfer between the four coordinate Ce(I) or Eu(I) and Ce(III) or Eu(III) species and the generation of two

Ce(II) or Eu(II) four coordinate species. These could then either thermally decompose or undergo electron transfer reactions with an additional molecule of the starting material.

The scenario above presents only one possible route by which the electron transfer process may result in a quantum yield greater than one. Several other related mechanisms differing in the point at which the electron transfer occurs may also be envisaged. Our data do not allow us to decide between these options. The electron transfer mechanism does have the advantage over the simple radical reaction in that it does not require the unusual abstraction of a specific hydrogen from the coordinated ligand.

2.4. Conclusions

In this chapter, the photoreactions of thin films of cerium (III) and europium (III) 2-ethylhexanoates under ambient conditions leading to amorphous films of cerium and europium oxides were presented. The photoreactions involved free radical chemistry in the solid film. Photolithography could be used to control the deposition of this material to produce micron-sized patterns of cerium or europium oxides.

2.5. Experimental

2.5.1 Instrument and materials

The precursor complexes, cerium (III) 2-ethylhexanoate (solution in 2-ethylhexanoaic acid) and europium (III) 2-ethylhexanoate (white solid) were purchased from Strem Chemical. Fourier transform infra-red (FTIR) spectra were obtained with 4 cm^{-1} resolution using a Bomem MB-120 spectrometer. UV/Visible spectroscopy was monitored with a HP 8452A diode array spectrometer. Auger spectra were obtained with a PHI double pass CMA at 0.85 eV resolution. Spin coating was done with a Laurell Technology Corporation spin coater. Optical microscopy was conducted with a Leitz Laborlux 12 ME S. Light intensities were measured with an International Light IL 1350 radiometer. The silicon chips used were cut from wafers of p-type silicon (100) obtained from Shin Etsu. X-ray diffraction spectra were obtained using a Phillips X-ray diffractometer operating at 35 kV and 45 A. The X-ray source was a Cu Kα (1.54 A) beam. The machine resolution was 0.05 degrees.

2.5.2 Calibrations of spectroscopic absorption

Calibration of the absorption in the infrared was accomplished in the following manner. A solution of cerium (III) 2-ethylhexanoate in methylene chloride was prepared by diluting the original solution such that the concentration of the final solution was 8.6 x 10^{-3} M. Single drops of this were deposited on a silicon chip in an area of 0.8 cm^2 resulting in an areal coverage per drop of 3.0 molecules/A^2. The FTIR of the deposited film was obtained as each drop was added and is presented in Figure 2.14. Also in Figure 2.14 is a plot of the absorbance vs. coverage. From the slope of this line the extinction coefficient for the band at 1588 cm^{-1} is 0.013 A^2/molecule (or 8.1 x 10^5 cm^2/mol). The extinction coefficients for each absorption band may be obtained from a comparison with this number. The absorption bands in the electronic spectra were calibrated based on the FTIR. A single film was cast on CaF_2 and both FTIR and electronic spectroscopy was conducted on this sample. The absorbances for this film were found to be 0.1 at 254 nm and 0.38 at 1588 cm^{-1}. By the relative absorbances and using the known extinction coefficients in the IR the extinction coefficient at 254 nm is 0.0035 A^2/molecule (or 2.1 x 10^5 cm^2/mol).

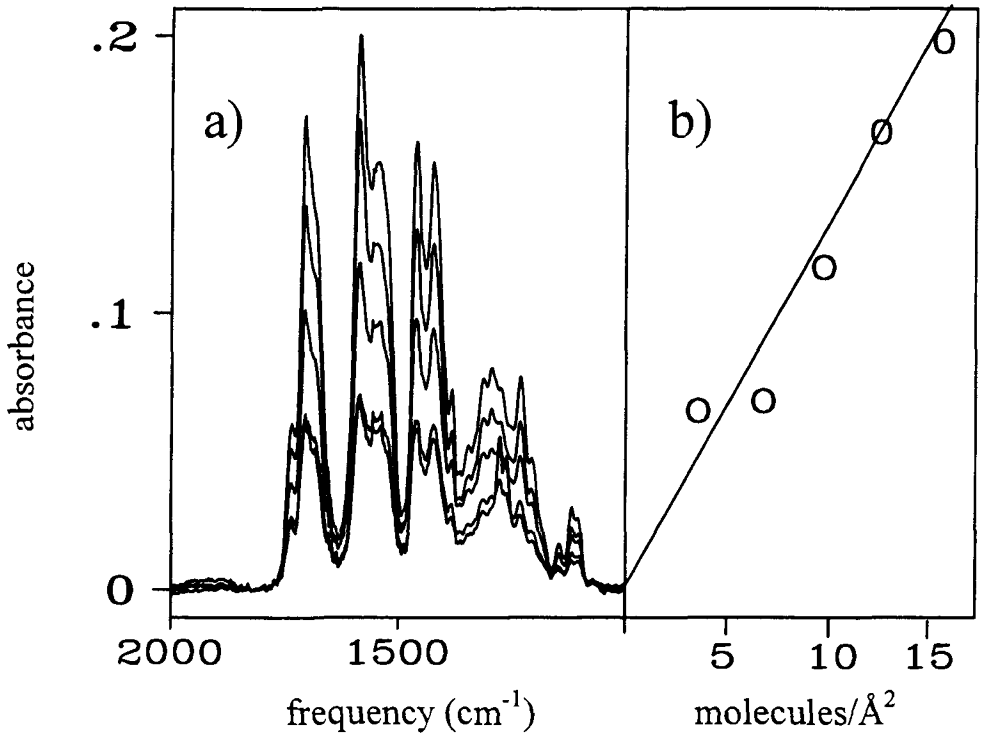

Figure 2.14 Plot showing a) the FTIR of the carboxylate region of a film formed by the deposition of cerium (III) 2-ethylhexanoate coverages of 3, 6, 9, 12, and 15 molecules/A^2 with intensities of the FTIR bands increased for increasing coverages and b) a plot of the absorbance at 1588 cm^{-1} vs. coverage for this data.

Similar experiments were conducted with europium (III) 2-ethylhexanoate and the results are summarized in Table 2.1.

2.5.3 Photolysis of films of cerium and europium (III) 2-ethylhexanoates

A silicon chip (1x1.5 cm^2) was cut from a wafer and thin amorphous films of the precursor, cerium (III) and europium (III) 2-ethylhexanoate, were prepared by spin coating the silicon chip from a solution of the complex in dichloromethane and toluene respectively. The precursor solutions were prepared by adding a few drops of cerium (III) 2-ethylhexanoate into about 1 ml of dichloromethane and about 200 mg of europium (III) 2-ethylhexanoate into about 1 ml of toluene. Precursor film was prepared adding a drop of precursor solution onto a silicon chip at approximately 2000 rpm. The FTIR of the samples were obtained and the samples then photolysed. The FTIR were again obtained and the process repeated until no absorbance associated with the carboxylate group was evident from the FTIR. By monitoring both the light intensity (constant at 2.73 mW/cm^2 for cerium complex and 2.52 mW/cm^2 for europium complex) and the extent of reaction, the apparent quantum yields for the two photoprocesses were determined. The samples were then subjected to Auger electron spectroscopy and powder X-ray diffraction.

2.5.4 Characterization of the photoreactions for cerium (III) and europium (III) 2-ethylhexanoates

In order to determine the volatile products for the photoreactions, films of cerium and europium (III) 2-ethylhexanoates were photolysed in a sealed, evacuated vessel. Following each photolysis the contents of the head space of the reactor were analyzed. The analysis was conducted by injecting the gas contents directly into the chamber of the mass spectrometer.

In a similar experiment a film of both AIBN and cerium (III) 2-ethylhexanoate was cast by spin coating. The thermal chemistry of this mixture, in the dark, was monitored by FTIR.

Chapter 3

Photochemical Metal Organic Deposition (PMOD) of Insulating Aluminum Oxide films

3.1.Introduction

In this chapter a method for the deposition of patterned aluminum oxide films from thin films of aluminum complexes by photochemical metal organic deposition (PMOD) is presented. Aluminum oxide is an insulator and has uses in both sensors and electronic devices.[44-45] Aluminum oxide has been deposited by a variety of methods including simple and plasma-enhanced chemical vapor deposition (CVD), atomic layer epitaxy (ALE), and vacuum evaporation.[44-47] None of these methods result in the direct patterning of the aluminum oxide. PMOD offers the advantage that it can be conducted lithographically to produce patterned structures without the requirement of separate masking and etching.

Photochemical methods for the deposition of metal-containing films from thin films of metal organic complexes have been developed.[7-9, 48-53] In this process, typically a thin film of precursor molecules is deposited by spin coating. The film is then irradiated and the precursor fragments generate metals, which remain in the film, and volatile organic by-products. Deposition of a variety of metal and metal oxides by this process has been successfully demonstrated.[7-9, 48-53] Irradiation of the films through a mask results in the generation of patterned films of the metal or metal oxide. A wide variety of transition metal complexes have been explored for use as precursors for the PMOD process. In Chapter 2, the use of the PMOD process in the preparation of rare earth metal oxides thin films was introduced. In this chapter, we will extend the PMOD process to main group metal oxides in the study of the deposition of aluminum oxide. The PMOD process using a series of aluminum β-diketonate and aluminum mixed alkoxide β-diketonate precursors in the preparation of aluminum oxide will be presented.

Metal β-diketonates have intense charge transfer transitions in the near-UV region. It was also known that metal β-diketonate complexes fragment upon irradiation, making them suitable candidates for PMOD precursors.[54] In this chapter we will also study the effect of purity of the final product upon substitution of β-diketonate for alkoxide ligands in the precursor molecules.

3.2. Results

3.2.1 Characterization of Aluminum β-diketonate precursors films

Three precursors are used in this study and their structures are represented in Figure 3.1.

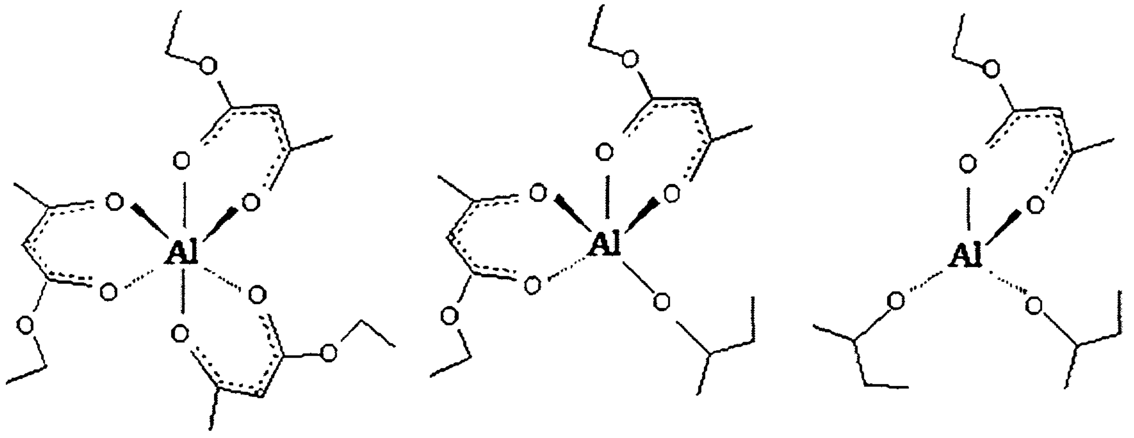

$Al(EtOacac)_3$ $Al(EtOacac)_2OBu$ $Al(EtOacac)(OBu)_2$

Figure 3.1 Aluminum β-diketonate and mixed alkoxide β-diketonate precursors.

The complexes being studied were all spin coated on silicon substrate to provide optical quality thin films for spectroscopic study. A typical FTIR spectrum of a thin film of $Al(EtOacac)(OBu)_2$ is shown in Figure 3.2. All of the aluminum complexes have similar FTIR spectra and their assignments, based on comparison with $Al(acac)_3$ complexes are summarized in Table 3.1.[54]

The FTIR spectrum of $Al(EtOacac)(OBu)_2$ shown absorptions between 3000 and 2800 cm^{-1}; they are associated with CH stretching modes of the ligands. There are a number of intense peaks between 1700 cm^{-1} to 1000 cm^{-1} and they are associated with the β-diketonate ligands. The absorption at 1611 cm^{-1} is assigned to ν(CC) coupled with ν(CO). The peak at 1527 cm^{-1} is assigned to ν(CO) coupled with ν(CC). Peaks at 1304

cm^{-1} and 1298 cm^{-1} are assigned to ν(CC) coupled with ν(C-CH_3) and δ(CH) coupled with ν(C-CH_3) respectively.[54]

The FTIR spectra of the other two precursors are similar to that of Al(EtOacac)$(OBu)_2$ and the data is summarized in Table 3.1.

The UV-vis absorption spectrum of Al(EtOacac)$(OBu)_2$ indicates an absorption maximum at 270 nm, associated to the charge transfer transition. The other two precursors have similar UV-vis absorption spectra and the results are summarized in Table 3.2.

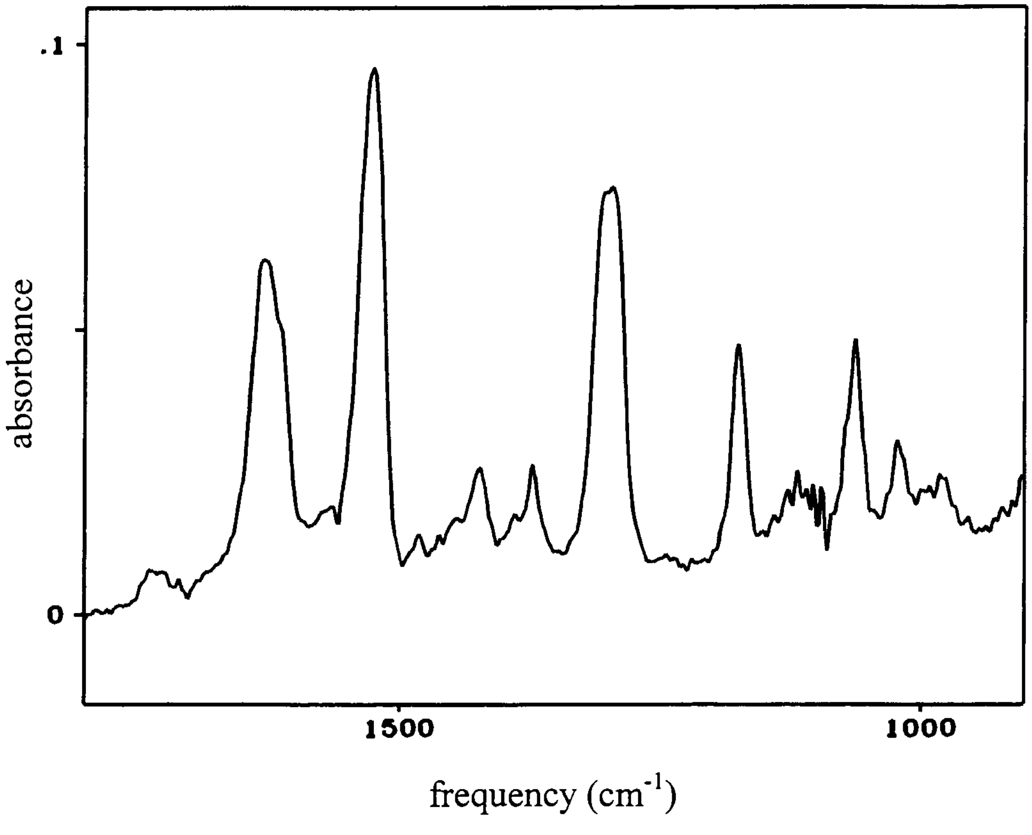

Figure 3.2 FTIR spectrum of Al(EtOacac)$(OBu)_2$.

Table 3.1 FTIR data for aluminum complexes.

Complex	ν (cm^{-1})	(ε 10^6 cm^2/mol)	assignments[54]
Al(EtOacac)$_3$	1610	(5.52)	ν(CO) + ν(CC)
	1523	(6.63)	ν(CO) + ν(CC)
	1294	(5.98)	ν(CC) + ν(C-CH$_3$)
	1178	(4.20)	δ(CH) + ν(C-CH$_3$)
Al(EtOacac)$_2$OBu	1608	(1.05)	ν(CO) + ν(CC)
	1525	(1.41)	ν(CO) + ν(CC)
	1304	(1.09)	ν(CC) + ν(C-CH$_3$)
	1178	(0.47)	δ(CH) + ν(C-CH$_3$)
Al(EtOacac)(OBu)$_2$	1611	(0.84)	ν(CO) + ν(CC)
	1527	(1.56)	ν(CO) + ν(CC)
	1298	(1.23)	ν(CC) + ν(C-CH$_3$)
	1175	(0.61)	δ(CH) + ν(C-CH$_3$)

Table 3.2 UV-visible spectral data of the aluminum complexes.

Complex	λ (nm)		(ε 10^7 cm^2/mol)
$Al(EtOacac)_3$	272	(max)	(8.72)
	254		(5.10)
$Al(EtOacac)_2OBu$	270	(max)	(1.96)
	254		(1.16)
$Al(EtOacac)(OBu)_2$	270	(max)	(2.32)
	254		(1.12)

3.2.2 Photochemistry of aluminum β-diketonates and mixed alkoxide β-diketonates

Spectral changes upon irradiation of a thin film of $Al(EtOacac)(OBu)_2$ are illustrated in Figure 3.3. The region shown indicates the main absorption bands associated with the β-diketonate ligands. When the film was exposed to 254 nm irradiation, the absorption bands decayed with a half life of about 50 minutes. During the reaction the spectral features decrease in proportion to their initial intensity, indicative of the absence of thermally stable intermediates during the photoreaction. There was no evidence for the presence of the starting material by the end of the photoreaction. Similar results were observed for the other two aluminum precursors.

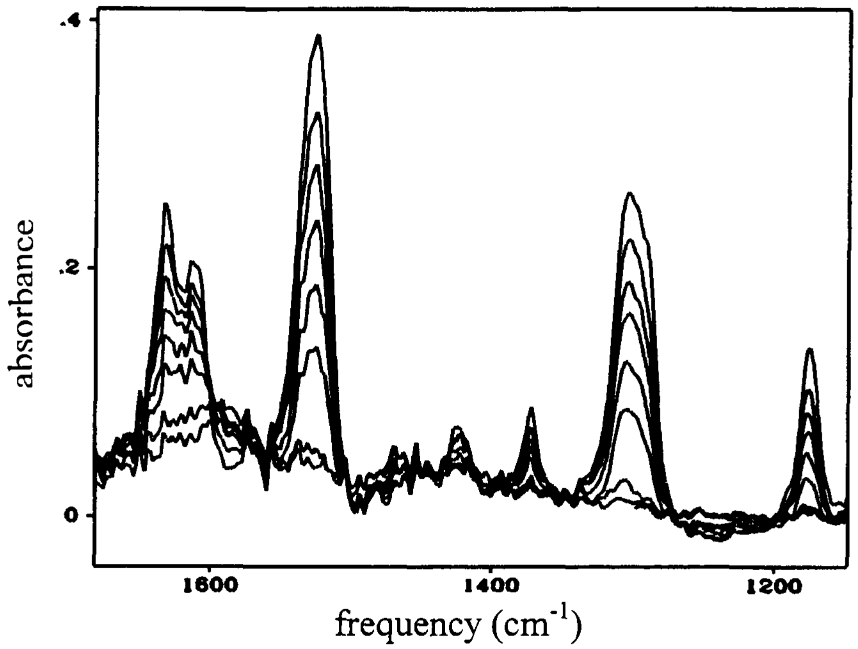

Figure 3.3 FTIR spectra associated with the photolysis of an amorphous film of Al(EtOacac)(OBu)$_2$ for 0, 10, 20, 30, 50, 70, 140 and 205 min. All FTIR intensities decreased upon photolysis

3.2.3 Determination of the quantum yield for the photoreaction

The efficiency of the photoreaction is interpreted by evaluating the decomposition quantum yield of the reaction. Previous studies have provided an equation, which describes the time evolution of the extent of photoreaction as a function of photolysis time, and is represented as Equation 3.1.[55, 56]

$$\frac{dX}{(A^0X/(A^0X+A^f-A^fX))(1-e^{-2.303(A^0X+A^f-A^fX)})}=\frac{\Phi I^0dt}{c^0} \quad 3.1$$

From Equation 3.1, the mole fraction, X, of the starting material is related to the photolysis time, *t*, incident light intensity, I^0, initial film concentration, c^0, initial and final absorbance at the irradiation wavelength, A^0 and A^f and quantum yield, Φ.

In order to solve for the quantum yield, Φ, the decomposition quantum yield of $Al(EtOacac)(OBu)_2$ was determined by following the decay of the FTIR absorption bands upon photolysis. The relationship between the FTIR absorbance at 1298 cm^{-1} and the photolysis time was obtained and the data was fit in a numerical integration sequence with the quantum yield as the only variable in the fitting procedure. The simulation from the integration is given in Figure 3.4. The resultant quantum yield for the photoreaction was found to be 0.027.

The confidence in the estimate of the quantum yield obtained by this method is guarded as the method provides no simple process to access the error. Given this limitation, the error is conservatively reported as 50 %.

Similar experiments were carried out for the other precursors and the simulations from the numerical integration are illustrated in Figure 3.5 and 3.6. The decomposition quantum yields for the precursors and the results are summarized in Table 3.3.

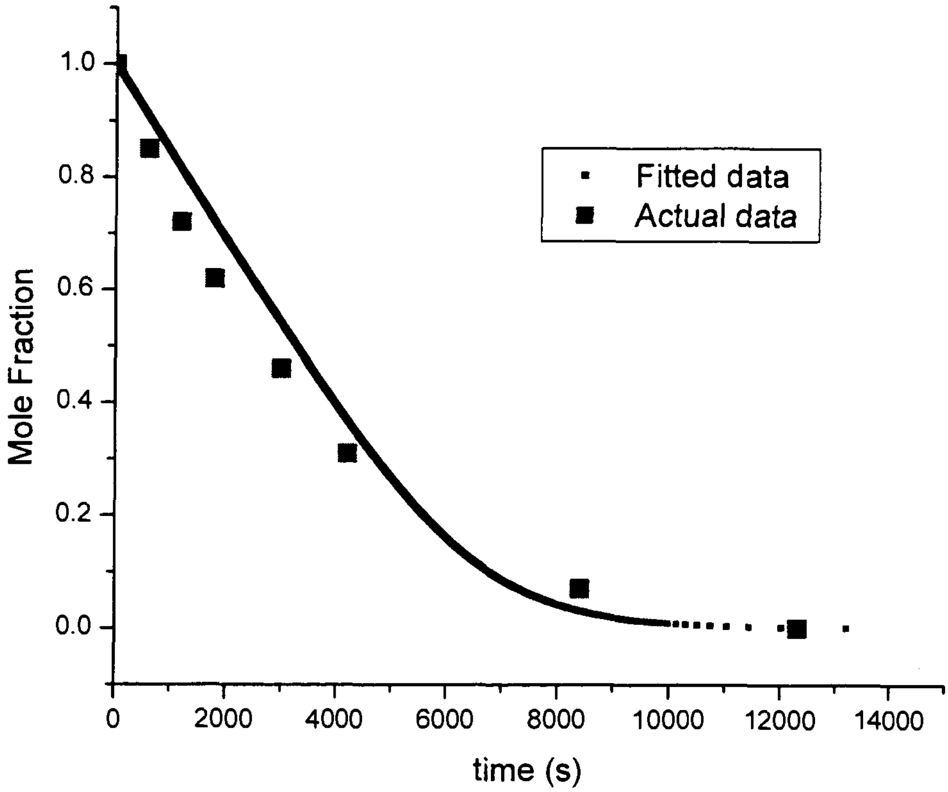

Figure 3.4 A plot of mole fraction against photolysis time for Al(EtOacac)(OBu)$_2$ in which the numerical integration with a quantum yield of 0.027 was fitted against experimental data.

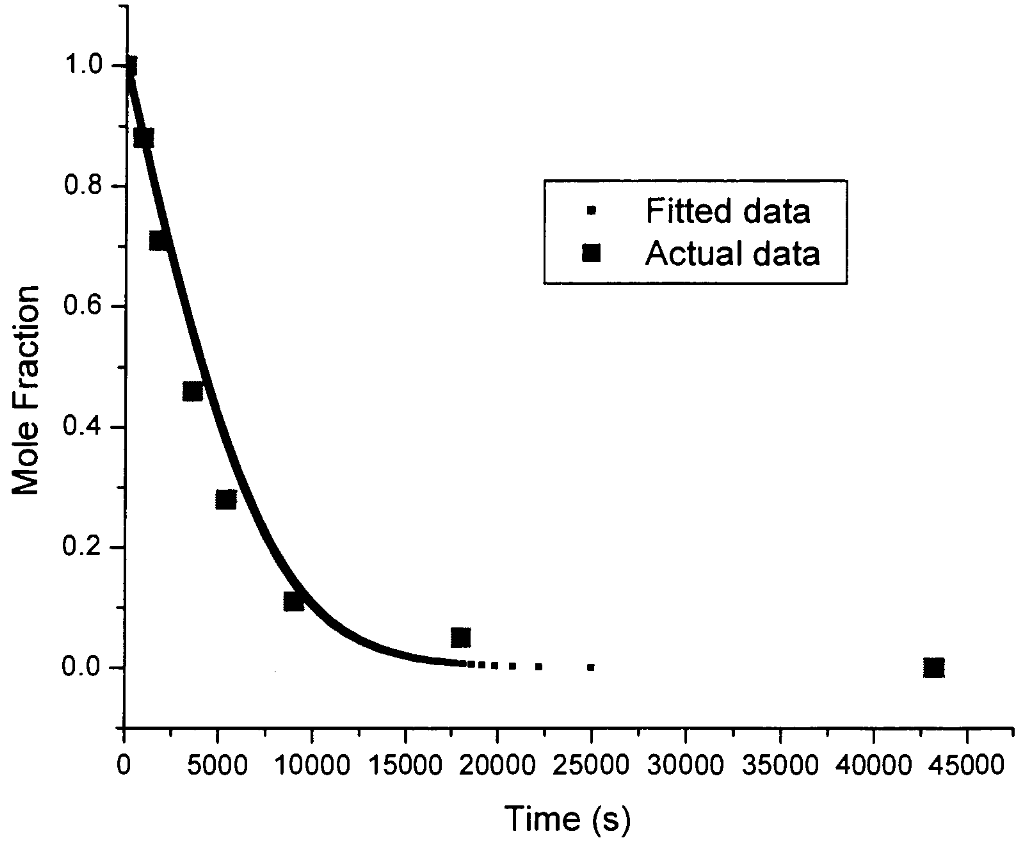

Figure 3.5 A plot of mole fraction against photolysis time for Al(EtOacac)$_2$(OBu) $_2$ in which the numerical integration with a quantum yield of 0.015 was fitted against experimental data.

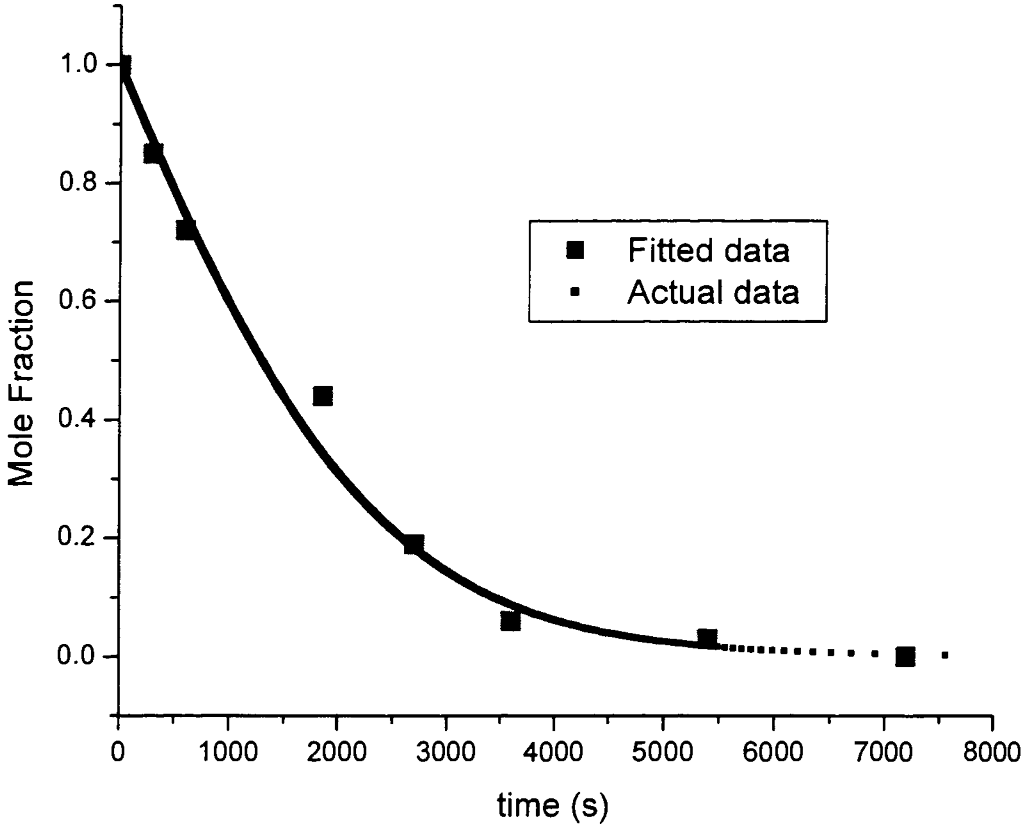

Figure 3.6 A plot of mole fraction against photolysis time for Al(EtOacac)3 2 in which the numerical integration with a quantum yield of 0.013 was fitted against experimental data.

Table 3.3 Quantum yield results for aluminum complexes.

Complex	**Φ**
$Al(EtOacac)_3$	**0.013 ± 0.07**
$Al(EtOacac)_2OBu$	**0.015 ± 0.08**
$Al(EtOacac)(OBu)_2$	**0.027 ± 0.14**

3.2.4 Characterization of the products for the photoreactions of the Aluminum β-diketonate

3.2.4.1 Elemental composition of the photolyzed products

Following the photolysis the sample of $Al(EtOacac)(OBu)_2$ was examined by Auger electron spectroscopy. Analysis of the surface by Auger spectroscopy indicated a film composed entirely of aluminum oxide. Auger electron spectroscopy analyses of the photoproducts of the rest of the aluminum β-diketonate precursors were performed and the results are summarized in Table 3.4. It was observed that except for $Al(EtOacac)(OBu)_2$, carbon impurities were detected on the surface of the photoproducts.

The extent of carbon contamination was 17 % with respect to $Al(EtOacac)_3$ and 18% with respect to $Al(EtOacac)_2(OBu)$. Sputtering of the surface revealed carbon free interiors with aluminum to oxygen ratio consistent with Al_2O_3 for both $Al(EtOacac)_2(OBu)$ and $Al(EtOacac)(OBu)_2$. For $Al(EtOacac)_3$, sputtering of the surface for 20 seconds revealed an aluminum to oxygen ratio indicative of Al_2O_3 with a slight 4% contamination of carbon.

Table 3.4 Summary of AES results for the photoreactions of the aluminum β-diketonate precursors.

Precursor	Sputter Time (seconds)	% Al	% O	% C
$Al(EtOacac)_3$	0	29 ± 3	54 ± 2	17 ± 3
	20	40 ± 3	56 ± 2	4 ± 2
$Al(EtOacac)_2OBu$	0	23± 3	58 ± 2	18± 3
	35	39 ± 3	61 ± 2	0
$Al(EtOacac)(OBu)_2$	0	38 ± 3	62 ± 2	0
	35	39 ± 3	61 ± 2	0

3.2.4.2 Characterization of the volatile products from the photoreactions of Aluminum β-diketonate precursors

Under a static vacuum, thin films of aluminum β-diketonate precursors were photolyzed to completion. Mass spectrometric analyses of the volatile products from the photoreactions were performed and the interpretations of the data are summarized in table 3.5.[57, 58] For volatile products from the photoreaction of $Al(EtOacac)_3$, MS peaks at 130, 87, 85, 69, 43, 31 and 27 were assigned to the parent ligand, $CH_3C(O)CH_2C(O)OCH_2CH_3$. A MS peak with m/e at 84 was assigned to $CH_3C(O)CHCO$ while a peak at 44 was assigned to CH_2OCH_2. The latter two products were believed to be the result of fragmentation of the ligands during photolysis.

For both the photoreactions of $Al(EtOacac)_2OBu$ and $Al(EtOacac)(OBu)_2$, MS peaks at 130, 102, 87, 85, 69, 43, 31, and 27 were associated with $CH_3C(O)CH_2C(O)OCH_2CH_3$. Peaks at 72, 57, 43, 29 and 27 were assigned to $CH_3C(O)CH_2CH_3$ while peaks at 59, 45, 39, 31,27 were assigned to $CH_3C(O)CH_2CH_3$. MS peak with m/e at 84 was assigned to $CH_3C(O)CHCO$ while peak at 44 was assigned to CH_2OCH_2. MS results are summarized in Table 3.5

Table 3.5 Mass Spectrometry data for the photoreactions of the aluminum β-diketonate precursors.

precursor	m/e	assignment
Al(EtOacac)$_3$	130, 87, 85, 69, 43, 31, 27	$CH_3C(O)CH_2C(O)OCH_2CH_3$
	84	$CH_3C(O)CHCO$
	44	CH_2OCH_2
Al(EtOacac)$_2$OBu	130, 102, 87, 85, 69, 43, 31, 27	$CH_3C(O)CH_2C(O)OCH_2CH_3$
	72, 57, 43, 29, 27	$CH_3C(O)CH_2CH_3$
	59, 45, 39, 31, 27	$CH_3C(O)CH_2CH_3$
	84	$CH_3C(O)CHCO$
	44	CH_2OCH_2
Al(EtOacac)(OBu)$_2$	130, 102, 87, 85, 69, 43, 31, 27	$CH_3C(O)CH_2C(O)OCH_2CH_3$
	72, 57, 43, 29, 27	$CH_3C(O)CH_2CH_3$
	59, 45, 39, 31, 27	$CH_3COHCH_2CH_3$
	84	$CH_3C(O)CHCO$
	44	CH_2OCH_2

3.2.4.3 X-ray diffraction from the films produced by the photoreactions

Powder X-ray diffractions were performed on the photolyzed films of Al(EtOacac)$_3$, Al(EtOacac)$_2$OBu and Al(EtOacac)(OBu)$_2$. X-ray spectra for all three photolyzed products did not reveal any reflections in the spectra. This result indicated that the resultant films from the photoreactions were amorphous in nature.

3.2.5 Photolithography of aluminum β-diketonate precursors

An amorphous film of Al(EtOacac)(OBu)$_2$ was irradiated with 254 nm light through a lithography mask. The mask was set in contact with the surface, negating the need for optics. The film was exposed for 3 hours through the mask. The resultant latent image was formed and the film developed with a hexane rinse. The resultant image is shown in Figure 3.7. The printed lines are clearly visible and are 2 μm by 50 μm in size. Similar results were found for films constructed from each of the other complexes.

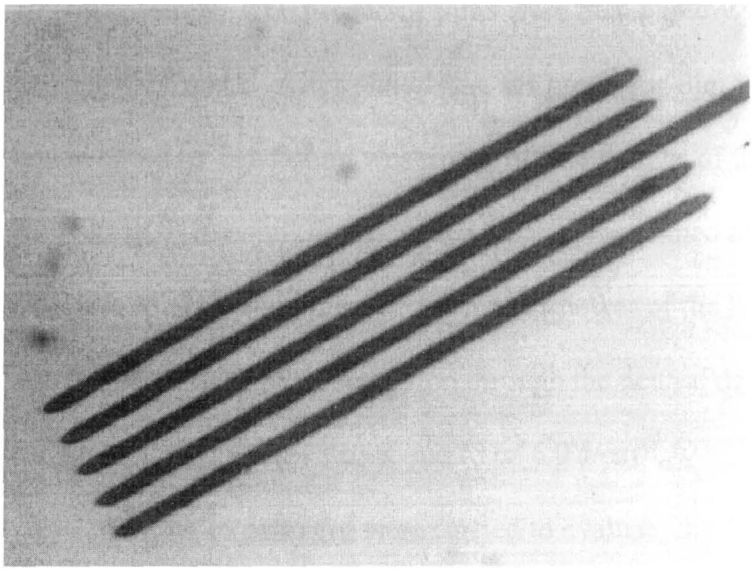

Figure 3.7 Optical micrograph of surface obtained by the photolithography of $Al(EtOacac)(OBu)_2$ on a silicon surface. The 50 micron length of the lines provides an internal scale.

3.2.6 Dose to print for aluminum β-diketonate and aluminum mixed alkoxide β-diketonate precursors

The dose to print is defined by the minimum amount of irradiation energy per unit area required to create an insoluble pattern of a desired material onto a substrate when the deposited material is irradiated. It is an important parameter in the electronics industry. The dose to print of aluminum oxide thin films were determined for the aluminum β-diketonate and aluminum mixed alkoxide β-diketonate precursors. Three aluminum precursors, $Al(EtOacac)_3$, $Al(EtOacac)_2(OBu)$ and $Al(EtOacac)(OBu)_2$ were used to determine the dose to print. For $Al(EtOacac)(OBu)_2$, the precursor solution was prepared by dissolving the precursor into ethyl acetate. The solution was then spin-coated onto a silicon substrate. The precursor films were then photolyzed through a calibrated neutral density filter mask. After photolysis, the precursor film was rinsed in hexane. Material unconverted by irradiation was rinsed off the surface of the substrate. The lowest percentage of transmission in which a pattern remained after photoreaction was recorded. The dose to print was calculated using the power of the light source, time of photolysis and the percentage of transmission through the neutral density filter. The dose to print for $Al(EtOacac)(OBu)_2$ was found to be 6.9 J/cm^{-2}.

Similar experiment were carried to evaluate the dose to print for $Al(EtOacac)_3$, $Al(EtOacac)_2(OBu)$ and all the results are summarized in Table 3.6.

Table 3.6 Dose to print with respect to aluminum β-diketonate and aluminum mixed alkoxide β-diketonate precursors.

Precursor	Dose J/cm^2
$Al(EtOacac)_3$	18.3
$Al(EtOacac)_2(OBu)$	16.5
$Al(EtOacac)(OBu)_2$	6.9

The data suggests the higher the number of β-diketonate ligands attached to the aluminum metal in the precursor, the higher the irradiation dose in order to print the aluminum oxide onto the substrate.

3.3. Discussion

In this chapter, the deposition of aluminum oxide films from films of aluminum precursors by PMOD is presented. A critical requirement for a PMOD precursor lies in its abilities to provide good film forming properties, photochemical sensitivity, and a suitable photoreaction. Aluminum β-diketonates were chosen as PMOD precursors to produce aluminum oxide. β-diketonate is a bidentate ligand that forms coordinate compounds with a variety of metal centers. It has an intense charge transfer transition in the near-UV region. It was also known that metal β-diketonate complexes fragment upon irradiation making them suitable candidates for PMOD precursors.[16]

The effect of inclusion of a single ethoxy group on the β-diketonate ligand, was to lower the overall symmetry of the aluminum precursor, as illustrated in Figure 3.8. This diagram illustrates the molecular form of $Al(acac)_3$ and $Al(EtOacac)_3$ for the purpose of explanation. It is believed that when the precursor is deposited as an amorphous thin film, considerable cross-linking between molecules is present. With the asymmetry introduced by the ethoxy ligand, crystallization of the precursor films can be impeded because the overall symmetry of the precursor molecule is lowered by such introduction. The use of aluminum mixed alkoxide β-diketonate precursor further lowers the symmetry of the precursor.[59] All the above modifications resulted in better film forming properties, leading to better quality precursor films.

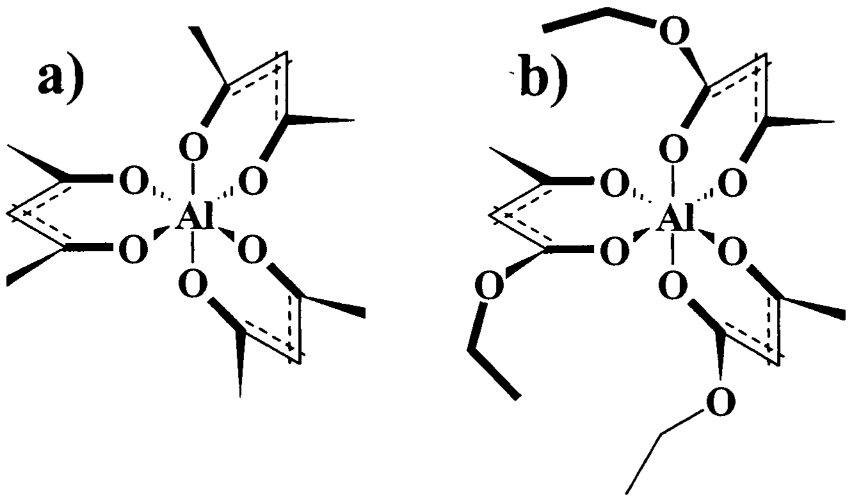

Figure 3.8 Diagrams of a) Al(acac)$_3$ and b) Al(EtOacac)$_3$.

The substitution of alkoxide ligands for β-diketonate ligands was also investigated as a means to improve the purity of the resultant film. By substituting with the smaller alkoxide ligands, the fragments generated from the photoreaction may have a higher chance to leave the surface. This can lead to a less contaminated Al_2O_3 film being produced. It is worth noting that the valence of aluminum does not change with this substitution although the apparent coordination number does change. This apparent change in the coordination number is probably not occurring, but rather association, probably acts to retain a coordination number of five to six.

The mechanism of the photoreactions for the aluminum β-diketonate precursors is best described by considering the reaction of a monomer. A schematic representation of the proposed mechanism for the photoreaction of Al(EtOacac)$_3$ is shown in Figure 3.9.

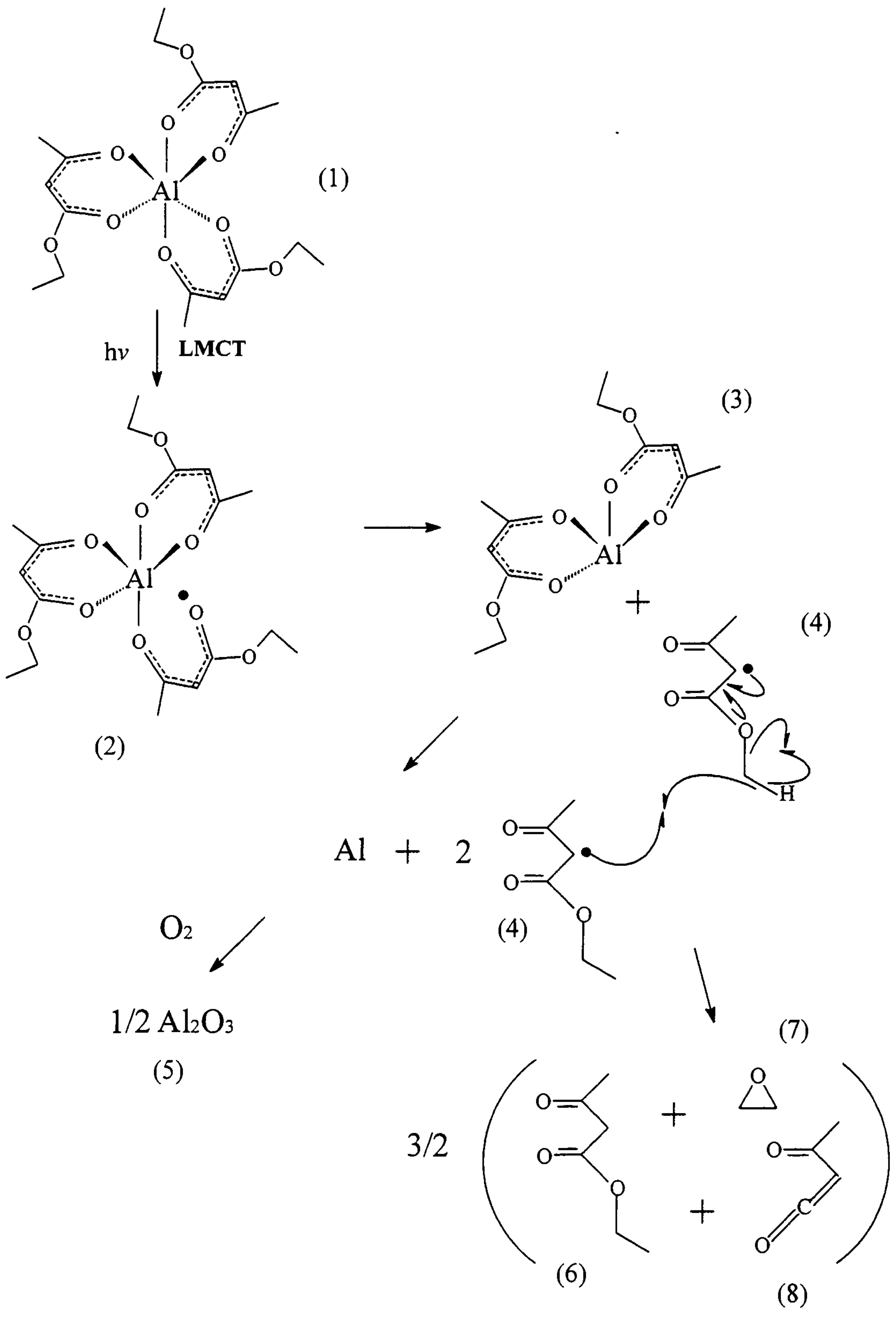

Figure 3.9 Proposed mechanism for the photolysis of Al(EtOacac)$_3$.

Upon irradiation, Al(EtOacac)$_3$ (1) absorbs a photon, the photon will trigger a ligand-to-metal charge transfer (LMCT). This transition results in the cleaving of one aluminum oxygen bond, resulting in a diradical species (2). The complex (2) is unstable due to the formation of an unstable aluminum (II) centre. This in turn leads to the fragmentation of species (2), yielding the intermediate (3) and the β-diketonate radical (4). The resulting species (3) is unstable and will undergo further fragmentation leading to the formation of an aluminum atom, and two more β-diketonate radicals (4). In the presence of oxygen under ambient conditions, aluminum oxide (5) is formed. This single photon mechanism was supported by the IR data as well as the quantum yield calculation. The evidence of aluminum oxide as final product for the photoreaction supported the above mechanism. For the remaining 3 β-diketonate radicals, they will undergo disproportionation, leading to the formation of the parent ligands (6), 3-oxoethylbutanoate, as well as species (7) and (8). All three species were evidenced in the the mass spectrometry data of the volatile fragments formed during the photoreaction of Al(EtOacac)$_3$.

The photoreaction of Al(EtOacac)$_3$ resulted in the formation of amorphous aluminum oxide film on the silicon substrate. Powder X-ray diffraction supported the amorphous nature of the photoproduct.

The proposed mechanism for the photoreaction of aluminum mixed alkoxide diketonate precursors is shown in Figure 3.10. The precursor (9), where x = 1 or 2, undergoes LCMT when a photon is absorbed. This leads to the formation of the diradical (10). Species (10) is unstable and leads to fragmentation of the complex, forming intermediate (11) as well as the β-diketonate radical (4). Species (11) is thermally unstable and further fragmentation leads to the formation of one aluminum atom, x-1 number of β-diketonate radicals, as well as 3-x number of sec-butoxy radical (12). The aluminum atom reacts with oxygen in air, forming aluminum oxide which is evident from the AES results of the photoproduct. The β-diketonate radicals as well as the sec-butoxy radicals will disproportionate, leading to the formation of a variety of products illustrated in the diagram. These species includes the parent ligand (6), 3-oxoethylbutanoate, CH_2OCH_2 (7), $CH_3C(O)CHCO$ (8), 2-butanone (13) and 2-butanol (14).

The presence of species (6), (7), (8), (11) and (12) in the MS data of the photolysis reactions seemed to support the proposed mechanism. This proposed single-photon mechanism also seems to be supported by the observed quantum yield. As in the case of photolysis of $Al(EtOacac)_3$, X-ray diffraction revealed the amorphous nature of the aluminum oxide films resulting from the photolysis of aluminum mixed alkoxide β-diketonate films.

It is also important to point out that the proposed mechanisms were deduced from volatile fragments detected by mass spectrometry when the precursor films were photolyzed in vacuum. When the precursor film is photolyzed under ambient conditions, alternative mechanism such as oxidation of the unstable Al (II) intermediates by oxygen (in stead of thermal decomposition aluminum metal and ligand fragments) is also a possibility.

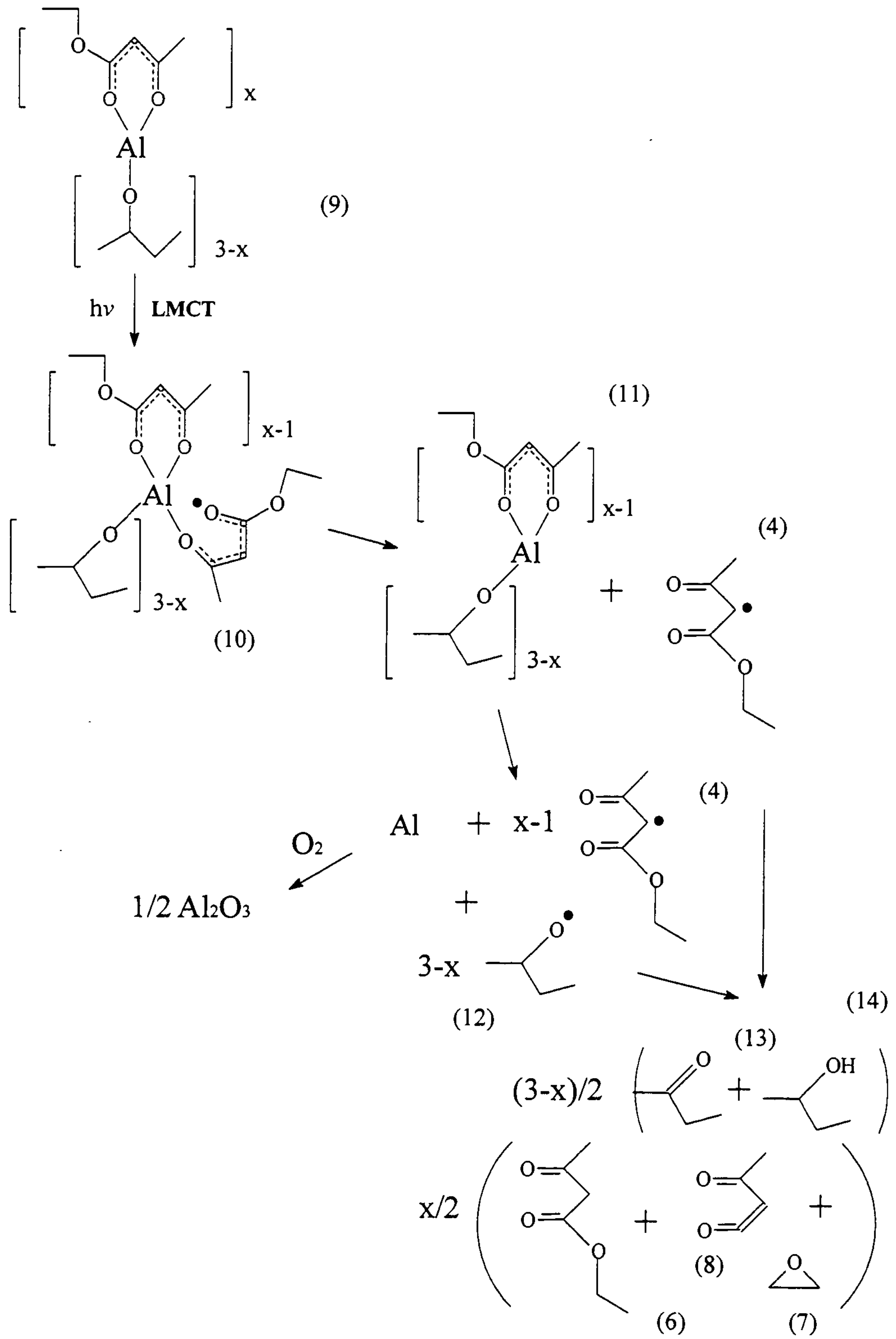

Figure 3.10 Proposed mechanism for aluminum mixed alkoxide diketonate precursor.

The purity of the resultant aluminum oxide photoproduct seems to be related to the number of sec-butoxy ligands present in the precursor complex. From the AES results, decreasing carbon contamination resides in the order of $Al(EtOacac)_3$> $Al(EtOacac)_2OBu$> $Al(EtOacac)(OBu)_2$. The improvement in the purity of the photolyzed films by the replacement of the alkoxy group can be explained by the volatile nature of the sec-butoxy ligands. Depending on the precursor complexes being used, the fragmentation process due to irradiation will result in either all β-diketonate ligands (as in the case of $Al(EtOacac)_3$) or a mixture of β-diketonate, 2-butanone and 2-butanol ligands (as in the case of $Al(EtOacac)_2OBu$ and $Al(EtOacac)(OBu)_2$). The 2-butanone and 2-butanol molecules are more volatile than the β-diketonate ligand, thus increasing their tendencies of leaving the reaction surface to the surroundings. The β-diketonate ligand has a higher tendency to be left on the film surface upon photolysis. The result from the AES analyses of the photolyzed films seems to support the hypothesis. Films from precursors with a higher number of β-diketonate ligands coordinating with the aluminum center have a higher carbon contamination. As a matter of fact, the resultant film from the $Al(EtOacac)(OBu)_2$ was carbon free from the AES result. All this evidence seems to suggest the achievement of improving the purity of the photolyzed films by the substitution of volatile alkoxy group to the precursor molecules.

The quantum yields calculation for the photoreactions indicated the most alkoxide substituted aluminum precursor, i.e. $Al(EtOacac)(OBu)_2$ had the highest quantum yield. This result was also reflected in the dose to print experiment, with $Al(EtOacac)(OBu)_2$ requiring the least amount of irradiation.

3.4. Conclusion

In this chapter, room temperature PMOD process for the deposition of aluminum oxide films is developed using aluminum β-diketonate typed precursor. The photoreactions for aluminum β-diketonate and aluminum mixed alkoxide β-diketonate precursors are consistent with a single photon process. The resultant photolyzed films are amorphous aluminum oxide. The purity of the resultant film improves with the introduction of alkoxide ligands to the aluminum β-diketonate system. Photolithographic patterning of aluminum oxide has also been demonstrated with aluminum β-diketonate and aluminum mixed alkoxide β-diketonate precursors.

3.5. Experimental

3.5.1 Instrument and materials

All silicon wafers were obtained from Wafernet and were n-type Si(100). The wafers were cut to the approximate dimensions of 1 cm x 1.5 cm in house. The NaCl crystals were obtained from Spectra-Tech Inc. The FTIR spectra were obtained with a Bomem MB-120 with 4 cm^{-1} resolution. Electronic absorption spectra were obtained with a HP 8452A diode array spectrometer. The irradiation source for photolysis was conducted with the 254nm output of a low pressure mercury lamp. The intensity of the light source was measured by Gentec detector head PS-310 with a TPM-300 monitor. The mass spectra were obtained from a HP 5958 gas chromatography-MS spectrometer. An electron-impact ion source was used and the ion source temperature was 200 °C. The resolution was 1000 amu^{-1} with electron energy for ionization at 70 eV. Auger spectra were obtained using a PHI double pass CMA at 0.85eV resolution at the Surface Physics Laboratory, Department of Physics, Simon Fraser University. Al(EtOacac)$_2$OBu was obtained commercially from Gelest Inc while Al(EtOacac)(OBu)$_2$ was obtained from Alfa Aesar and Al(EtOacac)$_3$ was prepared by a derivative of a published procedure.[60] AlCl$_3$ was added to toluene solution of ethoxyactylacetyacetone and the mixture was refluxed for 24 hours. The resulting mixture was filtered and the filtrate was evaporated under reduced pressure, yielding white Al(EtOacac)$_3$.

3.5.2 Calibration of the Fourier transform IR and UV-visible absorption on silicon surfaces

Al(EtOacac)(OBu)$_2$ solution (conc. 5.08x10^{-6} mol/ml) was prepared by dissolving the precursor (0.0307g) into ethyl acetate (20ml). A drop of the solution (0.0032ml) was placed on the silicon surface and allowed to dry. An FTIR spectrum of the drop was obtained. The process was repeated 6 more times and a total of seven spectra were overlaid as in Figure 3.11. The absorbance at 1298 cm^{-1} against the concentration was plotted as shown in Figure 3.12. The extinction coefficient for the IR absorption of the precursor at 1298 cm^{-1} was found to be 1.234x10^{6} cm^{2}/mol from the slope of the plot.

The extinction coefficient for the UV-visible absorption of the precursor was derived from the extinction coefficient for the IR absorption. A precursor film was prepared by spin coating the precursor solution onto NaCl substrate. Both FTIR as well as UV-visible spectra were obtained for the film. The extinction coefficient for the wavelength of irradiation (254nm) was obtained relative to the predetermined FTIR bands. Similar procedures were carried out for all the other precursors and the result is summarized in Table 3.2.

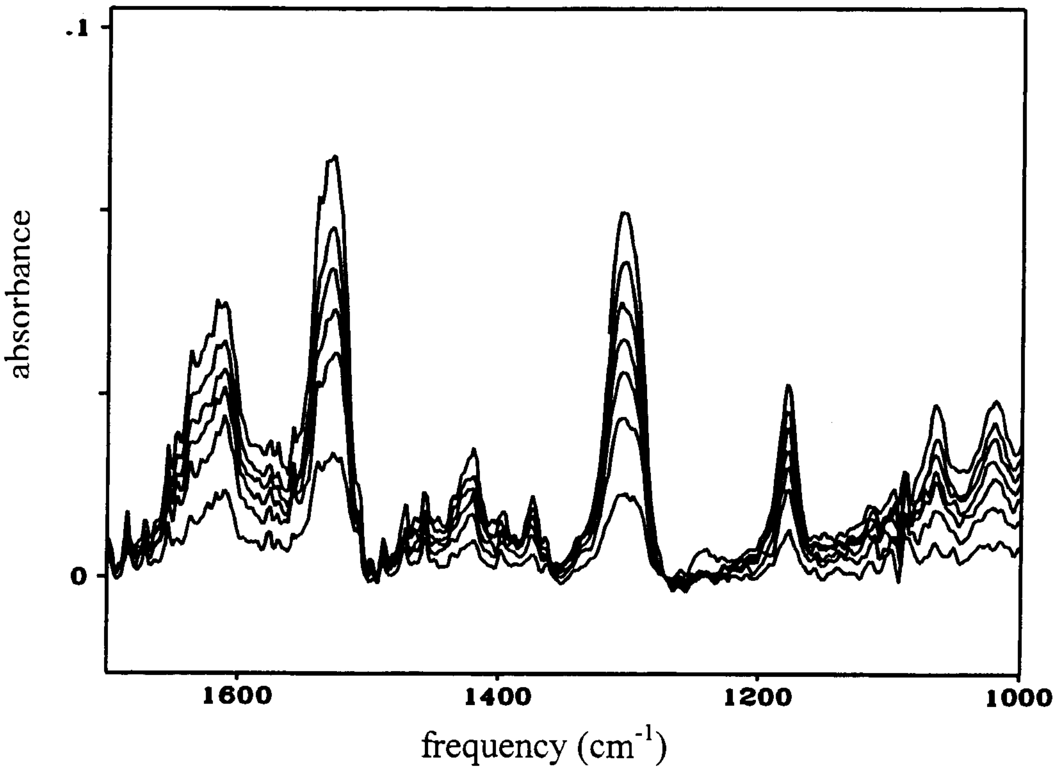

Figure 3.11 Calibration plot Al(EtOacac)(OBu)$_2$ showing the FTIR absorbance against 1, 2, 3, 4, 5, 6 and 7 drops of Al(EtOacac)(OBu)$_2$ with intensities for all FTIR bands increased with more Al(EtOacac)(OBu)$_2$ onto the surface of the substrate.

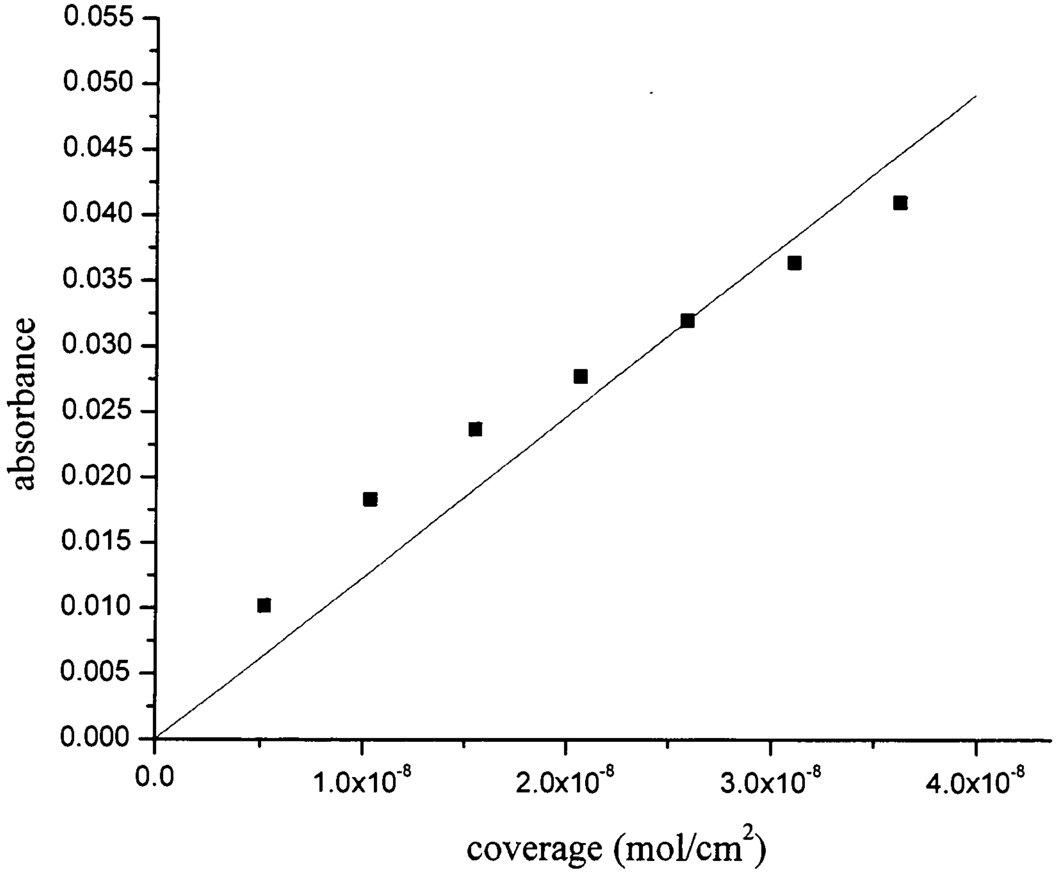

Figure 3.12 Plot of absorbance vs coverage of $Al(EtOacac)(OBu)_2$ at 1298 cm^{-1}.

3.5.3 Photolysis of films of aluminum β-diketonate and mixed alkoxide β-diketonate precursors

Precursor films of $Al(EtOacac)_3$, $Al(EtOacac)_2OBu$ and $Al(EtOacac)OBu_2$ were spin coated onto silicon chips (1x1.5 cm^2) from solutions of ethyl acetate. The FTIR of the samples were obtained and the samples then photolyzed. The FTIR spectra were again obtained and the process repeated until no absorbance associated with the precursors was evident from the FTIR. By monitoring both the light intensity and the extent reaction the apparent quantum yields for the photoreactions were determined. The composition of the photolyzed products were evaluated by Auger electron spectroscopy. Powder X-ray diffraction were also performed on the photolyzed films.

3.5.4 Mass Spectrometric analyses of volatile products from the photoreactions

Films of the aluminum precursors were prepared onto silicon chips in the same fashion as for the photolysis reactions. Each sample was then photolyzed in a sealed, evacuated quartz vessel. Following each photolysis the contents of the head space of the vessel were analyzed. The analysis was conducted by injecting the gaseous contents directly into the chamber of the mass spectrometer. MS data were obtained for all the aluminum precursors and the interpretation of the data is summarized in Table 3.4.

Chapter 4

Properties of Aluminum Oxide and Doped Aluminum Oxide Films Deposited by PMOD

4.1.Introduction

In Chapter 3, a method of depositing amorphous thin films of aluminum oxide using the photochemical metal organic deposition (PMOD) process was introduced. Carbon-free amorphous films of aluminum oxide were produced using aluminum β-diketonate and aluminum mixed alkoxide β-diketonate precursors. A light-induced ligand-to-metal charge transfer from the ligand to the aluminum center was proposed to account for the reaction. This leads to the fragmentation of the ligands, yielding thin films of aluminum oxide.

In this chapter, the properties of the aluminum oxide thin films deposited by PMOD will be presented. Physical properties such as the surface morphology, refractive index and dielectric constant of the aluminum oxide thin film will be discussed.

Aluminum oxide thin films can also be used as the host material for a variety of dopant materials with a number of potential applications. Examples of doped aluminum oxide thin films include rare earth doped (i.e. Tb, Eu or Ce) films of interest for their photoluminescence properties and chromium doped aluminum oxide of interest for laser applications.[61, 62] In this chapter, an example of using the PMOD approach to prepare doped aluminum oxide thin films will also be described.

4.2. Results

4.2.1 Physical properties of aluminum oxide thin films prepared by PMOD

4.2.1.1 Surface morphology of aluminum oxide thin films prepared by PMOD

A precursor film composed of Al(EtOacac)(OBu)$_2$ was prepared by spin coating an ethyl acetate solution of Al(EtOacac)(OBu)$_2$ onto a silicon substrate. The film was photolyzed with 254 nm irradiation to completion, as indicated by no further changes in its FTIR spectrum. The surface morphology of the resultant film was analyzed by atomic force microscopy (AFM). The resultant AFM image is illustrated in Figure 4.1. The surface of the aluminum oxide is smooth in nature with an average roughness of 0.9 Å in the scan area (1 µm x 1 µm). A defect structure was observed in the AFM image. This defect was attributed to the presence of a particle on the aluminum oxide film.

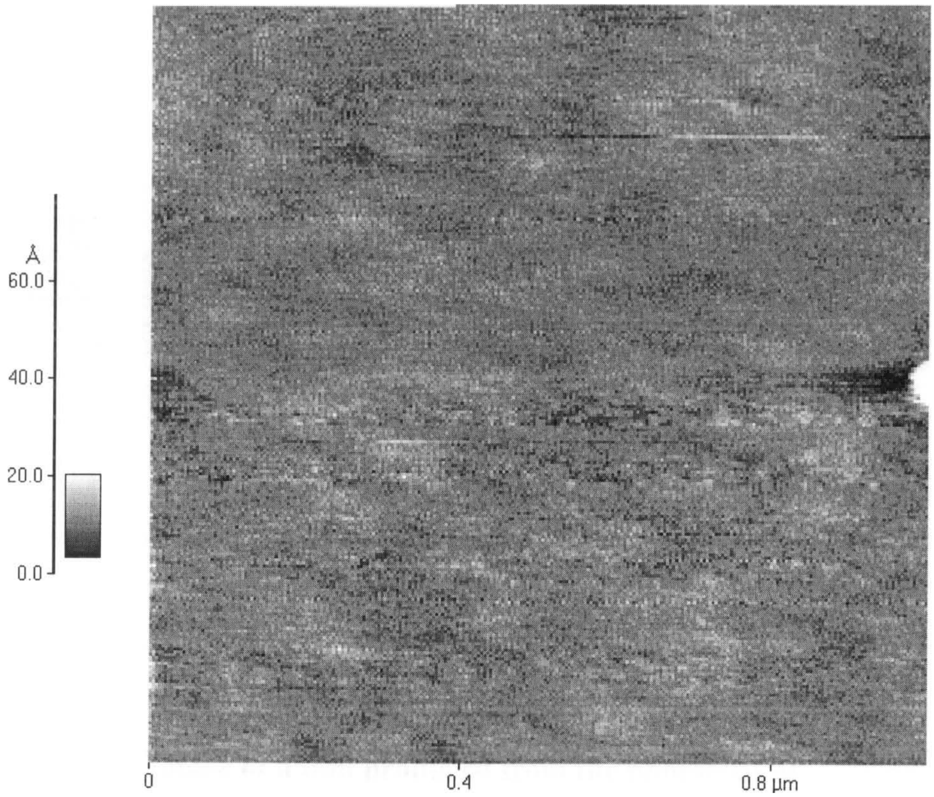

a)

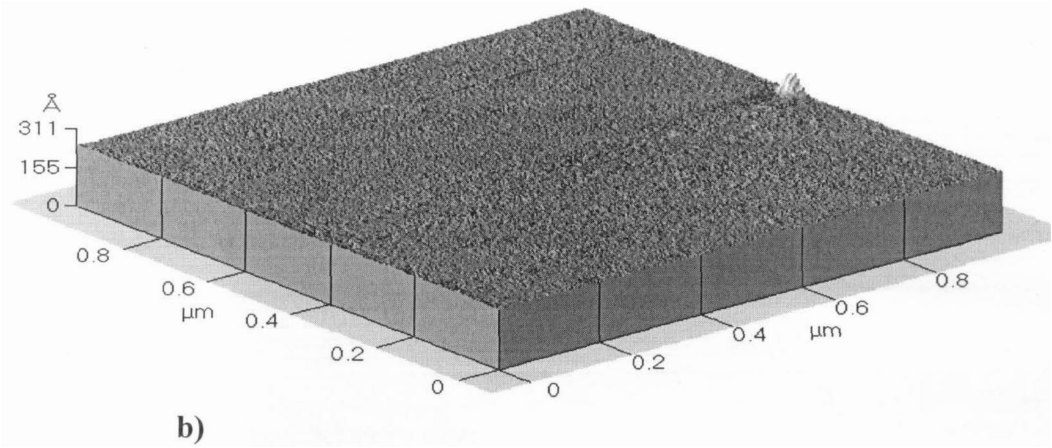

Figure 4.1 AFM image of a film produced from the photolysis of $Al(EtOacac)(OBu)_2$. a) Two-dimensional AFM image of the photolyzed film. b) Three-dimensional AFM image of the photolyzed film.

4.2.1.2 Effect of heat treatment on the aluminum oxide thin films prepared by PMOD

The aluminum oxide film was heated in a furnace in air at 1200 °C for 10 hours with a rate of 5 °C/min and the resultant film was analyzed with both atomic force microscopy and powder x-ray diffraction. The AFM image for the heat-treated aluminum oxide films is shown in Figure 4.2. It was observed that the roughness of the film increased significantly compared to the aluminum film before the heat treatment. The average roughness of the film was determined to be 20.2 Å (compared to 0.9 Å for the pre-heated sample). The AFM image of the heated sample also revealed the appearance of columnar features.

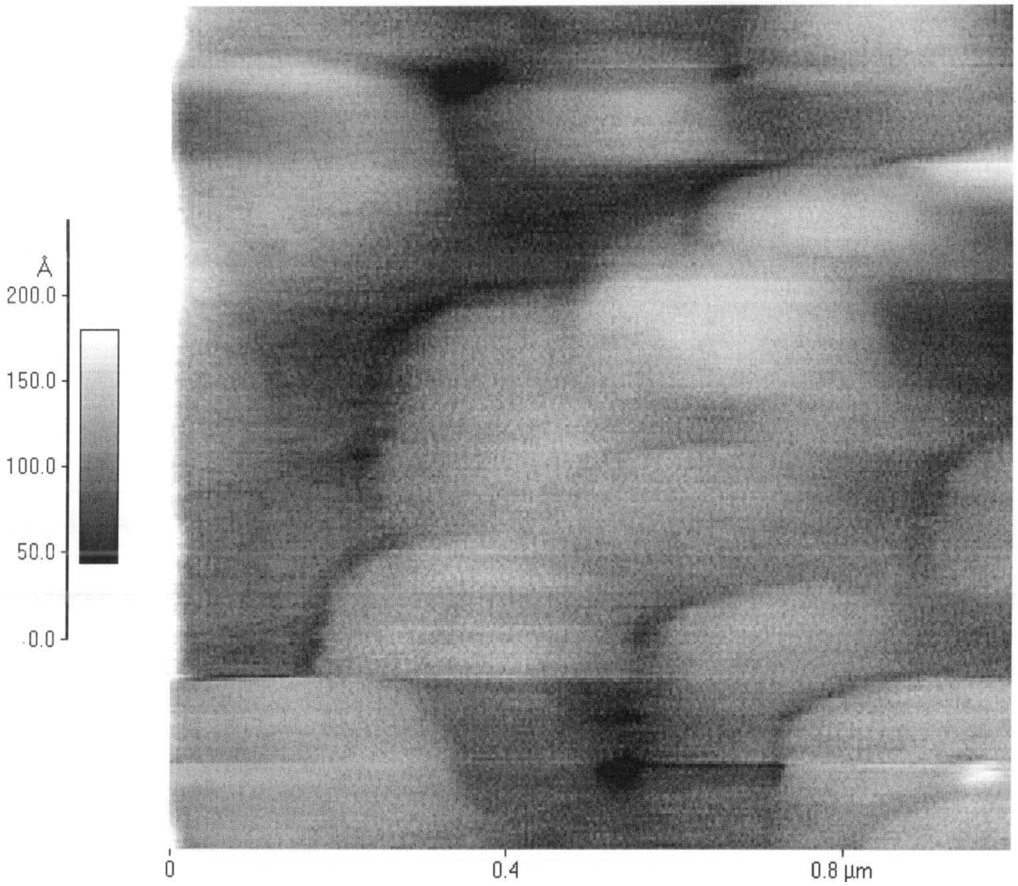

a)

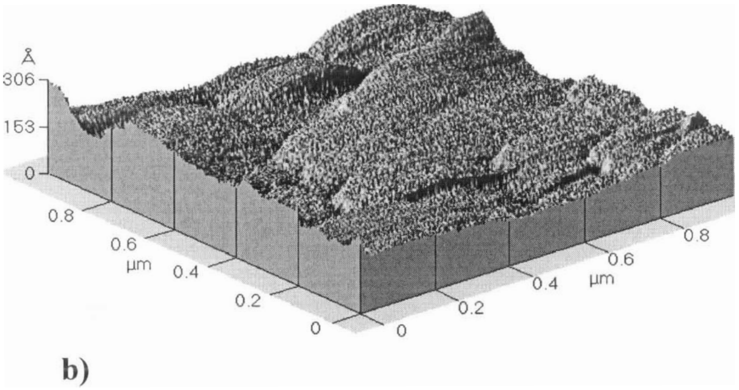

Figure 4.2 AFM image of a film produced from the photolysis of Al(EtOacac)(OBu)$_2$ and heated at 1200 °C for 10 hours in air. a) Two-dimensional AFM image for the annealed aluminum oxide film. b) Three-dimensional AFM image of the annealed aluminum oxide film.

Powder x-ray diffraction was also performed on the heat treated sample. Powder x-ray diffraction was measured on aluminum oxide samples treated at 500 and 800 °C in air. No reflections were observed in the X-ray spectra of the samples. The samples remained amorphous after annealing. When the sample was heated at 1200 °C for 10 hours, reflections were observed in the spectrum which is shown in Figure 4.3 was collected. X-ray reflections indicative of the [104], [113], [202] and [024] planes for α-Al_2O_3 were identified.[63] Reflections due to the substrate were identified by comparing with the X-ray spectrum of the substrate. The relatively weak signals were indications of poor crystallinity of the α-Al_2O_3 thin film. There are also reflections ($2\theta = 35.1$, 42.6 and 44.0) in the x-ray spectrum that were not assigned. These reflections were probably due to other phases of aluminum oxide.

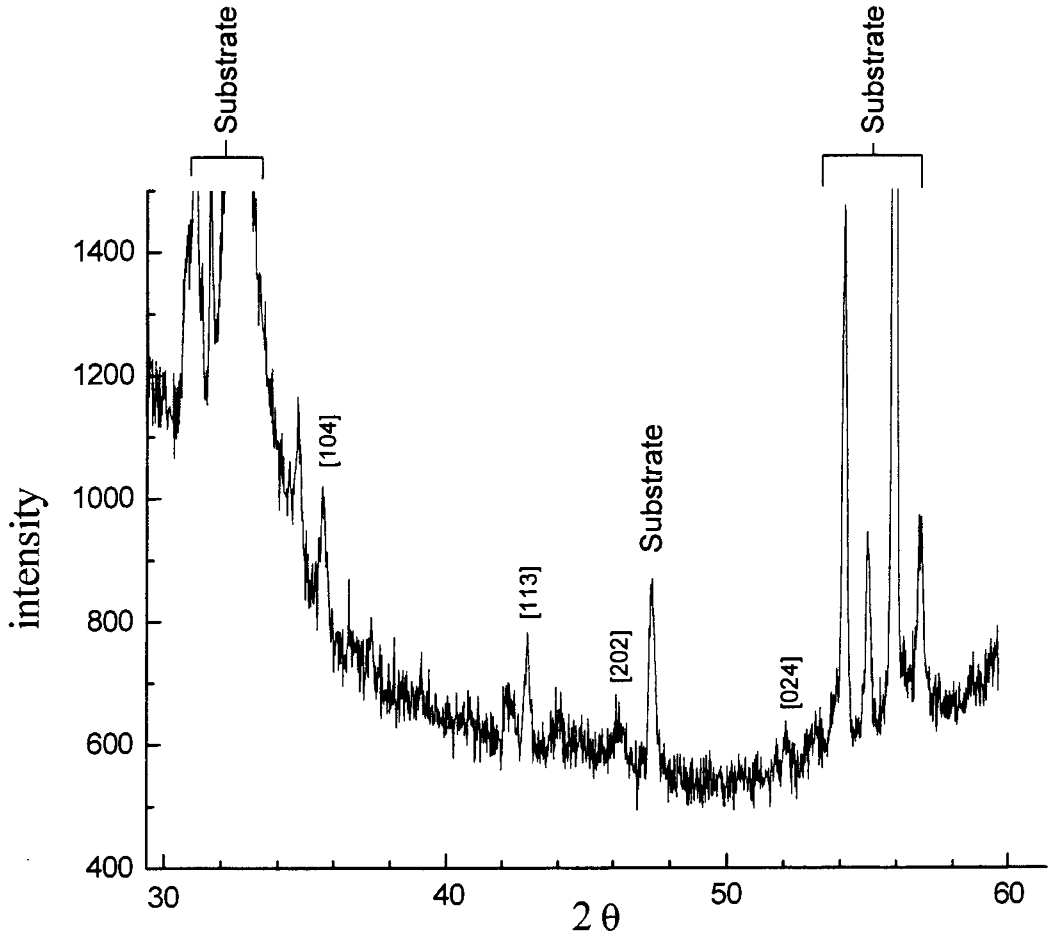

Figure 4.3 Powder x-ray diffraction of aluminum oxide prepared by PMOD and treated at 1200 °C in air.

4.2.1.3 Determination of the dielectric constant of the aluminum oxide film deposited by PMOD

The dielectric constant of the as-deposited aluminum oxide was determined using a metal-insulator-metal (MIM) structure. An illustration of the structure is shown in Figure 4.4. An ethyl acetate solution of $Al(EtOacac)(OBu)_2$ was spin coated onto a platinum substrate. The precursor film was then photolyzed overnight with 254 nm irradiation to ensure the completion of photoreaction. The thickness of the resultant film was determined to be 170 ± 20 nm by a profilometer measurement. Square aluminum features were then sputtered onto the surface of the aluminum oxide film through a shadow mask with square features of 250 μm x 250 μm, resulting in a metal-insulator-metal structure.

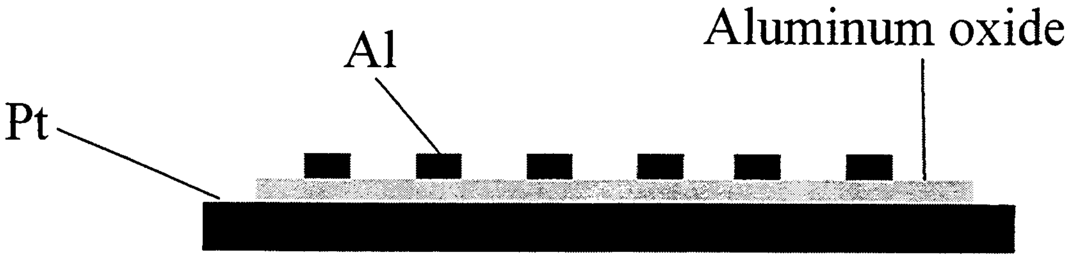

Figure 4.4 Schematic representation of metal-insulator-metal (MIM) structure used to determine the dielectric constant of the aluminum oxide film deposited by PMOD.

An impedance measurement was performed in the laboratory of Professor Zuo-Guang Ye at the Department of Chemistry, Simon Fraser University by Dr. Ming Dong. By interpreting the impedance data of the metal-insulator-metal structure, information about the dielectric constant of the aluminum oxide thin film deposited by PMOD could be obtained. The relationship between dielectric constant of the aluminum oxide deposited by PMOD versus the applied frequency is shown in Figure 4.5. It was observed that throughout the applied frequencies, the dielectric constant of the aluminum oxide film deposited by PMOD ranged from 3.6 to 2.1. The dielectric constant of the aluminum oxide decreased with increasing frequency. It was found that at 10000 Hz, the dielectric constant of the resultant film was 2.8. The measured dielectric constant for aluminum oxide deposited by PMOD is lower than the dielectric constants reported for crystalline aluminum oxide films, which range from 5.0 to 8.0.[64-66]

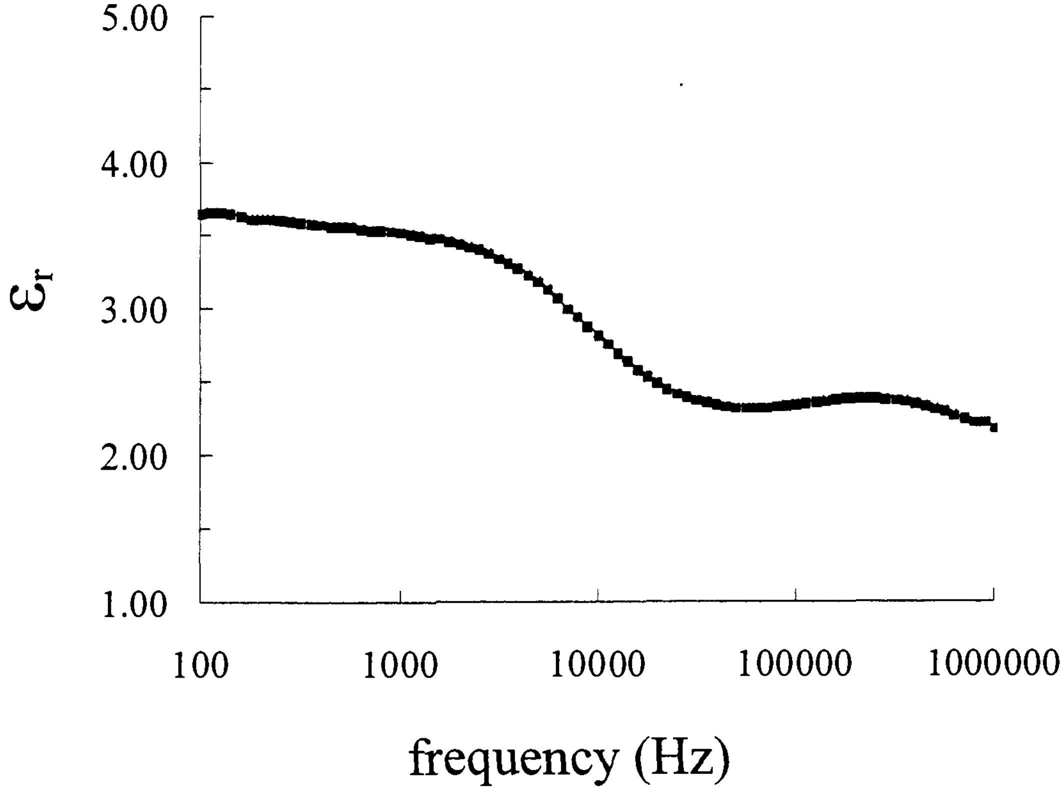

Figure 4.5 Relationship between dielectric constant of the aluminum oxide deposited by PMOD against applied frequency.

4.2.1.4 Refractive index of the aluminum oxide film deposited by PMOD

The refractive index of the aluminum oxide film deposited by PMOD was determined by laser ellipsometry. An aluminum precursor film was deposited by spin coating an ethylacetate solution of $Al(EtOacac)(OBu)_2$ onto a silicon wafer. The film was then photolyzed with a wavelength of 254 nm to completion. The refractive index of the as-deposited film was evaluated using laser ellipsometry. The ellipsometry experiment for the refractive index of the aluminum oxide thin films reported in this thesis was performed at the laboratory of Professor Cliff Henderson at the School of Chemical Engineering, Georgia Institute of Technology by Dr. Sean Barstow. A Cauchy fit was applied to the data and the refractive index can be expressed by the equation (4.1). From the equation, the refractive index at 400 nm is found to be 1.50 ± 0.01.

$$n = 1.499 + 0.005075/\lambda^2 + 2.232\text{x}10^{-5}/\lambda^4 \qquad (4.1)$$

4.2.1.5 Effect of annealing on the refractive index of aluminum oxide films prepared by PMOD

An aluminum oxide film was prepared on silicon substrate in the same fashion as described in the previous section. The film was annealed in a furnace at 500 °C in air for 10 hours. The refractive index of the annealed film was evaluated using laser ellipsometry. A Cauchy fit was applied to the data and the refractive index can be expressed by the equation (4.2). The refractive index at 400 nm is founded to be 1.54 ± 0.01.

$$n = 1.537 + 0.00503/\lambda^2 + 2.10\text{x}10^{-5}/\lambda^4 \qquad (4.2)$$

A third aluminum oxide film was prepared in a similar fashion except that the sample was annealed at 1000 °C for 10 hours upon completion of photolysis. The refractive index of this sample was evaluated using laser ellipsometry. It showed a refractive index in the order of 1.58 ± 0.01 at 400 nm. We were unable to fit the data into a Cauchy polynomial, possibly due to scattering from the annealed sample.

These results indicate an increase in the refractive index of the aluminum oxide film occurs upon annealing at elevated temperatures in air.

4.2.1.6 Photochemistry of precursor films of mixtures of europium and aluminum precursors

Europium doped aluminum oxide thin films were prepared by PMOD from a mixture of europium and aluminum precursors. The europium precursor used was europium (III) 2-ethylhexanoate while the aluminum precursor was $Al(EtOacac)(OBu)_2$. Amorphous Eu_2O_3 films have previously been prepared by the PMOD process with europium (III) 2-ethylhexanoate and was presented in Chapter 2.[49] Upon irradiation under ambient conditions, the europium precursor film decomposes, resulting in the formation of amorphous Eu_2O_3. $Al(EtOacac)(OBu)_2$ was chosen as the PMOD precursor for aluminum oxide. From chapter 3, it was demonstrated that amorphous carbon-free aluminum oxide film can be obtained by the photolysis of precursor film of $Al(EtOacac)(OBu)_2$.

A 0.17 atomic ratio of europium (atomic ratio of europium to aluminum) precursor solution was prepared by mixing measured amounts of europium (III) 2-ethylhexanoate and $Al(EtOacac)(OBu)_2$ in hexane. A thin film was prepared by spin coating the precursor solution onto a silicon substrate. The photolysis with 254 nm irradiation of the mixed precursor system was monitored by FTIR. The FTIR spectra of the film are shown in Figure 4.6.

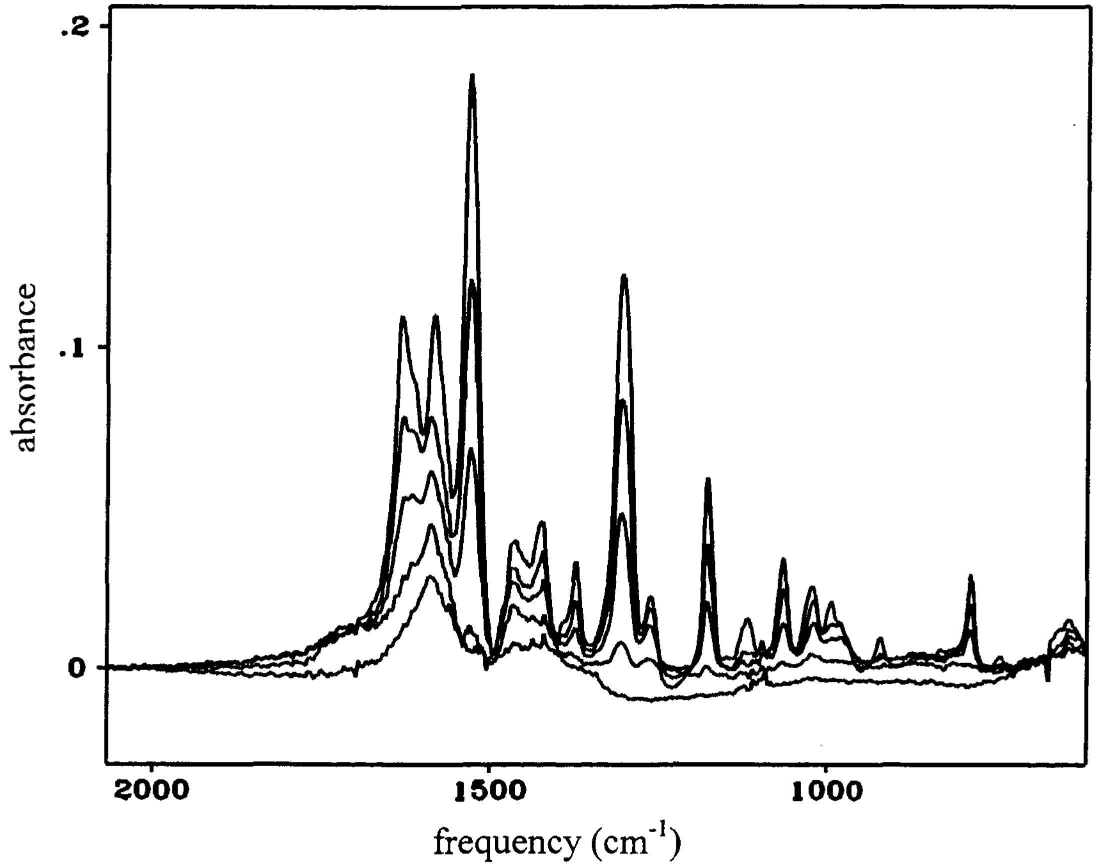

Figure 4.6 FTIR spectra of a film of europium (III) 2-ethylhexanoate and Al(EtOacac)(OBu)$_2$ upon 254 nm irradiation for 0, 35, 96, 240 and 720 minutes. The intensities of all FTIR bands decreased upon photolysis.

The FTIR spectrum of the film can be interpreted as the addition of the spectra of europium (III) 2-ethylhexanoate and Al(EtOacac)(OBu)$_2$. Assignments for the FTIR spectra of europium (III) 2-ethylhexanoate and Al(EtOacac)(OBu)$_2$ can be found in Figure 2.3 and Figure 3.3 respectively. The absorption peaks decayed upon irradiation, indicating the conversion of the precursors to their corresponding oxides. No intermediates were observed during the photoreaction and irradiation continued until no further changes in the FTIR spectrum were observed. The residual absorption observed in the FTIR spectrum was believed to be due to an artifact from spectral subtraction.

Aluminum, europium, carbon and oxygen were found to be present on the surface of the PMOD deposited film by Auger electron spectroscopy. Upon sputtering with argon ions, a carbon free film consisting of aluminum, europium and oxygen was obtained. This result is consistent with the surface contamination of the resultant film. Auger electron spectroscopy was used to determine the atomic ratio of Eu : Al and the result is summarized in Table 4.1.

Table 4.1 Elemental ratio between europium and aluminum in the europium doped aluminum oxide film prepared by PMOD.

Sputtering time (s)	Eu (51 eV) : Al (109 eV)
0	0.24 ± 0.12
60	0.11 ± 0.03
120	0.13 ± 0.06
240	0.11 ± 0.03

Due to the low Auger electron emission probabilities of europium signal in the sample, the error range in the ratio of europium to aluminum is quite significant. The Auger electron spectroscopic data of the ratio between europium and aluminum agrees within experimental error with the atomic ratio in the precursor solution.

4.2.1.7 Photoluminescence of europium-doped aluminum oxide film deposited by PMOD

Another thin film of europium doped aluminum oxide was prepared as above except that the substrate was quartz. A precursor mixture of 0.17 atomic europium : aluminum ratio was prepared. A precursor film was obtained by spin-coating the mixture onto the quartz substrate. The sample was then photolyzed using a 254 nm irradiation source. Upon the completion of the photoreaction, photoluminescence spectrum of the europium-doped aluminum oxide film was obtained using a spectrofluorimeter. The photoluminescence spectrum of the sample was obtained using an excitation wavelength of 340 nm. The resultant spectrum is shown in Figure 4.7.

It was believed that the emission peak at 400 nm was due to the emission from the quartz substrate. An emission spectrum of the blank quartz substrate resulted in the same emission peak at 400 nm. In order to perform a background subtraction to the emission spectrum of europium doped aluminum oxide, an un-doped aluminum oxide was prepared by PMOD on a quartz substrate using $Al(EtOacac)(OBu)_2$ as the precursor. Background subtraction was performed on the europium-doped aluminum oxide spectrum and the resulting spectrum is shown in Figure 4.8.

From the photoluminescence emission spectrum, two emission peaks can be identified. The stronger emission peak at 614 nm was assigned to the $^5D_0$ to $^7F_2$ transition while the emission peak at 590 nm was assigned to the $^5D_0$ to $^7F_1$ transition.[67]

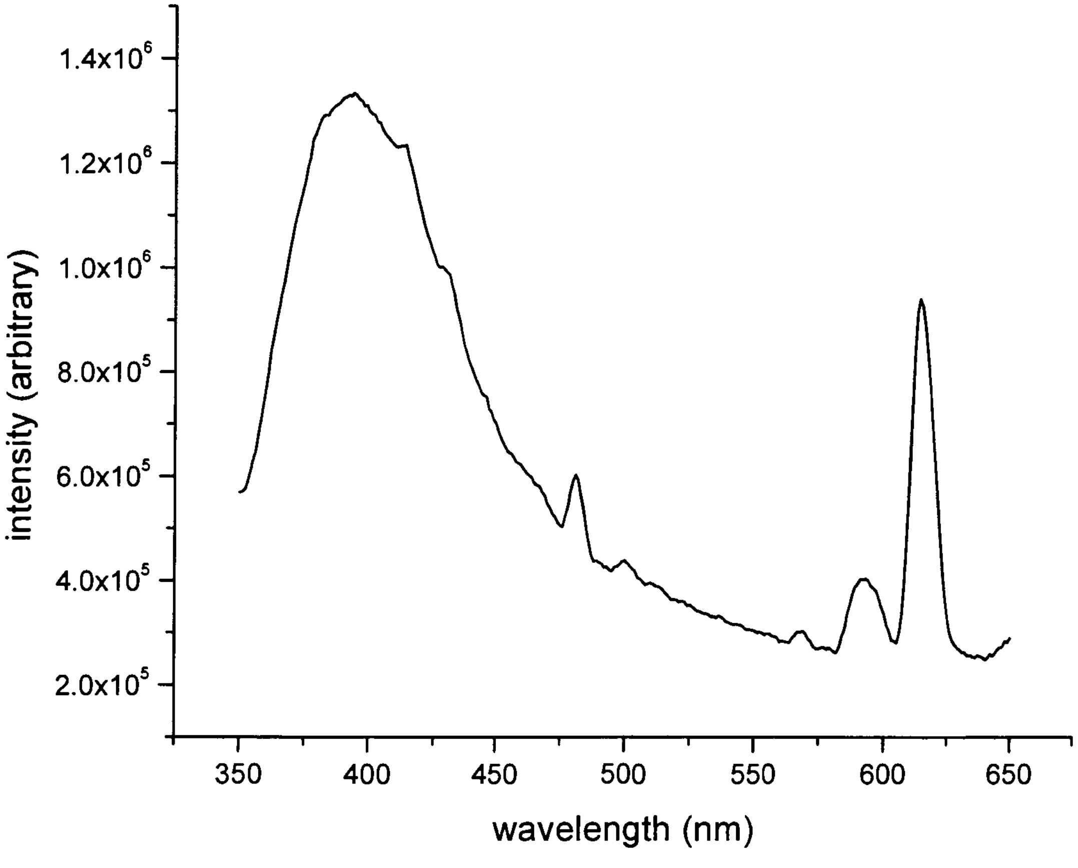

Figure 4.7 Photoluminescence of a europium doped aluminum oxide film (0.17 atomic ratio with excitation wavelength at 340 nm.)

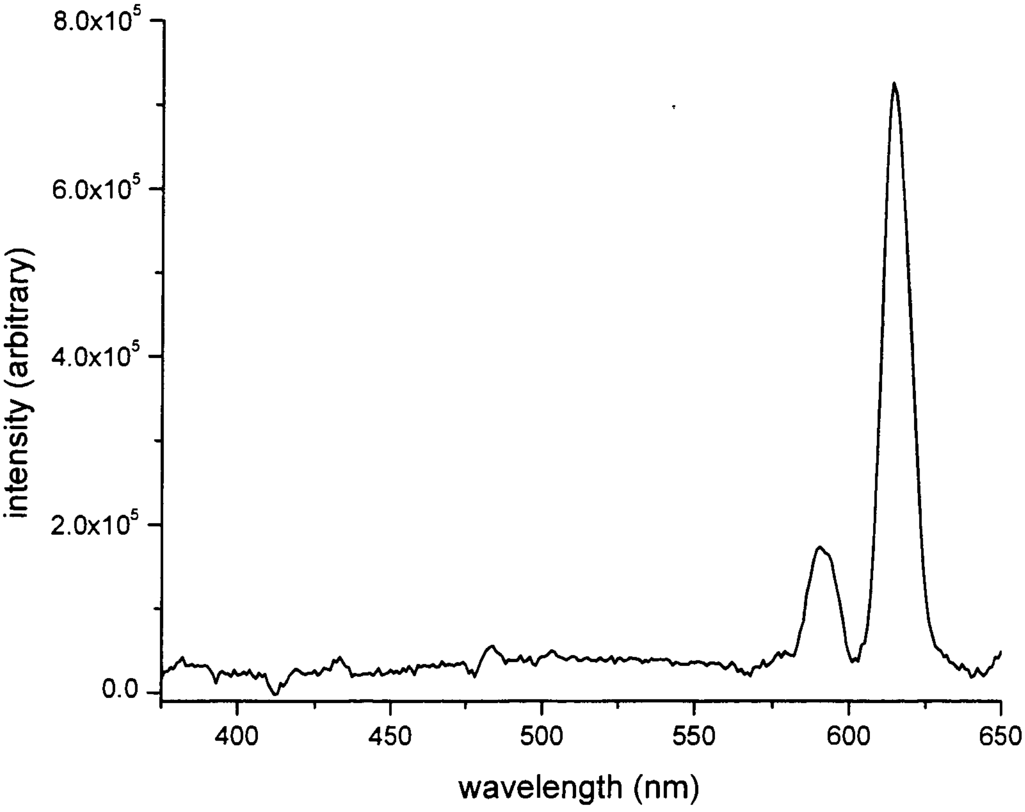

Figure 4.8 Photoluminescence of a europium doped aluminum oxide film after background subtraction.

4.3. Discussion

Amorphous aluminum oxide films were prepared by PMOD using aluminum β-diketonate and aluminum mixed alkoxide β-diketonate precursors. In this chapter some of the properties of the aluminum oxide film deposited by PMOD were presented.

The aluminum oxide has a smooth surface as indicated by atomic force microscopy (AFM). Powder x-ray diffraction revealed the film to be amorphous in nature. Upon heating the amorphous aluminum oxide at the temperature of 1200 °C, crystallization was initiated as indicated by powder x-ray diffraction information. α-Al_2O_3 was obtained upon annealing the amorphous aluminum oxide at 1200 °C. This is consistent with other published results.[68-70] The grain structure became visible in the AFM images upon crystallization. The increase in surface roughness was caused by the phase transition during annealing.[71]

The dielectric constant of the as-deposited aluminum oxide film has a range of 3.6 to 2.1, a lower value range than the previously reported dielectric constant of aluminum oxide thin films. However, the dielectric constant value is in the range of porous alumina formed by chemical etching of aluminum oxide, which has a value of 2.4.[72] The dielectric constant of aluminum oxide appeared to have a direct relationship with the density of the aluminum oxide. The lower the density of the aluminum oxide, as in the case of the porous aluminum oxide deposited by chemical etching, a lower dielectric constant resulted. Since the dielectric constant of aluminum oxide thin film deposited by PMOD is in the same range as with the dielectric constant of porous aluminum oxide, the PMOD deposited aluminum oxide film deposited appeared to have porous structure with density lower than that of bulk Al_2O_3.

The porous nature and the lower density compared with bulk Al_2O_3 can be explained by the nature of the precursor film and its subsequent fragmentation upon irradiation. When the precursor film is deposited onto the substrate, it consists of a three dimensional network of the precursor molecules. Upon irradiation, the ligands undergo fragmentation and escape from the film to the surroundings. This in turn alters the three dimensional arrangement of the film, leading to the formation of a porous, low density aluminum oxide film.

The refractive index of about 1.50 for the deposited aluminum oxide can be compared to the bulk value of 1.771 (at $\lambda = 546$nm).[73] This low refractive number can also be explained by the porous nature of the deposited film. Similar reports of refractive indices as low as 1.2 in porous alumina system have been reported.[8] Annealing of the deposited aluminum oxide film provides energy for the crystallization of the amorphous film. This in turn leads to increase in the density of the aluminum oxide film, resulting in an increase in refractive index as observed by ellipsometry.

Aluminum oxide thin films can also be used as a host matrix to a variety of dopants for a wide range of applications. Photoluminescence emission with europium-doped aluminum oxide at an atomic ratio 0.17 of europium to aluminum has been demonstrated on a sample prepared by PMOD. Studies of europium doped aluminum oxide thin films prepared by sol-gel method indicated the intensity of photoluminescence increased with increasing europium ratio.[67] However at higher dopant concentration (Eu : Al > 0.20) the photoluminescence intensity did not increase with increasing the dopant ratio. This was attributed to the asymmetry to the aluminum oxide structure the europium dopant introduced at higher dopant concentration. Emission at wavelengths of 614 nm and 590 nm are clearly visible from the europium-doped aluminum oxide film deposited by PMOD. The transition corresponds to the $^5D_0$ to $^7F_2$ and $^5D_0$ to $^7F_1$ transitions of Eu^{3+} respectively. The photoluminescence data obtained is consistent with the reported luminescence spectra of europium.[74]

Europium-doped aluminum oxide thin films have previously been prepared by the spray pyrolysis and sol-gel methods.[1, 15] Deposition using PMOD does not require the application of heat to the system. Photolithographic patterning of mixed metal oxides can also be achieved using PMOD. The stoichiometry of the resultant metal oxides is determined by the precursor mixture, which makes the compositional control of the mixed metal oxide system simple.

4.4. Conclusions

In this chapter physical properties such as surface morphology, dielectric constant and refractive index of the aluminum oxide films prepared by PMOD using aluminum β-diketonate and aluminum mixed alkoxide β-diketonate precursors were presented. The PMOD deposited aluminum oxide film is a porous material with a lower density than bulk aluminum oxide. The PMOD deposited aluminum oxide film can be used as a host matrix for dopants such as europium.

4.5. Acknowledgements

Special thanks to Dr. Ming Dong and Professor Zuo-Guang Ye for impedance analysis on the aluminum oxide films and Dr. Sean Barstow and Professor Cliff Henderson at the School of Chemical Engineering, Georgia Institute of Technology for the refractive index measurements of the aluminum oxide films.

4.6. Experimental

4.6.1 Instrument and materials

All silicon wafers were obtained from Wafernet and were n-type Si(100). The wafers were cut to the approximate dimensions of 1 cm x 1.5 cm in house. The NaCl crystals were obtained from Spectra-Tech Inc. The FTIR spectra were obtained with a Bomem MB-120 with 4 cm^{-1} resolution. Electronic absorption spectra were obtained with a HP 8452A diode array spectrometer. The irradiation source for photolysis was conducted with the 254nm output of a low pressure mercury lamp. Auger spectra were obtained using a PHI double pass CMA at 0.85eV resolution at the Surface Physics Laboratory, Department of Physics, Simon Fraser University. The AFM images were obtained using a Park Scientific atomic force microscopy at the Nano-Imaging facility, Department of Physics, Simon Fraser University. The photoluminescence data was obtained using Photon Technology International QuantumMaster fluorimeter (Model QM-1). The impedance experiment was performed at the laboratory of Professor Zuo-Guang Ye at the Department of Chemistry, Simon Fraser University by Dr. Ming Dong. The dielectric constant measurement was performed by Solartron SI 1260 impedance analyzer combined with a Solartron 1296 interface. The ellipsometry experiment for the refractive index of the aluminum oxide thin films reported in this thesis was performed at the laboratory of Professor Cliff Henderson at the School of Chemical Engineering, Georgia Institute of Technology by Dr. Sean Barstow. The film thickness measurement was obtained using an Alpha Step 100 profilometer. The powder X-ray diffraction analysis was performed using a Rigaku D/Max-Rapid curved image plate microdiffraction system

The Al(EtOacac)OBu$_2$ complex used in the experiment was obtained Alfa Aesar and europium 2-ethylhexanoate was purchased from Strem Chemicals. The solvent used in the experiment was ethyl acetate unless otherwise stated.

4.6.2 Determination of the dielectric constant of the photolyzed aluminum oxide film

Al(EtOacac)OBu$_2$ was added to an ethyl acetate solution. Aluminum precursor film was prepared by spin coating the solution onto a platinum coated silicon substrate at about 2000 rpm. The sample was then photolyzed with 254 nm irradiation until completion. Aluminum squares (250 nm thickness) of 250 μm x 250 μm were sputtered onto the amorphous oxide film. The thickness of the aluminum oxide layer was determined by profilometer and was found to be 170 nm. The impedance of the metal-insulator-metal structure was measured as a function of frequency.

4.6.3 Photoreaction of europium doped aluminum precursor film

0.1549g of europium (III) 2-ethylhexanoate was mixed with 0.4748g of Al(EtOacac)(OBu)$_2$ in 4.2 ml of hexane. The resulting mixture was spin-coated onto silicon substrate. The film was then irradiated at 254 nm with FTIR spectra recorded at various time intervals. The overlay spectra for the photolysis of the mixed precursor film were illustrated in Figure 4.6.

Chapter 5

Photochemical Metal Organic Deposition (PMOD) of Tin Oxide

5.1.Introduction

In this chapter, the photochemical metal organic deposition of tin oxide from thin films of tin (II) 2-ethylhexanoate is described. Tin oxides are of interest for a variety of applications. Tin (II) oxide has been suggested as an alternative anode material for lithium intercalation batteries.[75-77] Tin (IV) oxide is also of interest for application as transparent conducting oxide films in sensors and solar cells.[78, 79] Of more immediate importance is the use of precursors to tin oxide to prepare other materials which contain elements in addition of tin and oxygen. Of most importance is indium tin oxide, which is used as a transparent electrode in many applications.[80]

Tin oxide has previously been deposited by a variety of methods including hydrothermal synthesis, reactive ion assisted deposition, spray pyrolysis, sputtering, chemical vapor deposition, thermal evaporation and sol-gel deposition.[75, 81-88] All these deposition methods are high energy techniques and in most cases require expensive equipment for the depositions. Furthermore, the patterning of tin oxide films cannot be achieved directly from these methods.

Previous work has shown that metal carboxylate photochemistry is suitable for conducting PMOD.[49, 51, 89-90] The chosen precursor for PMOD of tin oxide thin films is tin (II) 2-ethylhexanoate. One of the main criteria for a suitable precursor for the PMOD process is the ability to form an amorphous precursor film. Amorphous precursor films exhibit much higher photoefficiency than a crystallized film during the photolysis process. Amorphous precursor films are readily formed using metal 2-ethylhexanoates. This is because metal 2-ethylhexanoate complexes have large organic ligands containing an unresolved chiral carbon (at the β position). This lowers the overall symmetry of the complex, resulting in a higher kinetic barrier to crystallization. Besides the ability to form an amorphous precursor film, thin films of metal 2-ethylhexanotes are also known to undergo decarboxylation upon photolysis, leading to the formation of metal oxide.[49, 51, 90] In this study, the mechanism of the photoreaction within the thin film will be explored. The effect of heating upon the resultant thin oxide film will also be discussed.

5.2. Results

5.2.1 Characterization of tin (II) 2-ethylhexanoate thin films

A thin film of tin (II) 2-ethylhexanoate was produced by dissolving the precursor in a volatile solvent and spin coating the solution onto a silicon substrate. Several solvents, including dichloromethane, hexane, butanone, ethylacetate and n-butylacetate were used to produce precursor films of tin (II) 2-ethylhexanoate and it was found that hexane and n-butylacetate gave best quality precursor films.

A solution of tin (II) 2-ethylhexanoate in hexane was spin coated onto a silicon substrate, producing an amorphous thin film of tin (II) 2-ethylhexanoate. The FTIR spectrum of the film was recorded and is presented in Figure 5.1. The four absorptions between 3000 and 2800 cm^{-1} are associated with CH stretching modes of the organic ligand. The absorption band at 1709 cm^{-1} is associated with uncoordinated 2-

ethylhexanoaic acid in the sample. The absorption peaks in the region between 1320 to 1200 cm^{-1} are assigned as hydrocarbon chain vibrations. The peaks at 1610 and 1562 cm^{-1} are assigned as to the antisymmetric CO stretching vibrations. The peaks, observed at 1462 and 1418 cm^{-1} are associated with the symmetric CO stretching vibration. The observation of two symmetric CO stretching vibrations have been reported previously in the related manganese compound.[91, 92] The assignments were made by comparison with other metal carboxylate molecules.[39, 93]

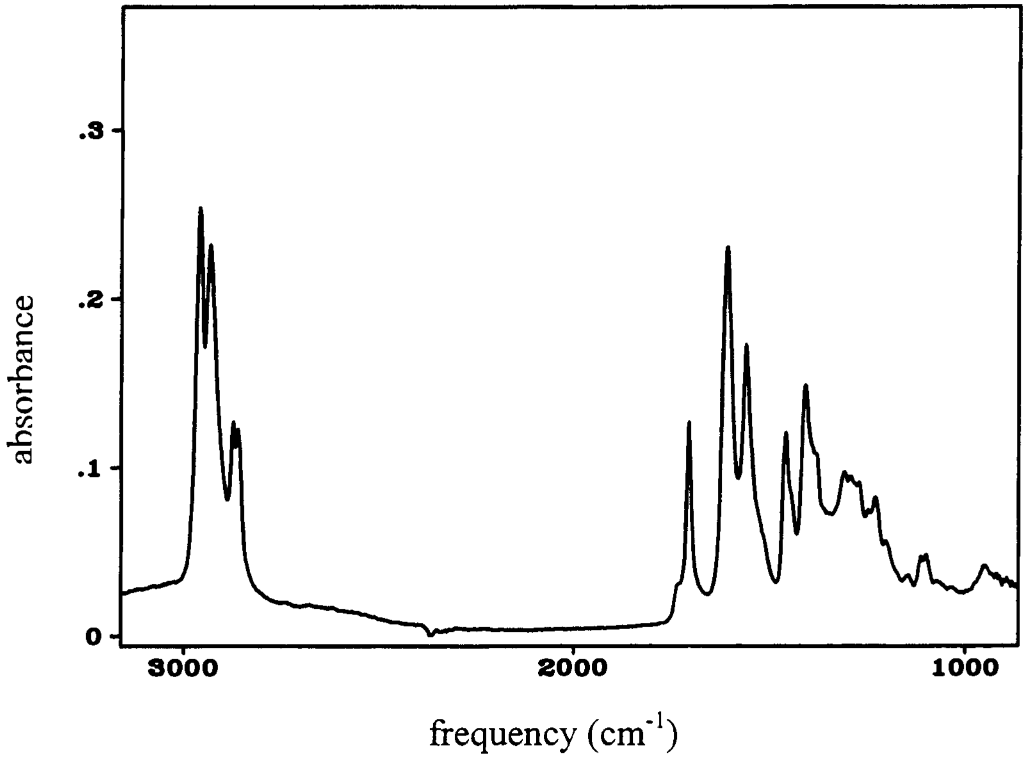

Figure 5.1 FTIR absorption spectrum of tin (II) 2-ethylhexanoate cast from hexane on CaF$_2$ substrate.

An indication of the bonding mode of carboxylate ligands may be found from the difference in energy between the symmetric and antisymmetric absorption bands.[94] Values of 40 to 80 cm^{-1} for the frequency difference $\Delta\nu = \nu_{as}(COO)-\nu_{s}(COO)$, are consistent with bidentate bonding modes for the acetate complexes. For bridging acetates the frequency difference $\Delta\nu$ ranges from 130 to 189 cm^{-1}. Unidentate complexes exhibit much greater $\Delta\nu$ values, between 220-380 cm^{-1}. The frequency differences for the tin (II) 2-ethylhexanoate are 192 cm^{-1}, and 100 cm^{-1}. This we interpret as indicating that the band at 1610 is associated with a bridging 2-ethylhexanoate ligand while the band at 1562 is associated with a bidentate coordination mode.

Similar infrared spectra of tin (II) carboxylates have been suggested to be associated with polymeric structures.[94] The spectra of the thin films support this postulate. The crystal structure of tin (II) acetate also suggest that the coordination is primarily of the bridging form.[39]

Based on similarity of the linkage group of tin acetates and 2-ethylhexanoates, an approximate structure for tin (II) 2-ethylhexanoate is proposed in Figure 5.2. Note that this structure will provide a model with which we can examine the photochemistry. The presence of coordinated acid is not included within this model but will be referred to independently.

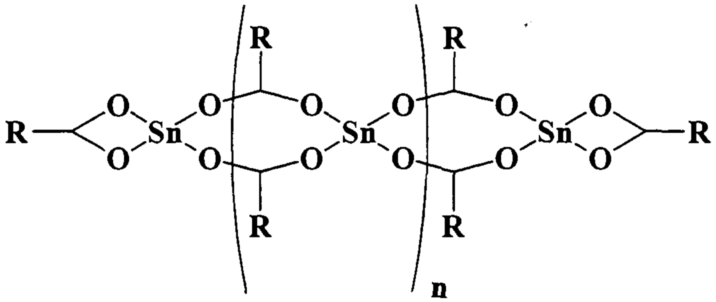

Figure 5.2 Representation of the general structure of tin (II) 2-ethylhexanoate as a thin film.

The FTIR spectroscopic data for region corresponding to the carboxylate regions as well as their corresponding extinction coefficients is shown in Table 5.1.

Table 5.1 FTIR Spectroscopic data with respect to the carboxylate absorptions for $Sn(O_2CCH(C_2H_5)C_4H_9)_2$ spin coated from hexane.

Absorption Maxima	Extinction coefficient x 10^5 cm^2/mol	Assignment
1709 cm^{-1}	0.56	2-ethylhexanoic acid
1610 cm^{-1}	1.22	ν_{as} (CO_2) 2-ethylhexanoate
1562 cm^{-1}	0.76	ν_{as} (CO_2) 2-ethylhexanoate
1462 cm^{-1}	0.51	ν_s (CO_2) 2-ethylhexanoate
1418 cm^{-1}	0.64	ν_s (CO_2) 2-ethylhexanoate
200 nm	11.52	LMCT
220 nm	13.22	LMCT
254 nm*	3.28	

* Absorbance at the irradiation wavelength

Thin films of tin (II) 2-ethylhexanoate were also characterized by UV-Vis spectroscopy. The electronic absorption spectrum for an amorphous film of tin (II) 2-ethylhexanoate was characterized by absorption bands in the region of 202 nm and 220 nm. These peaks are assigned as the charge transfer transitions. The molar extinction coefficients for these bands were determined by comparison with the extinction coefficient measured for the IR transitions. The molar extinction coefficient of each peak together with the extinction coefficient at 254 nm is also shown in Table 5.1.

5.2.2 Photochemical reaction of tin (II) 2-ethylhexanoate thin films

A film of tin (II) 2-ethylhexanoate was cast from hexane and its FTIR spectrum was recorded. The sample was then photolyzed for 5 seconds under a 254 nm irradiation and its FTIR spectrum was acquired again. The process was repeated until the FTIR spectrum of the precursor film did not change upon subsequent photolysis. There are no changes in the FTIR spectrum for photolysis times exceeding 30000 seconds. The spectra are displayed in Figure 5.3.

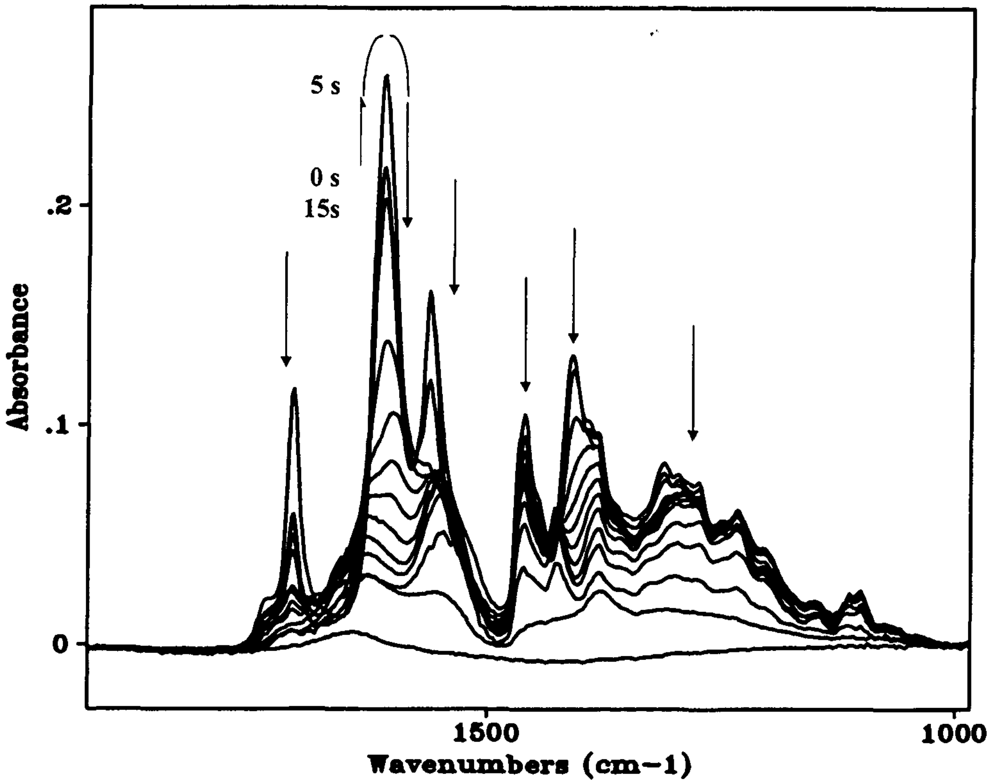

Figure 5.3 Overlay FTIR spectra of the photolysis of tin (II) 2-ethylhexanoate cast from hexane on CaF substrate at 0, 5, 15, 30, 60, 120, 240, 600, 1800, 3600, 7200, 14400 and 30000 seconds under 254 nm irradiation. During the photolysis, the intensities of all FTIR bands decreased upon photolysis except for the FTIR absorptions at 1610 and 1562 cm^{-1} in which the intensities were strongest at 5 seconds, followed by 0, 15, 30, 60, 120, 240, 600, 1800, 3600, 7200, 14400, and 30000 seconds.

During the first 5 seconds of the photolysis, the intensities of the IR peaks at 1610 cm^{-1} and 1562 cm^{-1} increased by 20% and 2% respectively and reached their maximum intensities. The IR absorbance corresponding to the free 2-ethylhexanoic acid at 1709 cm^{-1} decreased to about 50% of its original intensity during the first 5 seconds of irradiation. Subsequent irradiation led to the decay of intensities of all IR absorptions for the precursor film. During the process of photolysis, loss of IR absorption bands at 1610 and 1562 cm^{-1} was observed while IR bands at 1630 and 1550 cm^{-1} appeared. Photolysis of the precursor sample was continued until no further changes were observed in the FTIR spectrum after the film was photolyzed for 500 minutes.

An attempt to evaluate the quantum yield for the photolysis of tin (II) 2-ethylhaxanoate was performed by monitoring the IR absorption peaks against the photolysis time. However it was discovered that during the photoreaction, the rate of decay of a particular IR absorption band is different than the rate of a different IR absorption band. In order to illustrate the different rates of decay among different IR absorption bands, a plot of $(A_t - A_\infty)/(A_0 - A_\infty)$ for IR peaks in the carboxylic region at 1610 and 1562 cm^{-1} is shown in Fig. 5.4. As a result, no fit theory could be applied to evaluate the quantum yield of the photoreaction.

From the plot, it is shown that the peak at 1610 cm^{-1} has a higher initial rate of decay during the photolysis process than the peak at 1562 cm^{-1}. The difference in the rates with respect to the IR absorption peaks is due to the nature of the IR absorption peaks. Due to the polymeric nature of the carboxylic bonding within the precursor film, the observed IR peaks in the region are likely the result of a mixed mode of absorptions for the different bond types within the precursor film. So the observed decays from the IR absorptions are likely due to a number of different carboxylic vibrations. As a result a quantitative study for the quantum yield of the photolysis of tin (II) 2-ethylhexanoate from FTIR data was not successful.

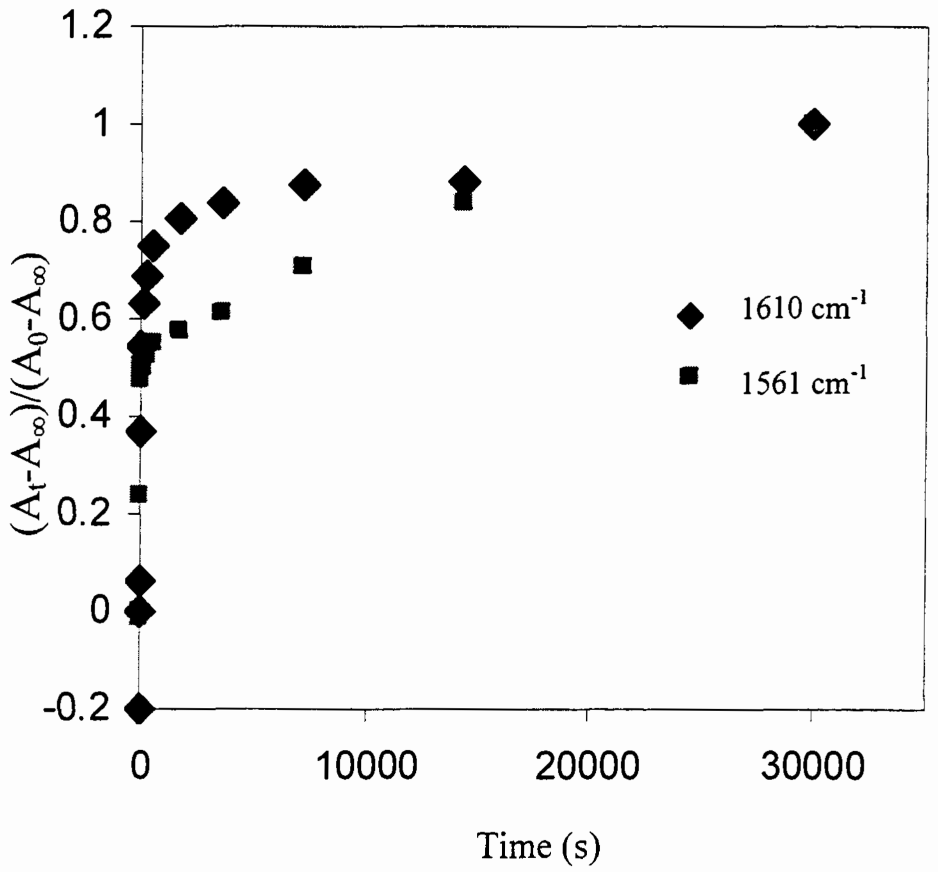

Figure 5.4 Plot of $(A_t - A_\infty)/(A_0 - A_\infty)$ for IR peaks at 1610 and 1562 cm^{-1} against time (in second) as an indication of the rate of decay for each IR peak during photolysis.

5.2.3 Dose to print for tin (II) 2-ethylhaxanote precursor

An alternative method to obtain quantitative information of the photoreaction can be achieved by evaluating the dose to print for the tin (II) 2-ethylhexanoate precursor. The dose to print for tin oxide was determined for the tin (II) 2-ethylhexanoate precursor. The precursor solutions were prepared by dissolving the precursor into hexane. The solution was then spin-coated onto a silicon substrate. The precursor film was then photolyzed through a calibrated neutral density filter mask. After photolysis, the precursor films were then rinsed in hexane. Materials unconverted by irradiation were rinsed off the surface of the substrate. The lowest percentage of transmission in which a pattern remained after photoreaction was recorded. The dosage was calculated using the power of the light source, time of photolysis and the percentage of transmission through the neutral density filter. The dose to print tin oxide from tin (II) 2-ethylhexanoate was found to be 2.8 J/cm^2.

5.2.4 Characterization of the product for the photoreaction of tin (II) 2-ethylhexanoate

The film resultant from the photolysis of tin (II) 2-ethylhexanoate cast from hexane was examined by Auger electron spectroscopy. The result is summarized in Table 5.2. Auger electrons indicative of the presence of tin, carbon and oxygen were all observed from the surface of the film. The composition of the interior revealed by sputtering of the film surface for 12 seconds revealed a carbon-free tin oxide with an elemental ratio of tin : oxygen of 1:1. A further 12 seconds of sputtering revealed a similar elemental composition. The film resultant from the photolysis of tin (II) 2-ethylhexanoate had an elemental composition within the error of that of tin (II) oxide SnO.

Table 5.2 Auger electron spectroscopic data of the film produced by photolysis of tin (II) 2-ethylhexanoate with 254 nm light

Sputter time (seconds)	%Sn	%O	%C
0	46 ± 3	40 ± 3	14 ± 6
12	51 ± 4	49 ± 5	0
24	51 ± 4	49 ± 2	0

5.2.5 Determination of the volatile products of the photoreaction of thin films of the 2-ethylhexanoate precursor

An amorphous film of tin (II) 2-ethylhexanoate was prepared as above and photolysed under a static vacuum. The volatile products were then introduced into the ionization chamber of a mass spectrometer and analyzed.[96]

The highest mass peaks observed were at m/e 100 and 98 and were presumably associated with the parent ions of heptane and heptene. Consistent with this interpretation the remaining spectrum had the distinctive features of the long chain saturated hydrocarbons.[23] The spectrum had peaks corresponding to the fragmentation of the molecular ion at m/e of 43, 57 and 71. The distribution of the relative intensities of these ions was characteristic of saturated hydrocarbon chains, having the most intense peak at m/e of 57 (C_4 fragment). The peaks at m/e=43 and 71 (C_3 and C_5 fragments) were also intense. The signal associated with ions of larger and smaller fragments are smaller than those of the C_3, C_4 and C_5 fragments.

There was also an intense peak observed at m/e of 44. This signal we associate with the formation of carbon dioxide. This result is consistent with the fragmentation of the 2-ethylhexanoate ligand to form carbon dioxide and the hydrocarbon radical C_7H_{15}. Presumably two of the photoproduced radicals exchange a hydrogen atom to yield the observed hydrocarbon fragments C_7H_{16} and C_7H_{14}. This, in combination with the information, from the Auger spectrum, that the resultant film is tin oxide suggests the reaction is best described by equation 5.1. The photoreaction produces one equivalent of tin oxide, two equivalents of carbon dioxide and one equivalent each of heptane and heptene.

From the FTIR we also proposed that there was some coordinated 2-ethylhexanoic acid within the film. The coordinated 2-ethylhexanoic acid presumably decomposes to yield the observed carbon dioxide and heptane.

$$Sn(O_2CCH(C_2H_5)(CH_2)_3CH_3)_2 + 1/2\ O_2 \rightarrow SnO + 2\ CO_2 + C_7H_{16} + CH_3(CH)_2C_4H_9 \qquad 5.1$$

5.2.6 X-ray diffraction of the photolyzed film of tin (II) 2-ethylhexanoate

X-ray diffraction was used to determine the crystallinity of the photoproduct. The X-ray spectrum for the tin oxide surface produced at room temperature showed no diffraction peaks. This indicated the film was amorphous in nature. The sample was then heated at 800 °C in air for 1 hour and another X-ray diffraction spectrum was obtained. The spectrum of the heated film is shown in Figure 5.5. Peaks observed were assigned to the (111), (220), (311), (400) and (511) reflections of tin (IV) oxide (SnO_2 Cassiterite) by comparison with the published data.[97] The result indicates oxidation of SnO to SnO_2 by air during the annealing process.

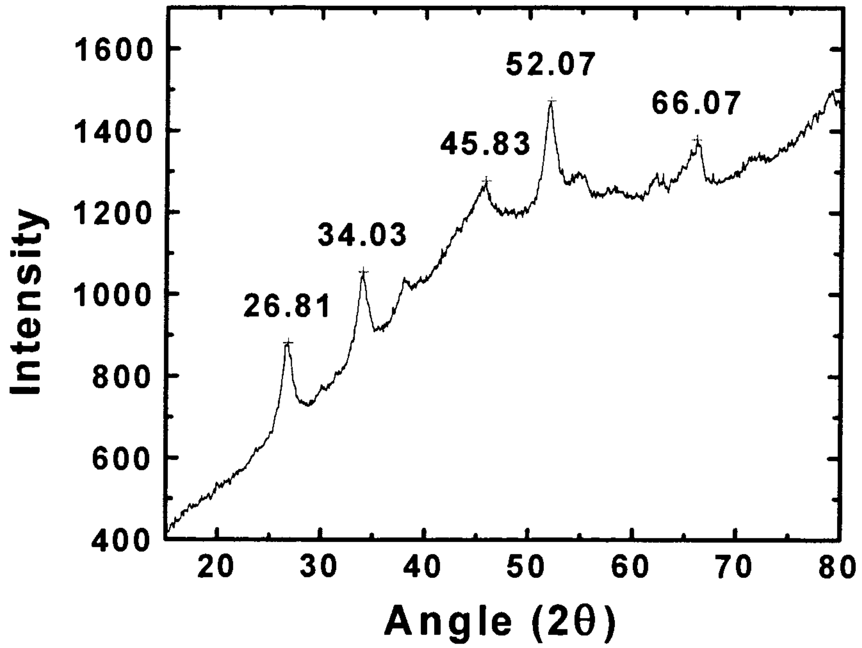

Figure 5.5 XRD pattern associated with a photoproduced tin oxide film which had been annealed at 800 °C for 1 hour.

5.3. Discussion

The precursor, tin (II) 2-ethylhexanoate, could be formed into thin films of optical quality by spin coating. The actual structure of this spin cast film cannot be determined with certainty although the FTIR spectrum indicates that the film contains primarily bridging 2-ethylhexanoate ligands. One structural model consistent with this result is shown in Figure 5.2. This structure consists of a polymer of tin (II) centers held together by bridging carboxylate ligands. The polymer is terminated by bidentate carboxylate ligands.

Not included in this model is the presence of monodentate 2-ethylhexanoic acid. This ligand is presumably located randomly within the film and gives rise to some tin (II) centers with five or six coordination.

The photolysis of a thin film of tin (II) 2-ethylhexanoate results in the formation of a tin (II) oxide thin film. The process is lithographic and can be used to define micron size patterns.

With regards to the mechanism of the photoreaction, it appears when the sample is first photolyzed, the free acid will coordinate with the metal center, forming a super saturated molecule. This phenomenon is supported by the FTIR data during photolysis. It was observed that the decrease in the intensity of the free 2-ethylhexanoic acid was accompanied by an increase in the signal of the bridging absorption at 1610 cm^{-1}.

The photoreaction involves the absorption of a photon from the precursor molecule, resulting in a charge transfer transition. This results in the transfer of an electron from the 2-ethylhexanoate ligand to a tin (II) center generating a tin (I) ion in the backbone of the polymer. This step in outlined in the scheme in Figure 5.6. The loss of the electron from the 2-ethylhexanoate leads to the fragmentation of the 2-ethylhexanoate ligand releasing carbon dioxide and a 3-heptanyl radical as shown in the subsequent step in Figure 5.6. This is consistent with the observation of carbon dioxide in the mass spectrum. The abstraction of a hydrogen atom from one 3-heptanyl radical by another leads to the formation of heptane and heptene by the reaction shown in equation 5.2.

$$2\,(C_7H_{15})\bullet \rightarrow C_7H_{16} + C_7H_{14} \qquad 5.2$$

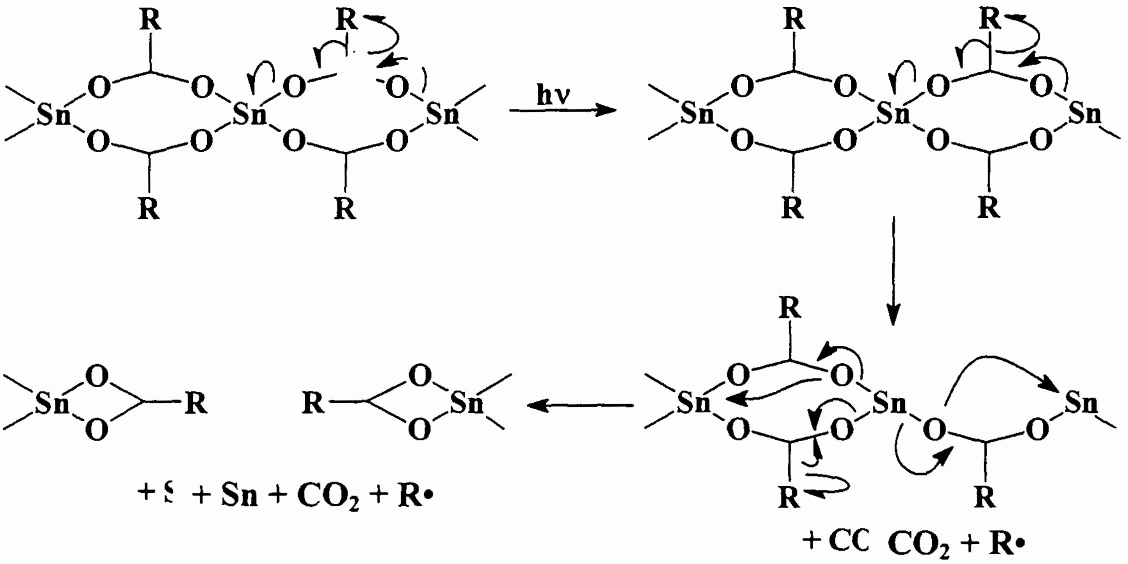

Figure 5.6 Proposed mechanism for the photoreaction of tin (II) 2-ethylhexanoate.

The loss of a single 2-ethylhexanoate ligand leaves a tin (I) within the backbone of the chain. This tin (I) atom is coordinatively unsaturated as is one of the tin (II) ions.

One of the remaining 2-ethylhexanoate ligands rearranges to provide a single coodinatively saturated tin ion, presumably this is the tin (II) ion, and further lowers the coordination of the tin (I) ion. The rearranged ligand is now bidentate and is responsible for the appearance of the 1550 cm^{-1} band in the FTIR of the film. The subsequent reactions in Scheme 1 are more speculative. One of the remaining ligands rearranges to provide a terminal bidentate ligand. This further increases the intensity of the band at 1550 cm^{-1}. The coordinatively unsaturated tin (I) then may decompose either as a result of its instability due to unsaturation or as a result of reaction with oxygen. The 2-ethylhexanoate ligand then fragments yielding carbon dioxide and a 3-heptene radical.

The appearance of FTIR band associated with the antisymmetric CO stretches at 1550 cm^{-1} is presumably a result of the continued shortening of the polymeric chain. After a short time the photoreaction of the bidentate carboxylate groups becomes significant.

The reaction of the bidentate carboxylate group is presumably the result of a charge transfer transisiton from the 2-ethylhexanoate ligand to the tin. The photoreaction and fragmentation is shown in Figure 5.7 for a single tin (II) with two bidentate 2-ethylhexanoate ligands. The ligand to metal charge transfer transition renders the ligand unstable and it fragments yielding a carbon dioxide and a 3-heptanyl radical. The tin (I) 2-ethylhexanoate, produced in this reaction, is presumably unstable and fragments as discussed above.

As illustrated in both Chapter 2 and Chapter 3, it is important to point out that the proposed mechanism was deduced from volatile fragments detected by mass spectrometry when the precursor film was photolyzed in vacuum. When the precursor film is photolyzed under ambient conditions, alternative mechanism such as oxidation of the unstable tin (I) intermediates by oxygen (in stead of thermal decomposition tin metal and ligand fragments) is also a possibility.

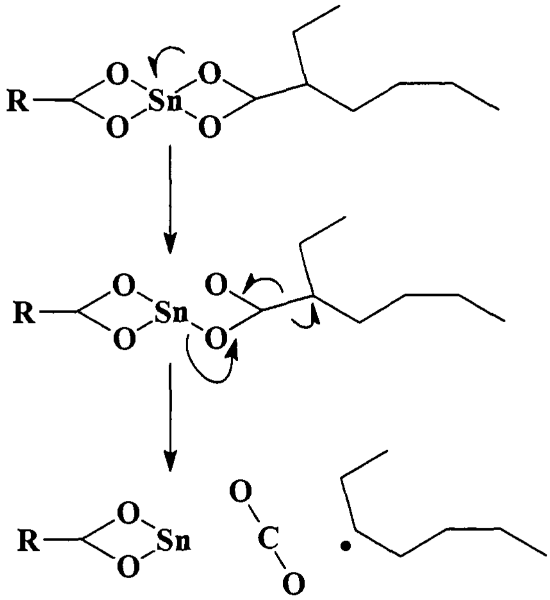

Figure 5.7 Proposed mechanism for a single tin (II) 2-ethylhexanoate bidentate molecule.

5.4. Conclusion

Tin oxide synthesis using PMOD has successfully been demonstrated using tin (II) 2-ethylhexanoate as the precursor. After photolysis there were no absorption bands associated with the vibrations of carbon oxygen bonds, an indication of the ligands being removed from the film. Carbon-free tin oxide films were obtained in the photoreaction and the photolithography of tin oxide was successfully demonstrated using the tin (II) 2-ethylhexanoate presursor.

5.5. Acknowledgements

We thank Miss Melissa Dowd for assistance with the calibration experiment of tin (II) 2-ethylhexanoate.

5.6. Experimental

5.6.1 Instrument and materials

The substrate used for the deposition of metal oxides was *p* type Si (100). The silicon wafers were cut in house to the approximate dimensions of 1 cm x 1.5 cm. The UV-Vis absorption spectra were recorded with a HP 8452A diode array spectrophotometer with a range 190-800 nm. The mass spectra were recorded using a HP 5958 GC/MS spectrometer with an electron impact ion source. The substrates used for the electronic absorption spectra measurements were CaF_2 crystals purchased from Wilmad Glass Co. Inc. The FTIR spectra were obtained with 4 cm^{-1} resolution using a Bomem Michelson 120 FTIR spectrophotometer. Auger electron spectra were obtained using a PHI double pass CMA at 0.85 eV resolution at the Surface Physics Laboratory, Department of Physics, Simon Fraser University.

X-ray analyses were done with a Rigaku diffractometer equipped with R-AXIS RAPID imaging plate area detector using a CuKα source at Department of Chemistry, Simon Fraser University.

The photolysis experiments were done using a 254 nm output low pressure Hg arc lamp in ambient conditions. The lamp intensity was measured with an International Light IL 1350 Radiometer with the sensor area of 2.835 cm^2. The power of the lamp was found to be (5 mW or 9.72×10^{-9} $Ecm^{-2}s^{-1}$).

The precursor complex, tin (II) 2-ethylhexanoate, was obtained from Aldrich Chemical. The obtained sample had some 2-ethylhexanoic acid impurity.

5.6.2 Calibrations of spectroscopic absorption

The calibration experiment was performed by Miss Melissa Dowd. A stock solution of tin (II) 2-ethylhexanoate was prepared by dissolving 0.1105 g tin (II) 2-ethylhexanoate in hexanes (1.1070 g) and diluting an aliquote of this solution (1.0 ml) to a volume of 10 ml with hexanes. A drop of this solution (0.00409 ml) was deposited on a silicon chip. After solvent evaporation, the FTIR spectrum was obtained. The same procedure was repeated for several successive drops. At the end of the experiment the area of the drop was measured to be 0.78 cm^2. Each drop of the solution corresponds to the coverage of 4.9 molecules per $Å^2$. The absorbance at 1610 cm^{-1} was plotted against the coverage (molecules/$Å^2$) and the extinction coefficients ($Å^2$/molecule) were calculated from the slope of the line. The FTIR of the deposited film was obtained as each drop was added and is presented in Figure 5.8.

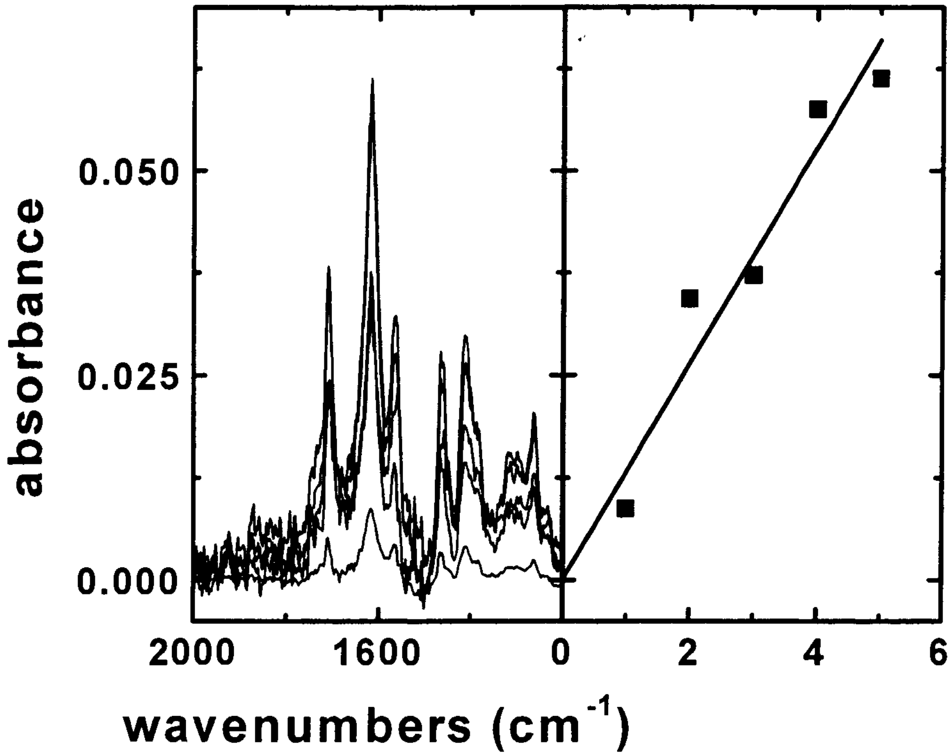

Figure 5.8 Figure showing the a) Overlaid spectra of tin (II) 2-ethylhexanoate for 1, 2, 3, 4, 5 drops molecules per Å^2 on a silicon surface and b) a plot of the absorbance versus coverage at 1610 cm^{-1}.

The extinction coefficients of absorption bands in the electronic spectrum were obtained by comparison. A film of tin (II) 2-ethylhexanoate was cast on CaF_2 and both the FTIR and UV spectra were obtained. The absorbance was measured directly for the specific wavelength whereas the extinction coefficients were obtained relative to the infrared results. For tin (II) 2-ethylhexanoate, the molar extinction coefficient at 1610 cm^{-1} was calculated as 1.22×10^5 cm^2mol^{-1}. In a similar fashion the extinction coefficient at the photolysis wavelength, 254 nm, was found to be 3.84×10^5 cm^2mol^{-1}.

5.6.3 Photolysis of the tin (II) 2-ethylhexanoate on silicon surfaces

A solution of tin (II) 2-ethylhexanoate in hexanes was prepared and used to spin coat a calcium fluoride substrate. An amorphous, smooth and continuos film was obtained. The coated silicon chip was placed in the spectrophotometer and the FTIR spectrum was recorded. The sample was then irradiated with 254 nm light for 5 seconds. The FTIR spectrum was obtained again. This procedure was repeated for the accumulated photolysis times of 5, 15, 30, 60, 120, 240, 600, 1800, 3600, 7200, 14400 and 30000 seconds.

The same solution was used to prepare another precursor film onto a silicon substrate and underwent the similar irradiation procedure as the photolysis above. The product was analyzed with Auger electron spectroscopy and powdered X-ray diffraction.

A similar experiment was conducted in which the sample was first placed in an quartz container. The container was evacuated and the sample was photolysed under a static vacuum. The gaseous contents of the container were then injected directly into the inlet of the mass spectrometer and analyzed.

Chapter 6

Photochemical Metal Organic Deposition of Indium Oxide Thin Films and Tin-doped Indium Oxide Thin Films

6.1 Introduction

In this chapter photochemical metal organic deposition (PMOD) of indium oxide thin films will be demonstrated. Indium oxide (In_2O_3) is an n-type semiconductor. Films of In_2O_3 are transparent and exhibit good electrical conductivity leading to a variety of applications in electronic devices such as gas sensors, liquid crystal displays, solar cells, solid electrolyte cells and photovoltaic devices.[98-101] Techniques used to deposit In_2O_3 films include chemical vapor deposition (CVD), spray pyrolysis, vacuum evaporation and sputtering.[102-105]

The incorporation of a dopant in In_2O_3 films changes the electrical properties significantly. Different dopants have been used in attempts to improve the electrical properties of In_2O_3. Tin is the most effective and commonly used dopant in decreasing the electrical resistivity of indium oxide films.[106] In tin doped indium oxide, Sn^{4+} substitutes for the In^{3+} cation creating a donor level between the valence and conduction bands of indium oxide.[107] A variety of processes have been used to deposit tin-doped indium oxide films. These include sputtering, spray pyrolysis, vacuum evaporation, chemical vapor deposition, RF aerosol plasma deposition and metal organic deposition.[108-113] However, none of these techniques allow direct patterning of tin-doped indium oxide, which PMOD enables.

In_2O_3 films have previously been deposited by PMOD using indium (III) 2-ethylhexanoate as the precursor.[114] It was found that the precursor films crystallized, leading to a reduction in the photoefficiency. Thicker films were found to be less inert towards crystallization. In this study an indium β-diketonate compound is used as the precursor for the PMOD of indium oxide. Metal β-diketonate compounds have been used successfully as precursors for the PMOD process in preparing metal oxide thin films.[115-117] Photolysis of metal β-diketonate films lead to ligand-to-metal charge transfer (LMCT) transitions. This transition results in the fragmentation of the precursor compound, leading to the formation of metal oxides under ambient conditions. In this chapter, a PMOD process to deposit tin-doped indium oxide from a mixture of indium and tin precursors will also be introduced.

6.2 Results

6.1.1 Characterization of amorphous indium methyl(trimethyl)acetylacetate precursor films

The molecular structure of a monomeric unit of indium methyl(trimethyl)acetylacetate is illustrated in Figure 6.1. This complex has large organic ligands which contain an unresolved chiral carbon. Since each molecule has three of these chiral centers the molecule is a mixture of enantiomers and diasteriomers.

Such a mixture of compounds has a much lower tendency to crystallize than a single compound. This results in the formation of a stable amorphous indium precursor film upon spin coating of the precursor solution onto a substrate.

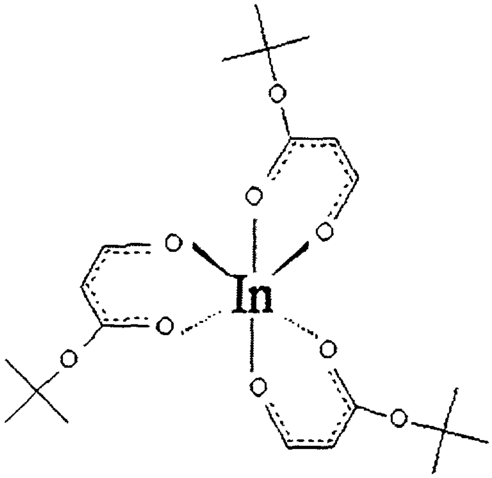

Figure 6.1 Indium methyl(trimethyl)acetylacetate.

Indium methyl(trimethyl)acetylacetate was dissolved in ethylacetate. Amorphous films were prepared by spin coating the ethylacetate solution of indium methyl(trimethyl)acetylacetate onto silicon substrates. Films were of good optical quality. A typical FTIR spectrum of indium ethyl(trimethyl)acetylacetate is shown in Figure 6.2. The assignments for the FTIR absorption peaks as well as their corresponding extinction coefficients are summarized in Table 6.1.

The FTIR absorptions were assigned by comparison with metal β-diketonate complexes.[39, 118] The absorptions between 3000 to 2800 cm^{-1} are associated with the CH stretching modes of the methyl(trimethyl)acetylacetate ligand. There are a number of intense peaks between 1700 cm^{-1} and 1000 cm^{-1}. The absorption band at 1602 cm^{-1} is assigned to ν(CC) while the peak at 1582 cm^{-1} is assigned to ν(CO). The peak at 1507 cm^{-1} is assigned to ν(CO) coupled with ν(CC). The absorption band at 1454 cm^{-1} is assigned to $\delta(CH_3)$. Peaks at 1273 cm^{-1} and 1225 cm^{-1} are assigned to ν(CC) coupled with $\nu(C\text{-}CH_3)$ and δ(CH) coupled with $\nu(C\text{-}CH_3)$ respectively. The band at 1047 cm^{-1} is assigned to $\rho(CH_3)$.

The UV-vis absorption spectrum of the indium precursor film indicates an absorption maximum at 276 nm, which is assigned to a charge transfer transition.

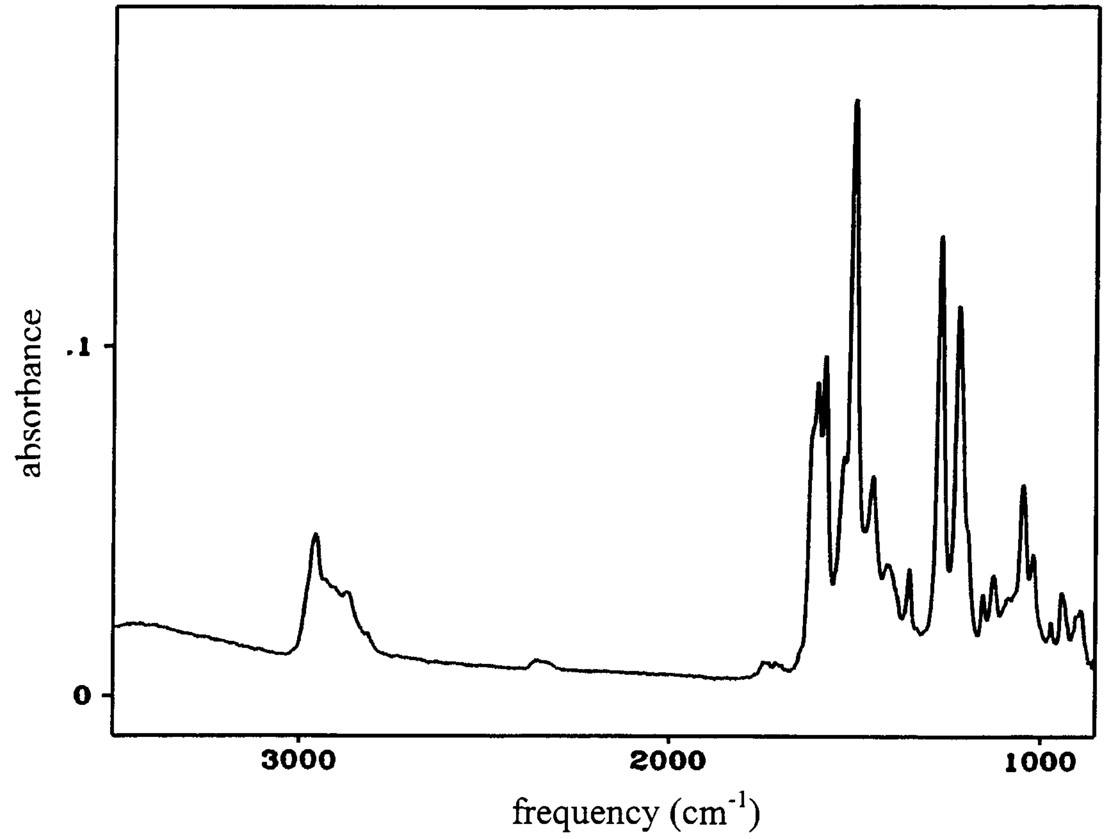

Figure 6.2 FTIR spectrum of indium ethyl(trimethyl)acetylacetate.

Table 6.1 FTIR data for indium (III) methyl(trimethyl)acetylacetate.

Band maxima	ε (10^5 cm^2/mol)	assignments
1602 cm^{-1}	3.19	ν(CC)
1582 cm^{-1}	3.45	ν(CO)
1507 cm^{-1}	6.04	ν(CO) + ν(CC)
1454 cm^{-1}	2.24	δ(CH_3)
1273 cm^{-1}	4.66	ν(CC) + ν(C-CH_3)
1225 cm^{-1}	3.95	δ(CH) + ν(C-CH_3)
1047 cm^{-1}	2.15	ρ(CH_3)
UV peak at 276 nm	77.0	Charge transfer
UV absorbance at 254 nm*	27.4	

* Absorbance at the irradiation wavelength, not a band maxima

A thin film of indium (III) methyl(trimethyl)acetyacetate was also characterized by UV-Vis spectroscopy. The electronic absorption spectrum for an amorphous film of indium (III) methyl(trimethyl)acetyacetate was characterized by an absorption band in the region of 276 nm. The molar extinction coefficient for this band was determined by comparison with the extinction coefficient measured for the IR transitions. The molar extinction coefficient of the peak together with the extinction coefficient at 254 nm is shown in Table 6.1.

6.2.2 Photochemistry of indium (III) methyl(trimethyl)acetylacetate

A thin film of indium (III) methyl(trimethyl)acetylacetate was obtained by spin coating an ethylacetate solution of the precursor onto a CaF_2 substrate. A FTIR spectrum of the precursor film was acquired. The film was then irradiated using a lamp with an output at 254 nm for 2 minutes and a second FTIR spectrum was taken. The film was irradiated further and FTIR spectra taken at various time intervals. The photolysis of the precursor film continued until no change in the FTIR spectrum was observed. An overlay of the FTIR spectra for the photolysis of the indium precursor is shown in Figure 6.3.

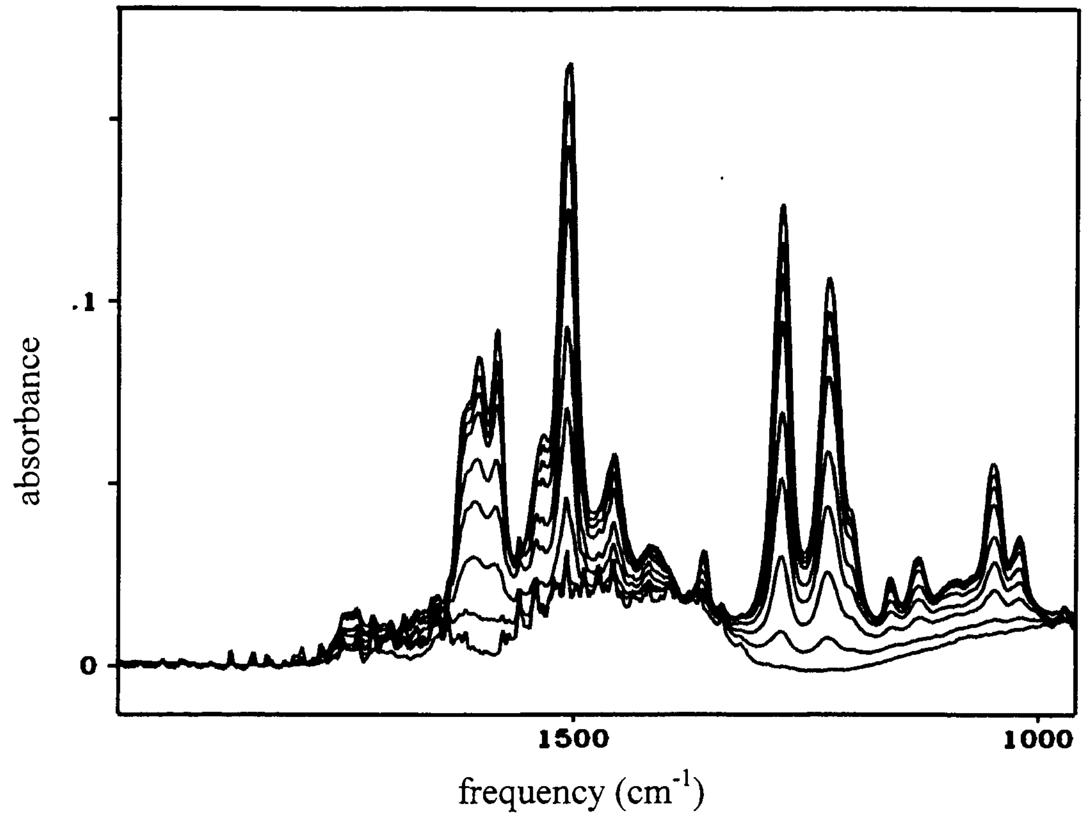

Figure 6.3 FTIR spectra associated with the photolysis of an amorphous film of indium (III) methyl(trimethyl)acetylacetate for 0, 2, 5, 10, 20, 30, 50, 80 and 140 min. The intensities of all FTIR bands decreased upon photolysis.

The absorption peaks of the precursor decrease in proportion to their initial intensity, indicating the absence of thermally stable intermediates during the photoreaction. There is no evidence for the presence of the starting material at the end of the photoreaction. The remaining absorptions observed in the FTIR spectra, shown in Figure 6.3, were attributed to artifacts during spectrum subtraction with the air background.

6.2.3 Determination of the quantum yield for the photoreaction

The efficiency of the photoreaction is interpreted by evaluating the decomposition quantum yield of the reaction. Previous studies have provided an equation, which describes the time evolution of the amount of photoreaction as a function of photolysis time, and is represented in equation 6.1.[9, 55]

$$\frac{dX}{(A^0 X/(A^0 X + A^f - A^f X))(1 - e^{-2.303(A^0 X + A^f - A^f X)})} = \frac{\Phi I^0 dt}{c^0} \tag{6.1}$$

In equation 6.1, the mole fraction, X, of the starting material is related to the photolysis time, t, incident light intensity, I^0, initial film concentration, c^0, initial and final absorbance at the irradiation wavelength, A^0 and A^f and the quantum yield, Φ. In order to solve for the quantum yield, Φ, numerical integration was used with the quantum yield as the only variable in the fitting procedure. The simulation from the integration is given in Figure 6.4. The resultant quantum yield for the photoraction was found to be 0.58 ± 0.29.

The confidence in the estimate of the quantum yield obtained by this method is guarded as the method provides no simple process to access the error. Given this limitation, the error is conservatively reported as 50 %.

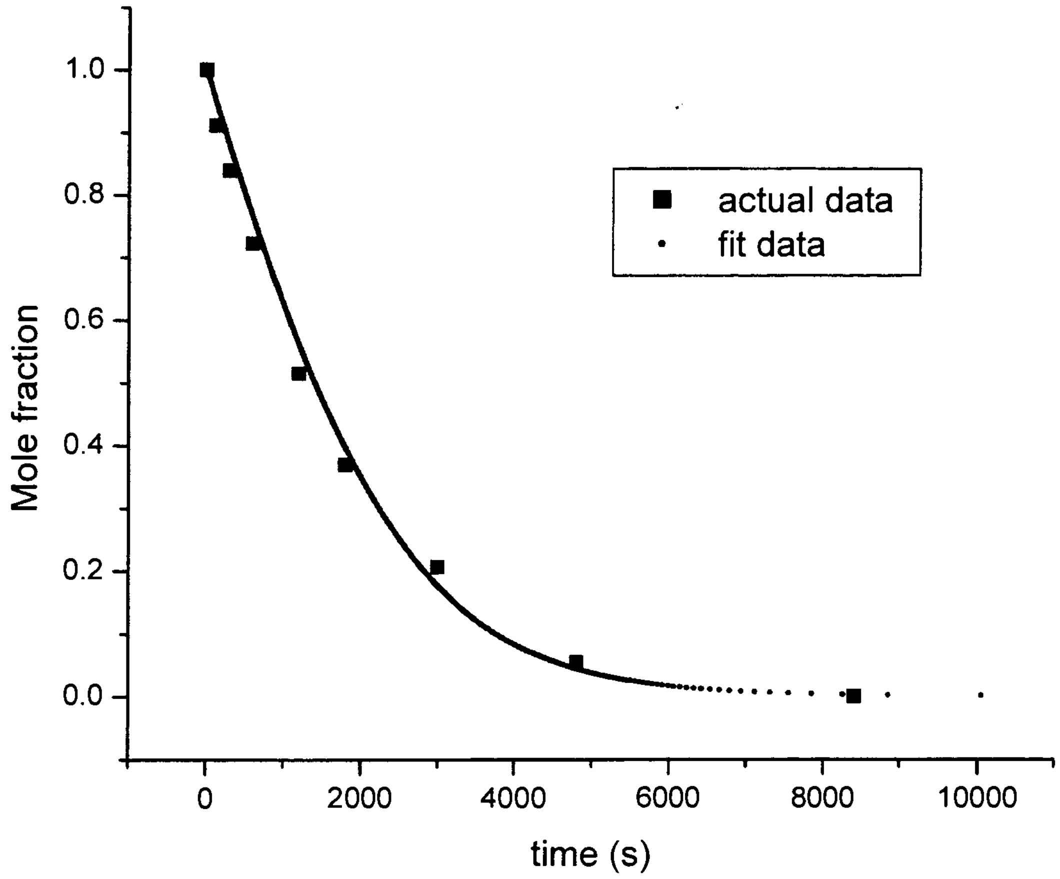

Figure 6.4 A plot of mole fraction against photolysis time for the indium precursor where squares represent experimental data and the points represent the numerical integration based on a quantum yield of 0.58 ± 0.29.

6.2.4 Characterization of the products of the photoreactions of indium (III) methyl(trimethyl)acetylacetate

6.2.4.1 Elemental composition of the film produced by photolysis of indium (III) methyl(trimethyl)acetylacetate films

The elemental composition of the photolyzed film was determined by Auger electron spectroscopy and the results are summarized in Table 6.2. Carbon impurities were detected on the surface of the film (18%). The interior of the film was carbon free as revealed by sputtering the film with an argon ion beam. A constant indium to oxygen ratio of 2 to 3 was detected with Auger electron spectroscopy, indicating the film composition as In_2O_3. The carbon contamination on the surface of the film was likely due to contamination from the environment.

Table 6.2 Auger electron spectroscopic results from a film produced by the photolysis of indium (III) methyl(trimethyl)acetylacetate.

Sputter Times	%In	%O	%C
0 sec	31 ± 2	51 ± 3	18 ± 4
12sec	41 ± 2	59 ± 4	0
24 sec	41 ± 2	59 ± 4	0

6.2.4.2 Characterization of the volatile products produced by the photoreactions of indium (III) methyl(trimethyl)acetylacetate films

Valuable information for the mechanism of the photolysis of indium (III) methyl(trimethyl)acetylacetate can be obtained by evaluating the photo-fragments produced from the photoylsis. In order to obtain such information, a thin film of indium (III) methyl(trimethyl)acetylacetate on silicon substrate was photolyzed under a static vacuum. The volatile products of the photoreaction were analyzed by mass spectrometry. Mass peaks at M/e of 99, 82, 67, 57, 44, 43 and 27 were assigned to the parent ligand, 3-oxo-1, 1-dimethylethyl butanoic acid ester by comparison with a reference database for the ligand.[58] The strong MS peak at M/e 44 was assigned to CO_2. The mass spectrum also contains peaks that were believed to result from the fragmentation of the photolyzed precursor at m/z of 100, 75 and 70. We were unable to assign those peaks to particular fragmentation products.

6.2.4.3 X-ray diffraction from the films produced by the photoreactions

X-ray diffraction from the film produced from the photolysis of indium (III) methyl(trimethyl)acetylacetate was obtained. The featureless nature of the X-ray spectrum revealed that the resultant film was amorphous in nature. The resultant film was then heated in a furnace at 500°C for 1 hour and X-ray diffraction was used to investigate the heated film. The X-ray data is shown in Figure 6.5. The data revealed reflections at 2θ positions of 21.6°, 30.7°, 35.5°, 51.2° and 56.3°. The peaks match the (211), (222), (400), (440) and (622) reflections of In_2O_3 respectively, indicating crystallization of the resultant films during the heat treatment. The peak with 2θ at 33.0 was a reflection from the substrate.

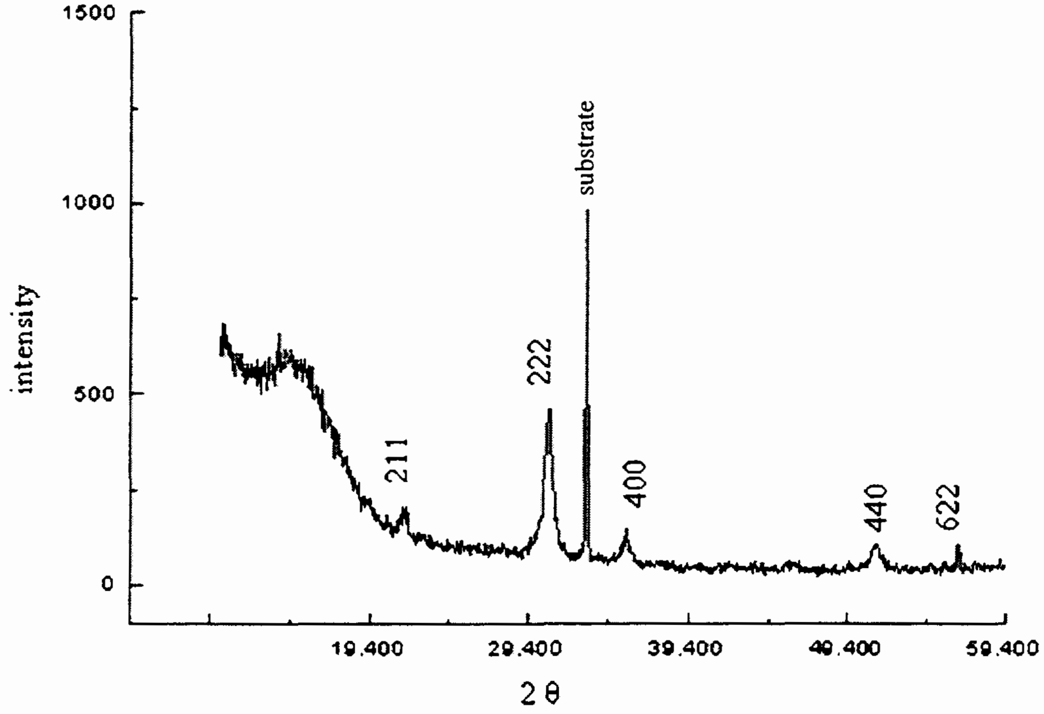

Figure 6.5 Powder x-ray diffraction of a film produced by photolysis of indium methyl(trimethyl)acetylacetate upon a heat treatment at 500 °C for one hour (the reflection at 33.0° is due to the silicon substrate).

6.2.5 Dose to print measurement for the indium (III) methyl(trimethyl) acetylacetate film

An amorphous film of indium (III) methyl(trimethyl)acetylacetate on silicon substrate was prepared and irradiated through a neutral density mask in contact mode for 2 hours. After the irradiation, a latent image was formed and the film was developed by rinsing with ethylacetate to reveal the image. The intensity of the irradiation was measured with a power meter and this data, together with the printed image on the film was used to determine the dose to print for the indium (III) methyl(trimethyl)acetylacetate. The dose to print indium oxide from indium (III) methyl(trimethyl)acetylacetate was found to be 5.1 J/cm^2.

6.2.6 Preparation of tin-doped indium oxide thin films by PMOD

6.2.6.1 Photochemistry of mixed tin (II) 2-ethylhexanoate and indium (III) ethyl(trimethyl)acetylacetate

PMOD of a mixture of tin and indium precursors was used to prepare tin doped indium oxide thin films. The tin precursor being used was tin (II) 2-ethylhexanoate while the indium precursor was indium (III) ethyl(trimethyl)acetylacetate. In chapter 5 and earlier sections in this chapter the photochemistry of tin (II) 2-ethylhexanoate and indium (III) ethyl(trimethyl)acetylacetate was presented. In this section the photochemistry of the combined tin and indium precursors will be presented.

A 10 % tin (atomic ratio of tin vs indium) solution of indium (III) ethyl(trimethyl)acetylacetate was prepared by mixing a measured amount of tin (II) 2-

ethylhexanoate and indium (III) ethyl(trimethyl)acetylacetate in ethylacetate. A thin film from the mixed precursor solution was prepared by spin coating the solution onto a glass substrate. The photolysis of the film under an irradiation wavelength of 254 nm was monitored by FTIR. The FTIR spectra obtained during the photoreaction are shown in Figure 6.6.

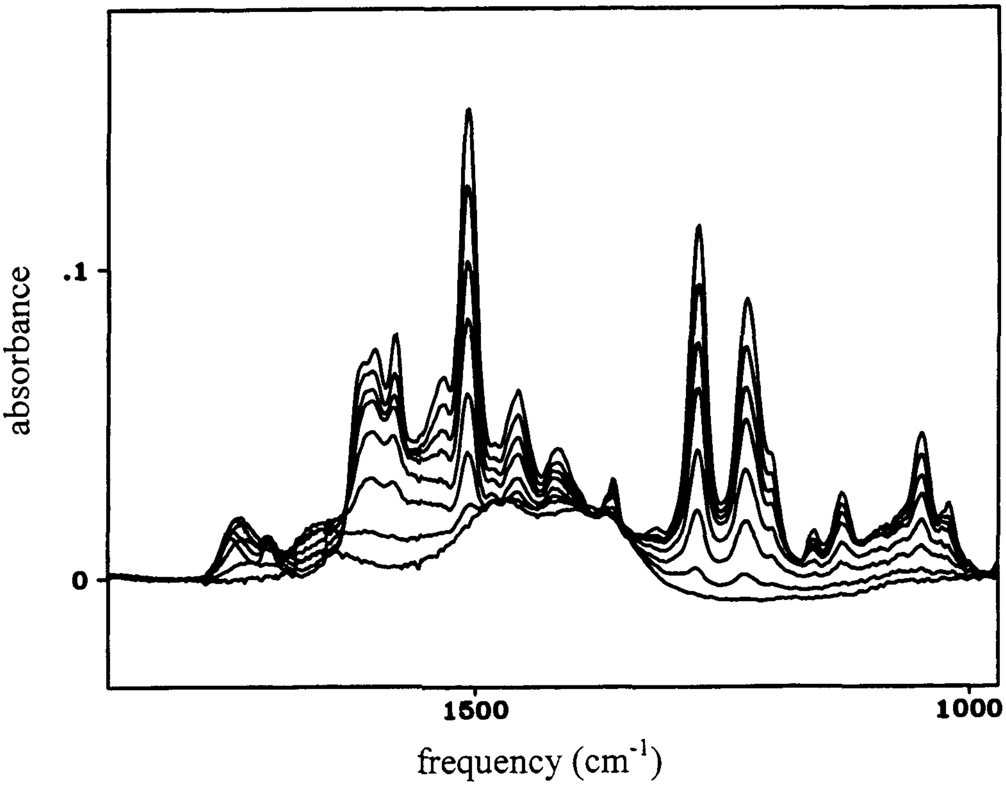

Figure 6.6 FTIR spectra of mixed tin and indium precursor upon 254 nm irradiation for 0, 2, 5, 10, 20, 35, 60, 105 minutes. The intensities of all FTIR absorptions decreased upon photolysis.

The FTIR spectrum of the mixed precursor system can be interpreted as due to the addition of the spectra of tin (II) 2-ethylhexanoate and indium (III) ethyl(trimethyl)acetylacetate. The absorption peaks decayed upon irradiation, indicating the conversion of the precursors to their corresponding oxides. No intermediates were observed during the photoreaction and irradiation continued until no further changes in the FTIR spectrum were observed. The remaining absorption bands observed in the FTIR spectum were attributed to the artifacts associated with spectral subtraction with the air background. X-ray diffraction of the as-deposited film indicated the film was amorphous in nature.

6.2.6.2 Elemental ratio of tin and indium from the as-deposited film

The elemental composition of the as-deposited film was determined by Auger electron spectroscopy. Indium, tin, carbon and oxygen were found to be present on the surface of the resultant film from the photoreaction by Auger electron spectroscopy. Upon sputtering with argon ions, a carbon-free film consisting of indium, tin and oxygen was obtained. This is consistent with the removal of surface contamination from the resultant film. Auger electron spectroscopy was used to determine the atomic ratio of Sn : In and the results are summarized in Table 6.3. The data obtained from Auger electron spectroscopy on the tin-doped indium film is within error of the original tin to indium ratio in the precursor mixture.

Table 6.3 Auger Electron Spectroscopy data for the atomic ratio of Sn : In in the deposited film.

Sputter Times (seconds)	Sn : In (%)
0	15 ± 4
120	10 ± 3
240	12 ± 4

6.2.6.3 Effect of heating on the as-deposited tin-doped indium oxide

A precursor film was prepared by spin coating the same precursor mixture onto a pyrex substrate. The film was photolyzed under 254 nm irradiation until completion. The film was then heated in a furnace in air at 500 ^{0}C for one hour. The x-ray diffractogram was obtained on the resultant film. The result is shown in Figure 6.7. The broad background signal in the x-ray spectrum was attributed to the pyrex substrate. X-ray peaks with 2θ at 30.7°, 35.5° and 51.2° corresponding to the (222), (400) and (440) reflections of In_2O_3 were observed. This indicated crystallization of the films occurred during the heat treatment. We are unable to identify the peak with 2θ at 60.7°. The result is consistent with crystallization of tin-doped indium oxide thin film.[119]

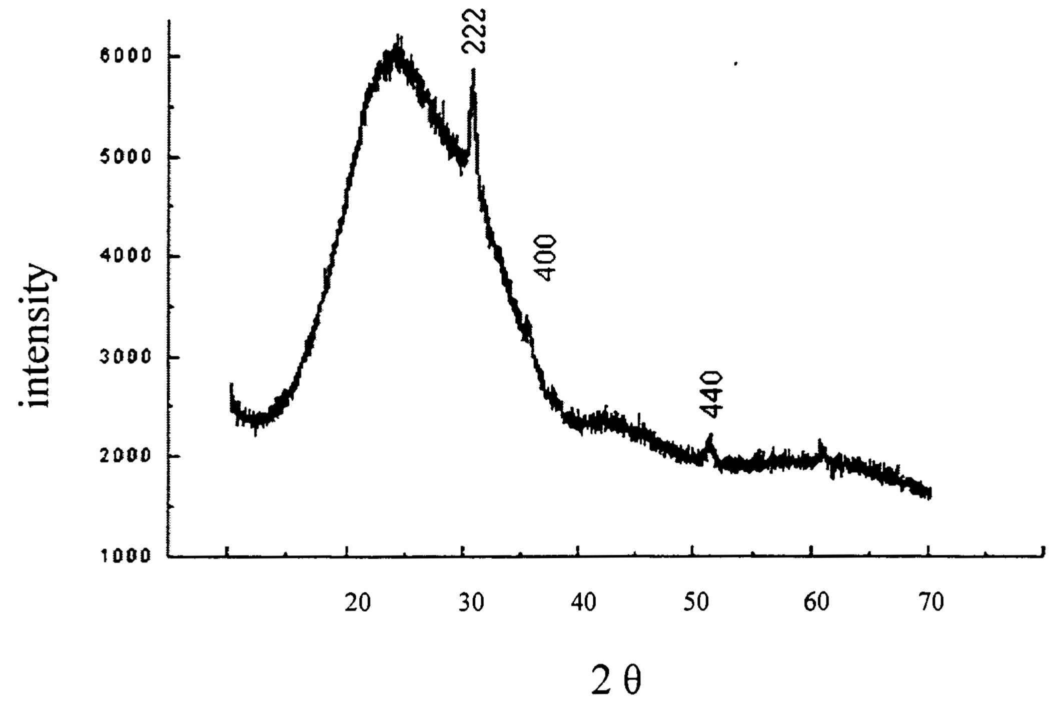

Figure 6.7 X-ray diffraction spectrum of the tin-doped indium oxide film deposited on Pyrex substrate heat treated at 500 ^{0}C in air for one hour.

6.2.7 Resistivity measurements for indium oxide and tin-doped indium oxide deposited by PMOD

In order to measure the resistivity of the indium oxide and tin-doped indium oxide prepared by PMOD, four-point probe measurements were performed on the films. The sheet resistance of the as-deposited indium oxide and tin-doped indium oxide were measured and the result is summarized in Table 6.4. Neither film conducted sufficiently well that the resistance could be measured. The films were then heated in a furnace at

500 °C in air for one hour and four-point probe measurements were again performed on the films. The resultant sheet resistance data is presented in Table 6.4. In each case a measurable resistance was obtained. The doped film had a lower resistance than the undoped film. The thicknesses of both annealed films were measured with a profilometer and were on the order of 60 nm.

Table 6.4 Sheet resistance measurements for indium oxide and tin-doped indium oxide prepared by PMOD.

	Indium oxide (Ω / □)	Tin-doped indium oxide (Ω / □)
As-deposited	Not observed	Not observed
500 °C 1 hour	120	84
Commercial sample	N/A	11

The sheet resistance of a tin-doped indium oxide coated glass substrate was also evaluated with the same technique. The resistance was found to be 84 **Ω/□**. For comparison the sheet resistance of the commercial sample of ITO was found to be 11 **Ω/□**. The result indicates indium oxide or tin-doped indium oxide film prepared by the PMOD process will increase in conductivity upon annealing.

6.3 Discussions

In this chapter the solid state photochemistry of indium (III) methyl(trimethyl)acetylacetate thin film was presented. It was shown that carbon-free amorphous indium oxide thin film resulted from the photoreaction of indium (III) methyl(trimethyl)acetylacetate. The proposed mechanism for the photoreaction is presented in Figure 6.8.

When the precursor film is photolyzed, the indium precursor (1) absorbs a photon, leading to a ligand-to-metal charge transfer (LMCT) transition in the precursor. This results in the cleavage of one indium-oxygen bond, forming a diradical species (2). The complex (2) undergoes fragmentation due to the presence of an unstable indium (II) center. The fragmentation leads to the formation of an intermediate (3) as well as the β-diketonate radical (4). Species (3) is unstable and undergoes further fragmentation leading to the formation of an indium atom and two more β-diketonate radicals (4). In the presence of oxygen under ambient conditions during the photolysis, indium oxide (5) is formed. This mechanism was supported by the IR data as well as the quantum yield calculation. The Auger evidence for indium oxide as final product of the photoreaction supported the mechanism. It is believed the β-diketonate radicals undergo disproportionation, leading to the formation of the parent ligand (6), 3-oxo-1, 1-dimethylethyl butanoic acid ester, as well as other fragmentation products. Results from mass spectrometry of the volatile products from the photoreaction indicated the presence of 3-oxo-1, 1-dimethylethyl butanoic acid ester and it is believed the unidentified MS peaks were due to other fragmentation products from the radical.

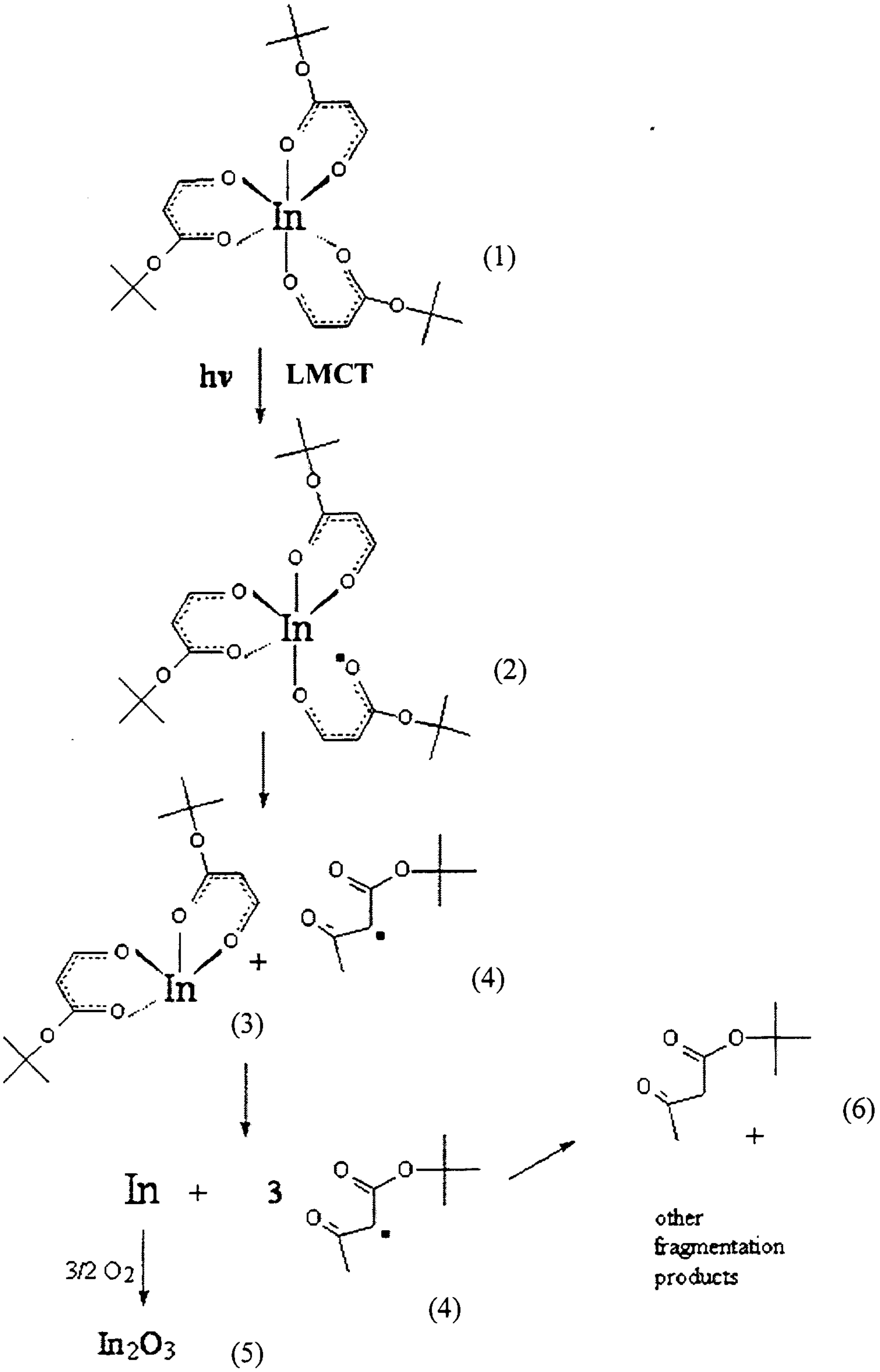

Figure 6.8 Proposed mechanism for the photoreaction of indium (III) methyl(trimethyl)acetylacetate.

Upon annealing the PMOD deposited indium oxide to 500 °C crystallization occurred as indicated by the powder x-ray diffraction.

One main application of indium oxide and tin-doped indium oxide is as transparent electrodes for display fabrication due to its low resistivity and transparent nature. The conductivity of tin-doped indium oxide is highest when the dopant ratio (Sn : In) is at about 10%. Higher dopant level will alter the crystal structure of indium oxide, leading to a decrease in its conductivity. The resistivities of the as-deposited indium oxide and tin-doped indium oxide thin films were so high that they are essentially non-conductive. However when the films were heated to 500 °C in air, their respective resistivities decreased significantly. The phenomenon can be explained due to the crystallization of the indium oxide and tin-doped indium oxide thin films upon annealing.

The electrical conduction of indium oxide is explained through its band structure. Crystalline indium oxide has a direct band-gap of 3.75 eV.[120, 121] The conduction band is mainly from In:5s electrons and the valence band is from O^{2-}:2p electrons. Indium oxide is generally oxygen deficient and a large number of native donors are produced because of oxygen vacancies. The low conductivities from the PMOD deposited amorphous films can be explained by the increase in electron scattering in the amorphous films during electrical conduction. The sheet resistance of the tin-doped indium oxide film is higher than that of the commercial sample. This phenomenon is probably due to the fact that the film deposited by PMOD is quite thin compared to the commercial sample (60 nm for PMOD as compared to 0.5-1 μm). Any impurities and defects in the film will also lead to a higher sheet resistance.

6.4 Conclusion

In this study, carbon free indium oxide was prepared by the photolysis of indium methyl(trimethyl)acetylacetate films. Irradiation triggers a ligand-to-metal charge transfer transition in the precursor, leading to the fragmentation of the precursor molecule. This leads to the formation of indium oxide when the reaction is carried out in air. Tin-doped indium oxide thin films were also prepared and it was also found that the amorphous indium oxide and tin-doped indium oxide have significantly lower electrical conductivity than their crystalline counterparts.

6.5 Experimental

6.5.1 Instrument and materials

All silicon wafers were obtained from Wafernet and were n-type Si(100). The wafers were cut to the approximate dimensions of 1 cm x 1.5 cm in house. The NaCl crystals were obtained from Spectra-Tech Inc. Microscope slides were used as the glass substrates. The FTIR spectra were obtained with a Bomem MB-120 with 4 cm^{-1} resolution. Electronic absorption spectra were obtained with a HP 8452A diode array spectrometer. The irradiation source for photolysis was conducted with the 254nm output of a low pressure mercury lamp. The intensity of the light source was measured by Gentec detector head PS-310 with a TPM-300 monitor. The mass spectra were obtained from a HP 5958 gas chromatography-MS spectrometer. An electron-impact ion source was used and the ion source temperature was 200 °C. The resolution was 1000 amu^{-1} with electron energy for ionization at 70 eV. Auger spectra were obtained using a PHI double pass CMA at 0.85eV resolution at the Surface Physics Laboratory, Department of Physics, Simon Fraser University. The complex indium (III) methyl(trimethyl)acetylacetate was purchased from Gelest.

6.5.2 Calibration of the Fourier transform IR and UV-visible absorption on silicon surfaces

Indium (III) methyl(trimethyl)acetylacetate solution (conc. 1.80 x 10^{-5} mol/ml) was prepared by dissolving the precursor (0.1584g) into ethyl acetate (15ml). A drop of the solution (0.0032ml) was placed on the silicon surface and allowed to dry. FTIR spectrum of the drop was obtained. The process was repeated 4 more times and a total of seven spectra were overlay as in Figure 6.9. The absorbance at 1508 cm^{-1} against the concentration was plotted as shown in Figure 6.10. The extinction coefficient for the IR absorption of the precursor at 1508 cm^{-1} was found to be 6.040x10^5 cm^2/mol from the slope of the plot.

The extinction coefficient for the UV-visible absorption of the precursor was derived from the extinction coefficient for the IR absorption. A precursor film was prepared by spin coating the precursor solution onto CaF substrate. Both FTIR as well as UV-visible spectra were obtained for the film. The extinction coefficient for the absorption peak (276nm) and wavelength of irradiation (254nm) was obtained relative to the predetermined FTIR bands. The extinction coefficients UV absorption at 276 nm (absorption peak) and at 254 nm are 7.70 x 10^6 and 2.74 x 10^6 cm^2/mol respectively.

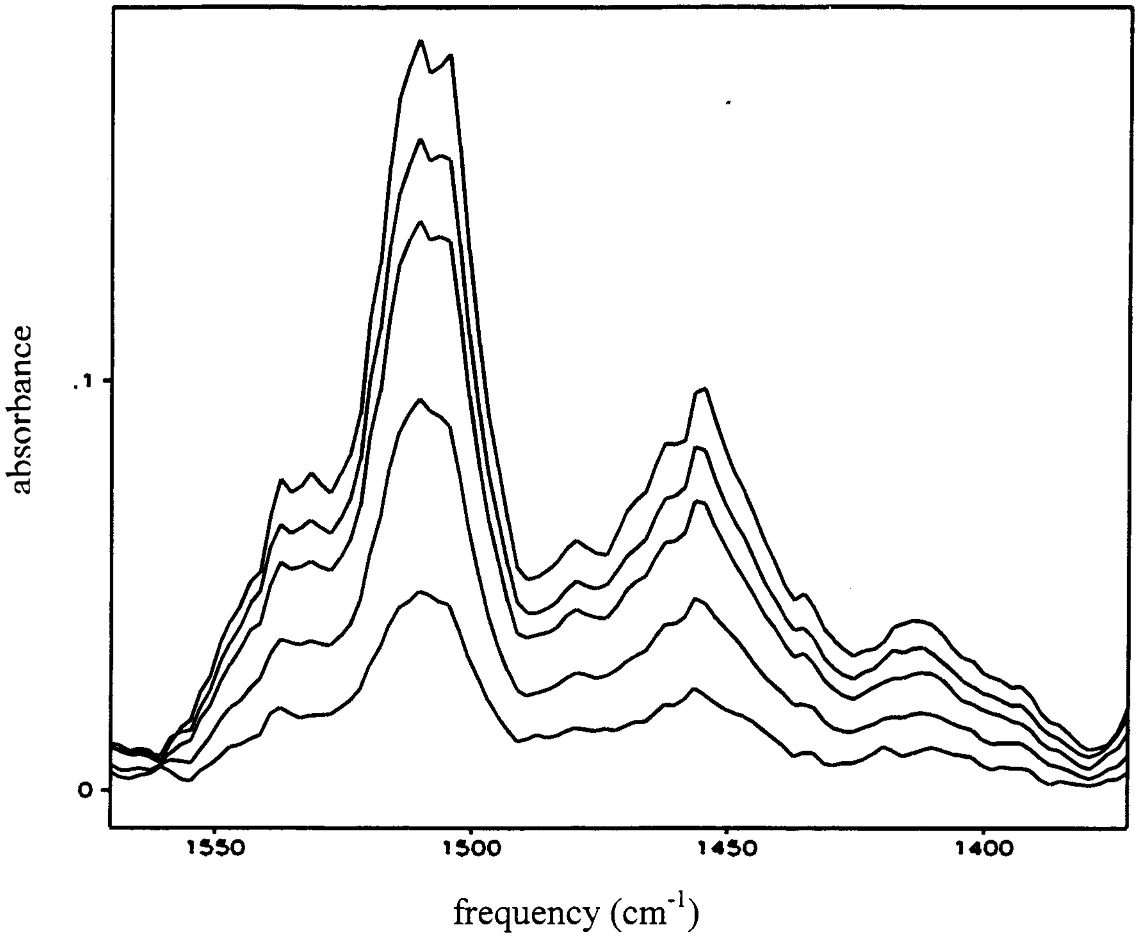

Figure 6.9 Calibration plot indium (III) methyl(trimethyl)acetylacetate.

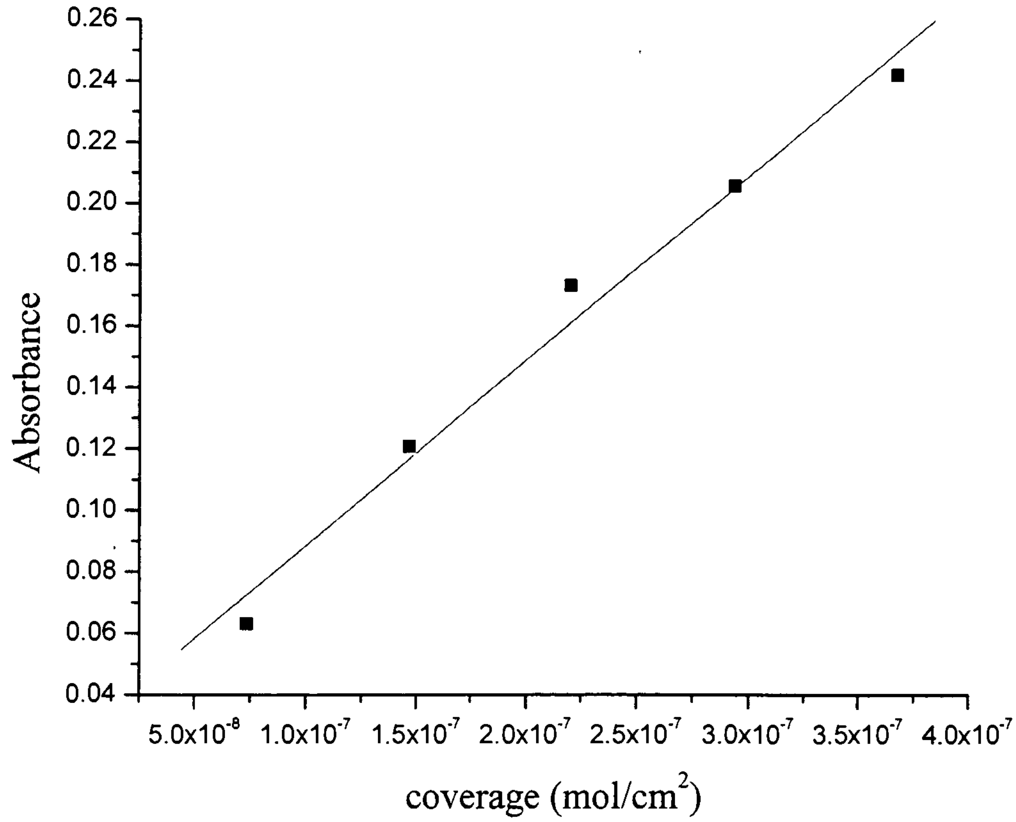

Figure 6.10 Plot of absorbance vs coverage of indium (III) methyl(trimethyl)acetylacetate at 1508 cm^{-1}.

6.5.3 Photolysis of film of indium (III) methyl(trimethyl)acetylacetate

A precursor film of indium (III) methyl(trimethyl)acetylacetate was spin coated onto silicon chips (1x1.5 cm^2) from solutions of ethyl acetate. The FTIR of the samples were obtained and the samples then photolyzed. The FTIR spectra were again obtained and the process repeated until no absorbance associated with the precursors was evident from the FTIR. By monitoring both the light intensity and the extent of reaction the apparent quantum yields for the photoreactions were determined. The composition of the photolyzed products were evaluated by Auger electron spectroscopy. Powder X-ray diffraction was also performed on the photolyzed films.

6.5.4 Mass Spectrometric analyses of volatile products from the photoreactions

A film of the indium precursor was prepared onto silicon chips in the same fashion as the photolysis reaction. The sample was then photolyzed in a sealed, evacuated quartz vessel. Following each photolysis the contents of the head space of the vessel were analyzed. The analysis was conducted by injecting the gaseous contents directly in the chamber of the mass spectrometer. MS data for the photolysis of indium (III) methyl(trimethyl)acetylacetate was obtained.

6.5.5 Four-point probe resistivity measurement

A four-point head with a linear configuration, and with each electrode spaced 1mm apart, was mounted onto a Wentworth probe stand. Current was injected at the two outside probes and voltage was measured across the two inner probes. The measurement was done by connecting the four-point probe to a HP 3478A multimeter in 4 wire resistance mode. The measurement resistance value was then converted to sheet resistance from the formula $R_s = 4.53(R)$ where R_s is the sheet resistance and R is the measured resistance.

Chapter 7

Summary

7.1. Overall Summary

The main focus of my research was to extend Photochemical Metal Organic Deposition (PMOD) beyond transition metal systems. It was also a goal of my research to develop chemistry to deposit potentially important mixed metal oxide thin films using the PMOD process.

From my research, PMOD processes in the deposition of main group metal oxides of aluminum oxide, indium oxide and tin oxide were developed. The PMOD process was also extended to lanthanide metal oxides of cerium oxide and europium oxide. Results indicated that PMOD deposited metal oxide thin films are porous in nature. It was also found that the precursor film for PMOD may contain associated molecules.

I have also successfully demonstrated photoresist-free lithographic deposition of metal oxide thin films using the PMOD process. The PMOD process requires less image transformation steps compared to conventional lithographic methods using photoresists. Fewer steps are required to deposit a metal oxide pattern when compared to the conventional process. This provides an attractive alternative for the deposition of metal oxides.

Modifying the precursor molecule by the introduction of asymmetry in the ligand proved to be a useful strategy in the formation of amorphous precursor films as well as increasing the purity of the final products.

The preparations of mixed metal oxide thin films were also demonstrated. Europium doped aluminum oxide and tin-doped indium oxide thin films were successfully deposited using the PMOD process. Important thin film properties such as photoluminescence (europium doped aluminum oxide) and transparent electrical conductivity (tin-doped indium oxide) were obtained from thin films developed by the process.

All in all, I believe I have achieved the research goals that I set out before I started my research project and in the process made additional unexpected advances in the science of lithography.

List of References

1. A.R. Chowdhuri and C.G. Takoudis, *Thin Solid Films*, **446**, 155 (2004).
2. S. Iakovlev, C.H. Solterbeck, M. Es-Souni and V. Zaporojtchenko, *Thin Solid Films,* **446**, 50 (2004).
3. Y.S. Jung, J.Y. Seo, D.W. Lee and D.Y. Jeon, *Thin Solid Films,* **445**, 63 (2003).
4. R. Nayak, V. Gupta, A. L. Dawar and K. Sreenivas, *Thin Solid Films,* **445**, 118 (2003).
5. O. Nilsen, H. Fjellvåg and A. Kjekshus, *Thin Solid Films,* **444**, 45 (2003).
6. M.M. Bagheri-Mohagheghi and M. Shokooh-Saremi, *Thin Solid Films,* **441**, 238 (2003).
7. A.A. Avey and R.H. Hill, *J. Am. Chem. Soc.,* **118**, 237 (1996).
8. M. Gao and R.H. Hill, *Journal of Materials Research*, **13**, 1397 (1998).
9. M. Gao and R.H. Hill, *J. PhotoChem. Photobiol. A: Chemistry*, **97**, 73 (1996).
10. S.L. Blair and R.H. Hill, *J. Organometallic Chemistry*, **554**, 63 (1998).
11. S. L. Blair, Simon Fraser University Ph.D. thesis (1996).
12. R.C. Mehrotra, *Metal carboxylates*, Academic Press (1983).
13. M. Bronislaw and E.B.C. Gonzalo, *Journal of Photochemistry and Photobiology, A: Chemistry,* **52**, 1 (1990).
14. J.R.V. Garcia and T. Goto, *Science and Technology of Advanced Materials,* **4**, 397 (2003).
15. P.Sandstrom, E.B. Svedberg, M.P. Johansson, J. Birch and J.E. Sungren, *Thin Solid Films*, **353**, 166 (1999).
16. I.K. Schuller, *Physical Review Letters*, **24**, 1597 (1980).

17. D. Chattarji, *The theory of Auger transitions,* Academic Press (1976).

18. V. Emeline, G.N. Kuzmin, D. Purevdorj, V.K. Ryabchuk and N.Serpone, *J. Phys. Chem. B*, **104**, 2989 (2000).

19. E. Wayne and R.P. Wayne, *Photochemistry*, Oxford University Press, (1996).

20. A.R. West, *Solid state chemistry and its applications*, John Wiley & Sons (1996).

21. H.L. Hartnagel, A.L. Dawar, A.K. Jain and C. Jagadish, *Semiconducting Transparent Thin Films*, Institute of Physics Publishing (1995).

22. P. Meena, C. Balsubramaniam, S.K. Narayandas and D. Mangalraj, *Commun. Instrum.,* **2,** 88 (1988).

23. T. Inoue, Y. Yamamoto, S. Koyama, S. Suzuki and Y. Ueda, *Appl. Phys. Lett.,* **56**, 1332 (1990).

24. L. Tye, N.A. El-Mastry, T. Chikyow, P. McLarty and S.M. Bedair, *Appl. Phys. Lett.,* **65**, 3081 (1994).

25. D. Huang, F. Qin, Z. Yao, Z. Ren, L. Lin, W. Gao and Q, Ren, *Appl. Phys. Lett.,* **67,** 3724 (1995).

26. X.D. Wu, R.C. Dye, R.E. Maenchausen, S.R. Foltyn, M. Maley, A.D. Rollett, A.R. Garcia and N.S. Nogar, *Appl. Phys. Lett.,* **58,** 2165 (1991).

27. H. Sato, R. Miyakawa, N. Nakamura, S.R. Gjoen, H. Akoh and S. Takada, *Jpn. J. Appl. Phys.,* **35,** L311 (1996).

28. F. Wang and R. Wordenweber, *Thin Solid Films,* **227,** 200 (1993).

29. G. Atanassov, R. Thielsch and B. Popov, *Thin Solid Films,* **223,** 288 (1993).

30. K.B. Sundaram, P.F. Wahid and P.J. Sisk, *Thin Solid Films,* **221,**13 (1992).

31. A.A. Dakhel, *Materials Chemistry and Physics,* **80,** 186 (2003)

32. M.P. Mulloy, W.S. Blau and J.G. Lunney, *J. Appl. Phys.,* **73**, 4104 (1993).

33. H. Nagata, M. Yoshimoto and H. Koinuma, *J. Cryst. Growth,* **118,** 299 (1992).

34. F. Sanchez, M. Varela, C. Ferrater, M.V. Garcia-Cuenca, R. Aguiar and J.L. Morenza, *Appl. Surf. Sci.,* **171** 94 (1993).

35. S. Yaegashi, T. Kurihara, H. Hoshi and H. Segawa, *Jpn. J. Appl. Phys.,* **33**, 270 (1994).

36. N.S. Gaikwad and C.H. Bhosale, *Materials Chemistry and Physics,* **71**, 242 (2001).

37. D.G. Karraker, *J. Inorg. Nucl. Chem.,* **31**, 2815 (1969)

38. A.L. Grigor'ev and V.N. Maksimov, *Russ. J. Inorg. Chem.,* **9,** 580 (1964).

39. K. Nakamoto, *"Infraed and Raman Spectra of Inorganic and Organometallic Compounds"*, 4th ed., John Wiley & Sons, New York (1986)

40. B.J. Palmer, *Photochemistry of inorganic and organometallic complexes in various media*, Ph.D. Thesis Simon Fraser University (1992)

41. A.W. Adamson and P.D. Fleischaner, *Concepts in Inorganic Photochemistry, R.E. Krieger Publishing, Malabar, FL* (1984).

42. R.A. Sheldon and J.K. Kochi, *J. Am. Chem. Soc.,* **90,** 6688 (1968).

43. P. Starynowicz, *Polyhedron,* **22,** 2761 (2003).

44. J.S. Kim, H.A. Marzouk, P.J. Reucroft, J.D. Robertson and C.E. Hamrin, *Appl. Phys. Lett.,* **62**, 681 (1993).

45. C.E. Chryssou and C.W. Pitt, *Appl. Phys. A.,* **65**, 469 (1997).

46. M. Tiitta, E. Nykanen, P. Soininen, L. Niinisto, M. Leskela and R. Lappalainen, *Mat. Res. Bull.*, **33,** 1315 (1998).

47. A. Serquis and R. Zimmerman, *J. Phys.: Condens. Matter,* **5,** A321 (1993).

48. R.H. Hill, A.A. Avey, S.L. Blair, M.Gao and B.J. Palmer, *Mater. Chem. Phys.*, **43,** 233 (1996).

49. J.P. Bravo-Vasquez, L.W.C. Ching, W.L. Law and R.H. Hill, *J. Photopolymer Sci. Technol.,* **11,** 589 (1998).

50. L.W.C. Ching and R.H. Hill, *J. Vac. Sci. Technol. A,* **16,** 897 (1998).

51. W.L. Law and R.H. Hill, *Mat. Res. Bull.,* **33,** 69 (1998).

52. C.W. Chu and R.H. Hill, *Mater. Chem. Phys.,* **43,** 135 (1996).

53. C.W. Chu, M.J. Deen and R.H. Hill, *J. Electrochem. Soc.,* **145,** 4219 (1998).

54. B. Marciniak and G.E. Buono-Core, *J. Photochem. Photobio. A: Chem.,* **52,** 1 (1990).

55. A. Becalska, R.J. Batchelor, F.W.B. Einstein, R.H. Hill and B.J. Palmer, *Inorg. Chem.*, **31,** 3118 (1992).

56. L.S. Andronic and R.H. Hill, *J. Photochem. Photobiol. A: Chemistry,* **15,** 259 (2002).

57. F. W. Mclafferty, *Interpretation of Mass Spectra*, fourth edition, Mill Valley, California; University Science Books (1993)

58. Mass Spectrometry Database of Chemicals, Wiley (1989)

59. R.C. Mehrotra and A.K. Rai, *Polyhedron,* **10,** 1967 (1991).

60. G. T. Morgan and H. D. K. Drew, *J. Chem. Soc.,* **119,** 1058 (1921).

61. A. Esparza, M. Garcia and C. Falcony, *Thin Solid Films,* **325,** 14 (1998).

62. T.H. Maiman, *Nature*, **187**, 493 (1960)

63. C.E. Chrysson and C.W. Pitt, *Applied Physics A*, **65**, 469 (1997).

64. V. Surganov and A. Mozalev, *Microelect. Eng:*, **37-38**, 329 (1997).

65. V. Surganov, A. Mozalev and V. Boksha, *Microelect. Eng.*, **37-38**, 335 (1997).

66. L.L. Young, *Anodic Oxide Films,* Academic Press, New York, (1971)

67. Y. Kurokawa, T. Ishizaka, T. Ikoma and S. Tero-Kubota, *Chemical Physics Letters*, **287**, 737 (1998).

68. J.A. Thornton and J. Chin, *Ceram. Bull.,* **56**, 504 (1977).

69. C. Taschner, B. Ljungberg, I. Endler and A. Leonhardt, *Surf. Coat. Technol.,* **116,** 891, (1999).

70. I. Shimizu, Y. Setsuhara, S. Miyake, M. Kumagai, K. Ogata, M. Kohata and K. Yamaguchi, *Surface and Coatings Technology,* **131**, 187 (2000).

71. Q.Y. Zhang, W.J. Zhao, P.S. Wang, L. Wang, J.J. Xu and P.K. Chu, *Nuclear Instruments and Methods in Physics Research B*, **206**, 357 (2003).

72. S. Lazarouk, S. Katsouba, A. Leshok, A. Demianovich, V. Stanovski, S. Voitech, V. Vysotski and V. Ponomar, *Microelect. Eng.,* **50**, 321 (2000).

73. *CRC Handbook of Chemistry and Physics,* CRC Press, (1989).

74. N.V. Gaponenko, *Journal of Applied Spectroscopy*, **69**, 1 (2002).

75. D.S. Wu and N.L. Wu, *J. Materials Research,* **15**, 1445 (2000).

76. Y. Idota, A. Matsufuji, Y. Maekawa, and T. Miyasaka, *Science*, **276,** 1395 (1977).

77. I.A. Courtney and J.R. Dahn, *J. Electrochem. Soc.*, **144**, 2045 (1977).

78. S. Semancik and T.B. Fryberger, *Sens. Actuators, B*, **1**, 97 (1990).

79. A.K. Gosh, C. Fishman and T. Feng, *J. Appl. Phys.*, **49**, 3490 (1978).

80. J.L. Vossen, *Phys. Thin Films,* **9,** 1 (1977)

81. S.K. Song, D. Kim, S. Kim, S.K. Koh, H.J. Jung, J.Y. Lee and H.K. Baik, *J. Materials Research*, **15**, 1911 (2000).

82. J.S. Marifacier, L. Szepessy, J.F. Bresse, M. Perotin and R. Stuck, *Mater. Res. Bull.*, **14,** 109 (1979).

83. E. Giani and R. Kelly, *J. Electrochem. Soc.,* **121,** 394 (1974).

84. J. R. Bosnell and R. Waghtone, *Thin Solid Films*, **15**, 141 (1973).

85. T. Susuki, T. Yamazaki, H. Yoshioka and K. Hikichi, *J. Mater. Sci.*, **23**, 145 (1988).

86. R.N. Ghostagore, *J. Electrochem. Soc.*, **125,** 110 (1978).

87. J. C. Manifacier, M. de Murcia and J. P. Fillard, *Thin Solid Films,* **41**, 127 (1977).

88. S.S. Park and J.D. Mackenzie, *Thin Solid Films*, **258**, 268 (1995).

89. R. H. Hill, A. A. Avey, S. L. Blair, M. Gao and B. J. Palmer, *IUMRS-ICEM 1994*, **1**, 435, Materials Research Society-Taiwan.

90. Y. Shi, G. Li and R. H. Hill, *Mat. Sci. in Semiconductor Processing*, **2**, 297 (1999).

91. H. J. Emeleus and A. G. Sharpe, *Advances in inorganic chemistry and radiochemistry*, New York San Francisco London (1977).

92. J.E. Tackett, *Applied spectroscopy,* **43**, 483 (1989).

93. S.L. Blair, C.W. Chu and R. Dammel, R. H. Hill, *SPIE,* **3049**, 829 (1997).

94. G.B. Deacon and R.J. Phillips, *Coordination Chemistry Reviews,* **33**, 227 (1980).

95. J.D. Donaldson and A. Jelen, *J. Chem. Soc. (A)*, 1448 (1968).

96. T.A. Lee, *A beginner's guide to mass spectral interpretation*, Chichester, New York, Wiley, (1998).

97. Joint Committee on Powder Diffraction Standards-ICDD database.

98. A. Gurlo, M. Ivanovskaya, A. Pfau, U. Weimar and W. Gopel, *Thin Solid Films* **307,** 288 (1997).

99. L.A. Perez-Maquela , L. Wang and E. Matijevic, *Langmuir,* **14,** 4397 (1998).

100. A. Gurlo, N. Barsan, M. Ivanovskaya, U. Weimar and W. Gopel, *Sens. Actuators B,* **47,** 327 (1998).

101. A. Wang, J.R. Babcock, N.L. Edleman, A.W. Metz, M.A. Lane, R. Asahi,V.P. Dravid, C.R. Kannewurf, A.J. Freeman and T.J. Marks, *PNAS,* **98,** 7113 (2001).

102. F.J. Gutierrez, L.ares, J.I. Robla, M.C. Horrillo, I. Sayago and J.J. Agapito, *Sens. Actuators B,* **8,** 231 (1992).

103. T. Suzuki, T. Yamazaki, K. Hayashi and T. Noma, *J. Mater. Sci.,* **26**, 6419 (1991).

104. H. Pink, L. Treitinger and L. Vite, *Japan. J. Appl. Phys.,* **19**, 513 (1980).

105. H. Nanto, H. Sokooshi, T. Kawai and T. Usuda, *J. Mater. Sci. Lett.,* **11**, 235 (1992).

106. H.L. Hartnagel, A.L. Dawar, A.K.Jain and C. Jagadish, *Semiconducting Transparent Thin Films*, Institute of Physics Publishing, Bristol and Philadelphia, (1995).

107. A.P. Genis, P.A. Smith, K. Emery, R. Singh and J.B. Dubow, *Appl. Phys. Lett.*, **37**, 77 (1980).

108. Y. Shigesato, S. Takaka, and T. Haranoh, *J. Appl. Phys.*, **71**, 3356 (1992).

109. C. Agashe, M. Takwale, V. Bhide, S. Mahamuni, and S. Kulkarni, *J. Appl. Phys.*, **70**, 7382 (1991).

110. S. Chen, K. Yang, and J. Wang, *Thin Solid Films*, **162**, 305 (1988).

111. C. Wan, R. McGrath, W. Keenan, and S. Frank, *J. Electrochem. Soc.*, **136**, 1459 (1989).

112. D.H. Lee, K.D. Vuong, J. A.A. Williams, J.Fagan, R.A. Condrate, Sr., and X.W. Wang, *J. Mater. Res.*, **11**, 895 (1996).

113. D. Gallagher, F. Scanlan, R. Houriet, H.J. Mathieu, and T.A. Ring, *J. Mater. Res.*, **11**, 3135 (1996).

114. C.L.W. Ching and R.H. Hill, *J.* Vac. Sci.& Tech. A., **16**, 897 (1998).

115. W. L. Law and R.H. Hill, *Thin Solid Films*, **375**, 42, (2000).

116. H.J. Zhu and R.H. Hill, *J. PhotoChem. Photobiol. A: Chemistry*, **147**, 127 (2002).

117. G.E. Buono-Core, M. Tejos, G. Alveal and R.H. Hill, *Journal of Materials Science*, **35**, 4873, (2000).

118. D.C. Bradley and R.C. Mehrotra, *Metal Alkoxides*, Academic Press Inc. (1978).

119. K. Utsumi, H. Iigusa, R. Tokumaru, P.K. Song and Y. Shigesato, *Thin Solid Films,* **445**, 229 (2003).

120. I. Hamberg and C.G. Granqvist, *J. Appl. Phys.,* **60**, 123 (1986).

121. J.C.C. Fan and J.B. Goodenough, *J. Appl. Phys.,* **48**, 3524 (1977).